Doctoral Thesis

博士論文

First-principles study of magnetic properties in transition-metal alloys

第一原理計算を用いた遷移金属合金における磁気的性質の研究

Naohiro Ito

伊東 直洋

Department of Physics,
Graduate School of Science,
Tohoku University

東北大学大学院 理学研究科物理学専攻

2021

令和３年

Contents

1 Introduction **5**

1.1 Background 5

1.2 Purpose of the Thesis 8

1.3 Outline 9

I Background of the Theoretical Method **11**

2 Density Functional Theory **13**

2.1 Born-Oppenheimer Approximation 14

2.2 Hohenberg-Kohn Theorem 15

2.3 Kohn-Sham Equation 16

2.4 Kohn-Sham-Dirac Equation 17

3 KKR Green's Function Method **19**

3.1 Non-relativistic Free Particle Green's Function 19

3.2 Dirac Equation 21

3.2.1 Central Field 21

3.2.2 Spin-angular Part of the Dirac Equation 22

3.2.3 Properties of Spin-angular Function 23

3.2.4 Quantum Numbers in spin 1/2 Dirac Equations 24

3.3 Solution of the Free Particle Dirac Equation 24

3.3.1 Right-hand Side Solution 24

3.3.2 Left-hand Side Solution 26

3.4 Relativistic Free Particle Green's Function 27

3.5 Fourier Transform . . . 27
3.6 Structure Constants . . . 28
3.7 Multiple Scattering . . . 29
3.7.1 Dyson Equation . . . 30
3.7.2 Scattering Path Operator . . . 30
3.7.3 Multiple Scattering in the KKR Methods . . . 32
3.8 Green's Function for a Particle in a Potential . . . 33
3.9 Radial Equations . . . 34

4 Calculation of the Disordered System 37
4.1 Virtual Crystal Approximation (VCA) . . . 37
4.2 Average t-matrix Approximation (ATA) . . . 38
4.3 Coherent Potential Approximation (CPA) . . . 39
4.3.1 Derivation of the CPA Condition . . . 40
4.4 KKR-CPA Method . . . 42
4.4.1 Representation by the Scattering Path Operator . . . 42
4.4.2 Representation by the Projection Matrix . . . 44
4.4.3 Representation by the Excess Scattering Matrix . . . 45
4.4.4 Mills' Method . . . 45

II Application of the CPA on the Basis of Wannier Representation 47

5 Wannier-based Implementation of the CPA Method 49
5.1 Wannier Functions . . . 49
5.2 Wannier TB Hamiltonian . . . 50
5.3 Green's Function . . . 51
5.4 CPA in Wannier Formalism . . . 52

6 Application of the Wannier-CPA Method to Fe-based Transition-metal Alloys 55
6.1 Computational Steps of a Wannier-CPA Calculation . . . 56
6.2 Reference of the On-site Potential . . . 56

6.3 Bloch Spectral Function 58
6.4 Density of States 68
6.5 Magnetic Moment 75
6.6 Conclusion 79

7 Magnetic Properties of Fe-Cr Alloys 81
7.1 Computational Steps 81
7.2 Magnetic Structure 82
7.3 Magnetic Moment 84
7.4 Anomalous Hall Conductivity 85
7.5 Conclusion 87

8 Summary 89

Appendix 90

A Determination of the Fermi Energy 91

B Anomalous Hall Conductivity Calculation in Wannier Representation 93
B.1 Formulation 93
B.2 Gauge Transformation 94
B.3 Symmetry Operation 95
B.4 Symmetry of Berry Curvature 97

References 99

Acknowledgements 107

List of Publication 111

Chapter 1

Introduction

1.1 Background

The DFT is a powerful tool to calculate the electronic structures of molecules and solids. Originally, it was formulated to predict the energy of the systems. However, it is now recognized that the band structures and wavefunctions contain a lot of information to predict the physical properties such as transport, optical and magnetic properties. Accompanied by the development of computers, a lot of predictive studies based on the DFT including the high-throughput calculations have been performed. For example, there are several databases of DFT calculated band structures and physical properties such as Materials Project [1], Automatic Flow (AFLOW) [2], and the Open Quantum Materials Database (OQMD) [3, 4]. Some high throughput calculations lead to the experimental findings of functional materials such as discoveries of new nitride semiconductors [5] and iron-based transverse thermoelectric materials [6].

On the other hand, for the application point of view, substitutional alloys are important candidates for materials design. In fact, many substitutional alloys show a fascinating richness in their physical properties depending on their composition. For example, in spintronics, the spin Hall angle can be tuned by alloying [7]. Another example is the possibility to induce magnetism in semiconductors by the addition of impurities [8]. Thus, the development of methods to calculate the alloys is an important problem.

The methods to calculate the electronic structure of substitutional alloy systems

have been developed since the 1930s [9, 10, 11]. The simplest approach implemented first for calculations on alloys is the virtual crystal approximation, in which the concentration average of the potential is placed on each site of the lattice [12, 13]. Although the VCA seems to be a good approximation for metals having a simple free-electron-like electronic structure such as Na, K, and Al, it completely fails for the transition-metal alloys. This shortcoming of the VCA has been removed by Korringa [14] and Beeby [15] by introducing the so-called average t-matrix approximation (ATA). Within this approach, the concentration average of the single-site scattering matrix, the t-matrix, is used instead of the potential to consider component-projected properties. However, the ATA still has formal problems sometimes leading to unphysical results [9]. For homogeneous random alloys, the most sophisticated single-site method solving these problems is provided by the coherent potential approximation (CPA). The CPA is a mean-filed theory treating alloys by introducing an effective medium defined by its average scattering properties first proposed by Soven [16] and Taylor [17]. Formulating the CPA within the framework of multiple scattering or KKR formalism implies that embedding one of the alloy components into the CPA should lead to no additional scattering on average. Accordingly, unlike for the VCA and ATA methods, one has to determine the effective medium self-consistently for the CPA calculations.

As the CPA can be easily applied on the basis of electronic structure methods working with the Green's function for each atomic site, it is usually formulated by a combination with the tight-binding (TB) method or the KKR Green's function method [18, 19], which is a well-established first-principles electronic structure calculation method. Especially using the KKR-CPA method [20, 21], quite a number of physical properties of alloy systems have been studied, such as their magnetic structure properties of dilute magnetic semiconductors [22], exchange coupling, and the corresponding magnetic transition temperature [23, 24], as well as transport properties. In Ref. [25], Lowitzer et al. performed the calculation of both intrinsic and extrinsic anomalous Hall conductivity in fcc Fe-Pd and Ni-Pd alloys. Their results of the conductivity are in good agreement with the experimental data for these alloys. Lowitzer et al. also performed the extrinsic and intrinsic contributions of the spin Hall conductivity calculations in Au-Pt and Ag-Pt alloys using the KKR-CPA methods [26]. They exploited Kubo-Středa equation which is the Kubo formula with independent electron approximation

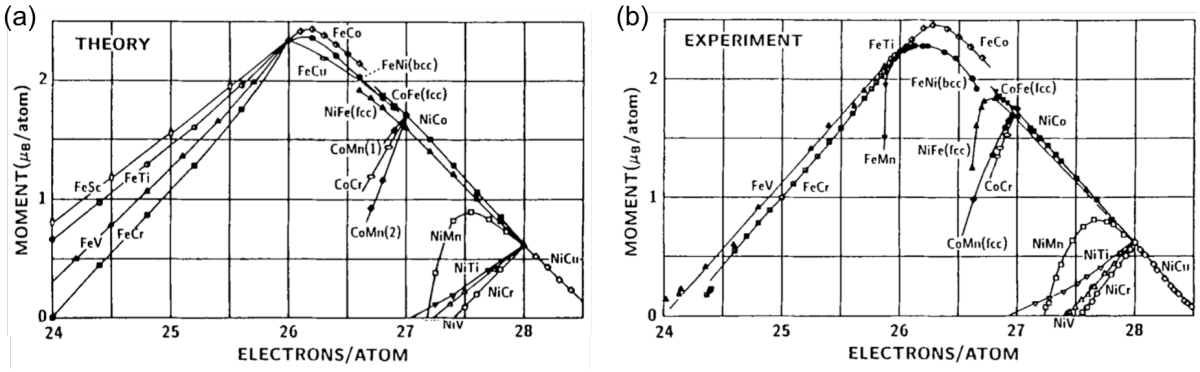

Figure 1.1: (a) Calculated and (b) experimental saturation magnetization of Fe-, Ni- and Co-based alloys vs. average electron number. Adapted from Ref. [39].

and the assumption of $T = 0$ for the calculation of these conductivities. There are several other studies on transport properties using KKR-CPA methods [27, 28, 29]. For example, Ref. [30] compare skew scattering terms of the anomalous Hall conductivity calculated by three different implementations using Kubo-Středa or Boltzmann equation, and atomic sphere approximation or full-potential implementation. The calculated results of the skew scattering agreed well even though the calculation methods are different. Another successful example of the KKR-CPA method is the calculation of the magnetic moment in 3d transition-metal alloys. Figure 1.1(a) shows KKR-CPA results of the magnetic moment calculated by Akai [39]. The magnetic moments obtained by the KKR-CPA method reproduce the saturation magnetization given by experiments [Fig. 1.1(b)] forming the well-known Slater-Pauling curve.

This situation is due to a characteristic feature of the KKR method. Unlike other general first-principles calculation methods, such as the standard pseudopotential-based methods or the linearized augmented plane wave (LAPW) method, the Green's function of the system is used already within the self-consistent field (SCF) calculation step when performing KKR calculations. Furthermore, the KKR Green's function is described using the single-site t-matrix and scattering path operator as explained in Chapter 3. Thus, it is easy to combine the KKR method with the CPA formalism, where the effect of substitutional atoms should be treated as local potentials. So-called local force method, which can calculate the exchange interactions in magnets by using the local

spin rotations, also employ this advantage [31, 32, 33, 34, 35, 36, 37, 38].

The problem of the KKR calculations is that the physical quantities have been studied only in a limited systems with particularly simple structures in the KKR-CPA method. This is because the KKR calculations are computationally intensive and require some experience and knowledge to apply the method to complex crystal systems. For example, atomic sphere approximation is a useful approximation in simple systems while it sometimes fails for systems with low crystal symmetry, while full-potential calculations require more computational costs and complicated implementations to obtain physical quantities. To use the CPA calculations as a material design method for alloy systems, there is a strong need for a simpler and easier way to calculate alloy systems.

In the field of first-principles calculations, the CPA is alternatively formulated on the basis of the tight-binding linear muffin-tin orbital (TB-LMTO) method [40] as well as the linear combination of atomic orbitals (LCAO) methods [41, 42]. The TB-LMTO-CPA method is also applied for the calculation of the anomalous Hall [43, 44] and spin Hall conductivities [45] using Kubo formula. In Ref. [45] the results they obtained reproduce the calculations of the KKR-CPA methods quite well for Au-Pt alloys. However, these are quite special calculation examples and there is no code that can be used in general. A more versatile calculation method for applying CPA is desired.

1.2 Purpose of the Thesis

In this thesis, we present an implementation of the CPA in Wannier representation to develop an efficient and widely applicable calculation method for alloy systems while keeping the accuracy for the prediction of physical properties that the KKR-CPA method possesses. The reason for exploiting the Wannier representation is that we can construct Wannier functions from any kind of first-principles calculation method if the wave function is available, and set up a corresponding TB model from the obtained Wannier functions. This means that we present a computational method for the electronic structure of random alloys that can be combined with any kind of first-principles computational method. Moreover, we can substantially reduce the computational time when using the Wannier formalism if it is successfully combined with the CPA as it

can be performed independently from the SCF calculations done by first-principles calculations. The Wannier functions are widely used to investigate physical properties [46] such as the anomalous Hall effect [47], exchange coupling [48], transport properties using the Boltzmann transport equation [49], electron-phonon couplings [50], and orbital magnetism [51]. Several open source codes have been developed to calculate the topological properties of materials [52, 53].

However, only very few studies were done for alloy systems [54, 55]. One of the reasons for this is that there is an ambiguity in the determination of the relative reference values of the on-site potentials for the elements that form an alloy. Concerning this problem, we propose a very simple method to set the reference values from the results of some few supercell calculations. Despite the simplicity of this method, we show that it works quite well for the construction of the CPA Green's function within the Wannier formalism.

In the following, we first describe the theoretical background of the calculation methods such as the density functional theory and the methodology of the KKR Green's function methods. We also formulate the CPA in terms of the KKR method as well as the Wannier representation. As examples for its application, we will show results for the Bloch spectral function, the density of states (DOS), and the magnetic moment in the Fe-based 3d transition-metal alloys, Fe-V, Fe-Co, Fe-Ni, and Fe-Cu in both the Wannier-CPA and the KKR-CPA methods. Despite the rather simple formulation for the Wannier-CPA method, these quantities obtained by this way reproduce quite well the results obtained by the more demanding KKR-CPA method. For the Fe-Cr alloys which have antiferromagnetism in Cr-rich region, we exploit the diatomic supercell and discuss the magnetic transition using the KKR-CPA method.

1.3 Outline

This thesis consists of eight chapters. In Chapter 2 we present a brief summary of the theoretical framework of the density functional theory (DFT), which provides the *ab-initio* computational method for the electronic structure calculations of real materials. This theory approximates the quantum many-body effects to the independent-particle equations called the Kohn-Sham equations. We also describe the Kohn-Sham-Dirac

equations, which are the relativistic extension of the Kohn-Sham equations. Chapter 3 is devoted to the KKR Green's function method as one of the computational methods to numerically solve the Kohn-Sham or Kohn-Sham-Dirac equations. As the name implies, we exploit the Green's function to treat the multiple scattering in a crystal. We overview this calculation methods without deriving individual formulas. The scattering path operator and the structure constants we define in this chapter is used for the discussion of the calculation of alloys. Chapter 4 presents the calculation methods of the homogeneous random alloys. The only practical method for the calculation of alloy systems is the coherent potential approximation (CPA), which is discussed later in this chapter. However, we also mention other tools, virtual crystal approximation and average t-matrix approximation, to describe the historical development of the methods to treat alloys. At the end of this chapter, we focus on the application of the CPA methods to the KKR Green's function method and its numerical calculation methods given by Mills. In Chapter 5, we describe how to implement the CPA in the Wannier formalism. We present the definition of the Green's function in the Wannier representation as well as the algorithm for the CPA calculations. Chapter 6 provides the application of the Wannier-CPA methods developed in the previous chapter to Fe-based transition-metal alloys. To verify the performance of the CPA methods implemented within the Wannier-CPA methods, we compared the Bloch spectral function, the density of states, and the magnetic moments calculated by the Wannier-CPA methods with those of calculated by the KKR-CPA methods. In Chapter 7, we focus on the Fe-Cr alloys to discuss the CPA calculations for antiferromagnets. Chapter 8 is the summary of this thesis.

Part I

Background of the Theoretical Method

Chapter 2

Density Functional Theory

In this chapter, we focus on the density functional theory (DFT). DFT is the *ab-initio* or first-principles methods for the calculation of electronic structure. This means that we would like to find a method to predict physical quantities for real materials without experiments. When it is difficult to comprehensively verify the chemical and physical properties by experiments, theoretical interpretation based on computational science becomes an important issue. According to quantum mechanics, material properties can be obtained by solving the quantum many-body Hamiltonian for the system of electrons and nuclei

$$\begin{aligned}\hat{H} = &-\frac{\hbar^2}{2m}\sum_i \nabla^2_{\boldsymbol{r}_i} + \frac{1}{2}\sum_{i\neq j}\frac{e^2}{|\boldsymbol{r}_i - \boldsymbol{r}_j|} - \sum_{i,n}\frac{Z_n e^2}{|\boldsymbol{r}_i - \boldsymbol{R}_n|} \\ &- \sum_n \frac{\hbar^2}{2M_n}\nabla^2_{\boldsymbol{R}_n} + \frac{1}{2}\sum_{n\neq m}\frac{Z_n Z_m e^2}{|\boldsymbol{R}_n - \boldsymbol{R}_m|}\,, \end{aligned} \tag{2.1}$$

where $\boldsymbol{r}_i$ is the position of the i-th electron, $\boldsymbol{R}_n$ is the position of n-th nuclei, m is the electron mass, e is the elementary charge, and Z_n and M_n are charge and mass, respectively, for n-th nuclei. To obtain the ground state properties of the real materials, we have to solve the corresponding stationary Schrödinger equations

$$\hat{H}\Psi_p(\{\boldsymbol{r}\},\{\boldsymbol{R}\}) = E_p\Psi_p(\{\boldsymbol{r}\},\{\boldsymbol{R}\})\,, \tag{2.2}$$

where p is one of the quantum states having an energy eigenvalue E_p. However, it is usually quite difficult to numerically solve this equation directly. Several computation methods have been devised as an approach to this equation such as the configuration

interaction (CI) method and the quantum Monte Carlo method. Here, as one of these calculation methods, we describe the DFT, which requires relatively low computational time. In this theory, the original many-body problem described by the Schrödinger equation in Eq. (2.1) is replaced by an auxiliary independent-particle equation called the Kohn-Sham equation. A number of methods are developed for numerically solving the Kohn-Sham equation. As one of these calculation methods, we will focus on the KKR Green's function methods in next chapter.

2.1 Born-Oppenheimer Approximation

The first approximation to the Hamiltonian given by Eq. (2.1) was proposed in 1927 by Born and Oppenheimer [56] which is known as the Born-Oppenheimer or adiabatic approximation. In the approximation the inverse of the nuclei mass $1/M_n$ is considered small enough compared to the inverse of the electron mass $1/m$. In other wards, electrons are assumed to move much faster than nuclei. Therefore, we can treat nuclei as stationary within the framework of the electron system. To confirm what is suggested by the Born-Oppenheimer approximation we separate the contribution of nuclei from the wavefunction

$$\Psi_p(\{\boldsymbol{r}\},\{\boldsymbol{R}\}) = \sum_q \chi_{pq}(\{\boldsymbol{R}\})\Psi_q^{\mathrm{el}}(\{\boldsymbol{r}\},\{\boldsymbol{R}\}) \tag{2.3}$$

and substitute it into the the Schrödinger equation given by Eq. (2.2). According to the Born-Oppenheimer approximation we can obtained the following two equations:

$$\left[-\frac{\hbar^2}{2m}\sum_i \nabla^2_{\boldsymbol{r}_i} - \frac{1}{2}\sum_{i\neq j}\frac{e^2}{|\boldsymbol{r}_i-\boldsymbol{r}_j|} + \sum_{i,n}\frac{Z_n e^2}{|\boldsymbol{r}_i-\boldsymbol{R}_n|}\right]\Psi_q^{\mathrm{el}}(\{\boldsymbol{r}\},\{\boldsymbol{R}\}) = E_q^{\mathrm{el}}\Psi_q^{\mathrm{el}}(\{\boldsymbol{r}\},\{\boldsymbol{R}\}) \tag{2.4}$$

$$\left[-\sum_n \frac{\hbar^2}{2M_n}\nabla^2_{\boldsymbol{R}_n} + E_q^{\mathrm{el}} + \frac{1}{2}\sum_{n\neq m}\frac{Z_n Z_m e^2}{|\boldsymbol{R}_n-\boldsymbol{R}_m|}\right]\chi_{pq}(\{\boldsymbol{R}\}) = E_p\chi_{pq}(\{\boldsymbol{R}\}) \tag{2.5}$$

Here, the first equation describes the Schrödinger equation only for the electron system. In other wards, the Born-Oppenheimer approximation allows to handle the electrons and nuclei motion separately. The Born-Oppenheimer approximation is applicable unless we deal with specific physical quantities such as the dispersion relation of phonons with broken symmetry.

2.2 Hohenberg-Kohn Theorem

According to the Born-Oppenheimer approximation, we can treat the electron system separately as given in Eq. (2.4). The first attempt to solve the equation was given by the Hartree mean-field method. The theory is then improved by Fock and Slater. In the Hartree-Fock method, we approximate the wave function of the total electron system based on the one-particle wave function $\psi_i(\boldsymbol{r})$ as a Slater determinant

$$\Psi_q^{\mathrm{el}}(\boldsymbol{r}_1, \boldsymbol{r}_2, \cdots, \boldsymbol{r}_N) = \frac{1}{\sqrt{N!}} \begin{vmatrix} \psi_1(\boldsymbol{r}_1) & \psi_1(\boldsymbol{r}_2) & \cdots & \psi_1(\boldsymbol{r}_N) \\ \psi_2(\boldsymbol{r}_1) & \psi_2(\boldsymbol{r}_2) & \cdots & \psi_2(\boldsymbol{r}_N) \\ \vdots & \vdots & \ddots & \vdots \\ \psi_N(\boldsymbol{r}_1) & \psi_N(\boldsymbol{r}_2) & \cdots & \psi_N(\boldsymbol{r}_N) \end{vmatrix} . \tag{2.6}$$

Here, we omit the dependence of $\{\boldsymbol{R}\}$ for simplicity. Thereby, we can simplify the effect of electron-electron interaction to that of mean-field

$$\begin{aligned} &\left[-\frac{\hbar^2}{2m}\nabla^2 + V_{\mathrm{ext}}(\boldsymbol{r}) + e^2 \int \mathrm{d}\boldsymbol{r}' \frac{n(\boldsymbol{r}')}{|\boldsymbol{r} - \boldsymbol{r}'|} \right] \psi_i(\boldsymbol{r}) \\ &\quad - e^2 \sum_j \int \mathrm{d}\boldsymbol{r}' \frac{\psi_j^*(\boldsymbol{r}')\psi_i(\boldsymbol{r}')}{|\boldsymbol{r} - \boldsymbol{r}'|} \psi_j(\boldsymbol{r}) = \varepsilon_i \psi_j(\boldsymbol{r}) \end{aligned} \tag{2.7}$$

Hartree-Fock approximation is used in some research fields. However, it often gives inaccurate physical quantities. For example, in a metal, the density of states of electrons vanishes on the Fermi surface. Furthermore, it is also computationally expensive.

In Hartree-Fock approximation, the energy of the system is given as a functional of one-particle wave function. On the contrary, another calculation method was suggested by Kohn and Hohenberg in 1964 [57]. In their theory, the electrons are treated not by the wave function of N electron system but by the density distribution function. The Hohenberg-Kohn's first theorem states that the electron density $n(\boldsymbol{r})$ can be a basic variable instead of N and $V_{\mathrm{ext}}(\boldsymbol{r})$. They found that the external potential $V_{\mathrm{ext}}(\boldsymbol{r})$ is determined uniquely, except for a constant shift for energy, from the ground state electron density. Since all the properties of the ground states are determined by N and $V_{\mathrm{ext}}(\boldsymbol{r})$, the theorem indicates that all electronic properties are determined from the electron density $n(\boldsymbol{r})$

$$E[n] = T[n] + V_{ee}[n] + \int \mathrm{d}\boldsymbol{r} V_{\mathrm{ext}}(\boldsymbol{r}) n(\boldsymbol{r}) \, , \tag{2.8}$$

where $T[n]$ is the kinetic term and $V_{ee}[n]$ indicates all contributions of the electron-electron interaction. Hohenberg-Kohn's second theorem formulates a variational principle for electron density not for wavefunction. That means there exists a functional for the energy $E[n]$ in terms of the density $n(\boldsymbol{r})$ which has a minimal values when $n(\boldsymbol{r})$ is the ground state density

$$E_0 = E[n_0] \leq E[n] \, , \tag{2.9}$$

where $n_0(\boldsymbol{r})$ represents the ground state density and E_0 is the ground state energy. In theses theorems, they assumes that there exists at least one external potential $v_{\text{ext}}(\boldsymbol{r})$ for a given electron density $n(\boldsymbol{r})$ where $n(\boldsymbol{r})$ gives the ground state density. This assumption is called the V-representability. However, this is not always the case. In fact, there exists many electron densities even in a single particle system that cannot be derived from the ground state wavefunction of any external potential. This condition can be reduced to N-representability: given the electron density $n(\boldsymbol{r})$ of a certain N-electron system, there always exists a wave function of the N-electron systems that reproduce this density $n(\boldsymbol{r})$.

2.3 Kohn-Sham Equation

From the Hohenberg-Kohn theorem, we can derive the Kohn-Sham equations [58]. They made an assumption that the exact ground state density can be expressed as the ground state density of an auxiliary non-interacting particle system. Therefore, energy functional $E[n]$ can be expressed in terms of several contributions

$$E[n] = T_s[n] + V_H[n] + \int \mathrm{d}^3 r \; n(\boldsymbol{r}) V_{\text{ext}}(\boldsymbol{r}) + E_{\text{xc}}[n] \, , \tag{2.10}$$

where the density of the auxiliary system is given by the sum of squares of the single electron wavefunctions

$$n(\boldsymbol{r}) = \sum_i |\psi_i(\boldsymbol{r})|^2 \, . \tag{2.11}$$

The first term on the right side is the kinetic energy term of non-interacting electrons

$$T_s[n] = \frac{\hbar^2}{2m} \sum_i \int \mathrm{d}^3 r \; |\nabla \psi_i(\boldsymbol{r})|^2 \, . \tag{2.12}$$

The second term is the Hartree energy which describes the classical Coulomb interaction between electrons

$$V_H[n] = \frac{e^2}{2} \int \mathrm{d}^3 r \int \mathrm{d}^3 r' \, \frac{n(\boldsymbol{r}) n(\boldsymbol{r}')}{|\boldsymbol{r} - \boldsymbol{r}'|} \, . \tag{2.13}$$

The third term describes the interaction between the electrons and external potentials. The last term is called the exchange-correlation energy in which all the difficult many-body terms are incorporated. Varying the wavefunction and applying the Hohenberg-Kohn theorem, Kohn-Sham Schrödinger-like equations can be obtained

$$\left[-\frac{\hbar^2}{2m} \nabla^2 + e^2 \int \mathrm{d}^3 r' \, \frac{n(\boldsymbol{r})}{|\boldsymbol{r} - \boldsymbol{r}'|} + V_{\mathrm{ext}}(\boldsymbol{r}) + V_{\mathrm{xc}}(\boldsymbol{r}) \right] \psi_i(\boldsymbol{r}) = \varepsilon_i \psi_i(\boldsymbol{r}) \, , \tag{2.14}$$

where $V_{\mathrm{xc}}(\boldsymbol{r})$ is given by

$$V_{\mathrm{xc}}(\boldsymbol{r}) = \frac{\delta E_{\mathrm{xc}}}{\delta n(\boldsymbol{r})} \, . \tag{2.15}$$

All we have to do is to solve this equation self-consistently.

2.4 Kohn-Sham-Dirac Equation

The relativistic extension of the density functional theory was formulated in 1970s by Rajagopal and Callaway [59] and Ramana and Rajagopal [60]. In the relativistic formulation, four-vector current takes over the role of the electron density. Therefore, the relativistic Hohenberg-Kohn theorem is changed so that the ground state energy is a unique functional of the ground state of four-vector current. The corresponding Kohn-Sham-Dirac equation is given as follows:

$$\left[c\boldsymbol{\alpha} \cdot (\boldsymbol{p} - e\boldsymbol{A}_{\mathrm{eff}}(\boldsymbol{r})) + \beta mc^2 + V_{\mathrm{eff}}(\boldsymbol{r}) \right] \psi_i(\boldsymbol{r}) = \varepsilon_i \psi_i(\boldsymbol{r}) \tag{2.16}$$

with

$$V_{\mathrm{eff}}(\boldsymbol{r}) = V_{\mathrm{ext}}(\boldsymbol{r}) + e^2 \int \mathrm{d}^3 r' \, \frac{n(\boldsymbol{r}')}{|\boldsymbol{r} - \boldsymbol{r}'|} + \frac{\delta E_{\mathrm{xc}}}{\delta n(\boldsymbol{r})} \, , \tag{2.17}$$

$$\boldsymbol{A}_{\mathrm{eff}}(\boldsymbol{r}) = \boldsymbol{A}_{\mathrm{ext}}(\boldsymbol{r}) + \frac{e}{c^2} \int \mathrm{d}^3 r' \, \frac{\boldsymbol{J}(\boldsymbol{r}')}{|\boldsymbol{r} - \boldsymbol{r}'|} + \frac{1}{e} \frac{\delta E_{\mathrm{xc}}}{\delta \boldsymbol{J}(\boldsymbol{r})} \, . \tag{2.18}$$

Here, $\boldsymbol{\alpha}$ and β is the standard 4×4 Dirac matrix [see Sec. 3.2 for the specific expression] and $\boldsymbol{J}(\boldsymbol{r})$ is given by

$$\boldsymbol{J}(\boldsymbol{r}) = c\sum_i \psi_i^\dagger(\boldsymbol{r})\boldsymbol{\alpha}\psi_i(\boldsymbol{r}) \ . \tag{2.19}$$

For the practical application, the four-vector current is split by the Gordon decomposition. The Kohn-Sham-Dirac equation can be simplified as

$$\left[c\boldsymbol{\alpha}\cdot\boldsymbol{p} + \beta mc^2 + V_{\text{eff}}(\boldsymbol{r}) + \beta\Sigma_z B_{\text{eff}}(\boldsymbol{r})\right]\psi_i(\boldsymbol{r}) = \varepsilon_i\psi_i(\boldsymbol{r}) \ , \tag{2.20}$$

with

$$V_{\text{eff}}(\boldsymbol{r}) = V_{\text{ext}}(\boldsymbol{r}) + e^2\int \mathrm{d}^3r' \ \frac{n(\boldsymbol{r})}{|\boldsymbol{r}-\boldsymbol{r}'|} + \frac{\delta E_{\text{xc}}[n(\boldsymbol{r}), m(\boldsymbol{r})]}{\delta n(\boldsymbol{r})} \ , \tag{2.21}$$

$$B_{\text{eff}}(\boldsymbol{r}) = B_{\text{ext}}(\boldsymbol{r}) + \frac{\delta E_{\text{xc}}[n(\boldsymbol{r}), m(\boldsymbol{r})]}{\delta m(\boldsymbol{r})} \ , \tag{2.22}$$

where $B_{\text{ext}}(\boldsymbol{r})$ is the external magnetic filed and $m(\boldsymbol{r})$ is the spin magnetic density

$$m(\boldsymbol{r}) = c\sum_i \psi_i^\dagger(\boldsymbol{r})\beta\Sigma_z\psi_i(\boldsymbol{r}) \ . \tag{2.23}$$

Chapter 3

KKR Green's Function Method

The Korringa-Kohn-Rostoker (KKR) Green's function method is one of the calculation methods for solving the Kohn-Sham or Kohn-Sham-Dirac equations. It was introduced as an electronic structure calculation method before the development of the density functional theory (DFT) in 1947 by Korringa [61] and in 1954 by Kohn and Rostoker [62]. The most prominent feature of the KKR Green's function method is that multiple scattering problem is expressed using the Green's function of the system. Unlike other general first-principles calculation methods, such as the standard pseudopotential-based methods or the linearized augmented plane wave (LAPW) method, the Green's function of the system is used already within the self-consistent field (SCF) calculation step when performing the KKR calculations. Therefore, it is easy to directly calculate physical quantities using the resulting Green's function or construct the Green's function for alloy systems by means of coherent potential approximation which will be introduced in Sec. 4.3. In this chapter we outlines the main idea of the KKR multiple scattering Green's function theory.

3.1 Non-relativistic Free Particle Green's Function

Before discussing the multiple scattering formalism of the Green's function, we will start from the most simple case, that is, non-relativistic and free-electron system. The wave function $\psi(\boldsymbol{r})$ of this system is described by the Schödinger equation as follows:

$$-\nabla_{\boldsymbol{r}}^2\psi(\boldsymbol{r}) = E\psi(\boldsymbol{r}) \ . \tag{3.1}$$

Here, we exploit the Rydberg atomic units of $\hbar = 2m = e^2/2 = 1$ for simplicity [1]. The corresponding Green's function is then defined by

$$(\nabla_{\boldsymbol{r}}^2 + E)G_{\mathrm{nr0}}(\boldsymbol{r}, \boldsymbol{r}', E) = \delta^3(\boldsymbol{r} - \boldsymbol{r}') \ . \tag{3.2}$$

This is a well-known Helmholtz equation whose solution is given by

$$G_{\mathrm{nr0}}^{\pm}(\boldsymbol{r}, \boldsymbol{r}', E) = -\frac{1}{4\pi}\frac{e^{\pm p|\boldsymbol{r}-\boldsymbol{r}'|}}{|\boldsymbol{r} - \boldsymbol{r}'|} \ , \tag{3.3}$$

where we define the momentum p as $p = \sqrt{E}$. As is evident from these solutions, the Green's function for free particle only depends on the difference in position $|\boldsymbol{r} - \boldsymbol{r}'|$. However, we explicitly write down the dependence of the positions of $\boldsymbol{r}$ and $\boldsymbol{r}'$ in the free-particle Green's function to develop the theory to multiple scattering case in the following sections. These two equations have a different behavior for $|\boldsymbol{r} - \boldsymbol{r}'| \to 0$. In a physical interpretation, $G_{\mathrm{nr0}}^{+}(\boldsymbol{r}, \boldsymbol{r}', E)$ describes outgoing wave while $G_{\mathrm{nr0}}^{-}(\boldsymbol{r}, \boldsymbol{r}', E)$ stands for incoming wave. As we have an interest in outgoing wave in the scattering theory, we focus only on $G_{\mathrm{nr0}}^{+}(\boldsymbol{r}, \boldsymbol{r}', E)$ and expressed it as $G_{\mathrm{nr0}}(\boldsymbol{r}, \boldsymbol{r}', E)$ hereafter.

For convenience of the computation, we exploit the spherical Bessel function $j_l(\sqrt{E}r)$ and the spherical Hankel function of the first kind $h_l^{(+)}(\sqrt{E}r)$ to describe the free particle Green's function

$$\begin{aligned} G_{\mathrm{nr0}}(\boldsymbol{r}, \boldsymbol{r}', E) = -ip\sum_L \big[& j_L(\boldsymbol{r}, E)\bar{h}_L^{(+)}(\boldsymbol{r}', E)\theta(r' - r) \\ & + h_L^{(+)}(\boldsymbol{r}, E)\bar{j}_L(\boldsymbol{r}', E)\theta(r - r')\big] \ , \end{aligned} \tag{3.4}$$

where $L = (l, m_l)$ is the combined quantum number of azimuthal quantum number l and magnetic quantum number m_l. Here, we also define the following functions:

$$j_L(\boldsymbol{r}, E) \equiv j_l(pr)Y_L(\hat{\boldsymbol{r}}) \ , \tag{3.5}$$

$$\bar{j}_L(\boldsymbol{r}, E) \equiv j_l(pr)Y_L^*(\hat{\boldsymbol{r}}) \ , \tag{3.6}$$

$$h_L^{(+)}(\boldsymbol{r}, E) \equiv h_l^{(+)}(pr)Y_L(\hat{\boldsymbol{r}}) \ , \tag{3.7}$$

$$\bar{h}_L^{(+)}(\boldsymbol{r}, E) \equiv h_l^{(+)}(pr)Y_L^*(\hat{\boldsymbol{r}}) \ . \tag{3.8}$$

[1] In DFT Hartree atomic units $\hbar = m = e = 1$ are also used. However, we always use Rydberg atomic unit in the following discussion.

Although we expressed the free particle Green's function using the complex spherical harmonics $Y_L(\hat{\boldsymbol{r}})$, the KKR calculations in Schrödinger formalism are usually performed by using real spherical harmonics. However, in the case of the relativistic formulation, we have to exploit the complex one.

3.2 Dirac Equation

Now we develop the free particle Green's function into a relativistic one. This is because that some terms such as Darwin and spin-orbit coupling terms are missing in the Schrödinger formalism. To deal with relativistic scattering we have to exploit the Dirac Hamiltonian. The Dirac Hamiltonian without a potential can be written as

$$\hat{H}_0(\boldsymbol{r}) = -ic\boldsymbol{\alpha} \cdot \boldsymbol{\nabla}_{\boldsymbol{r}} + \frac{1}{2}c^2\beta \tag{3.9}$$

where each 4×4 Dirac matrix is defined as

$$\alpha_i = \begin{pmatrix} 0 & \sigma_i \\ \sigma_i & 0 \end{pmatrix} , \qquad \beta = \begin{pmatrix} I_2 & 0 \\ 0 & I_2 \end{pmatrix} . \tag{3.10}$$

Here, the matrices α_i is composed by the Pauli matrices σ_i

$$\sigma_x = \begin{pmatrix} 0 & 1 \\ 1 & 0 \end{pmatrix} , \qquad \sigma_y = \begin{pmatrix} 0 & -i \\ i & 0 \end{pmatrix} , \qquad \sigma_z = \begin{pmatrix} 1 & 0 \\ 0 & -1 \end{pmatrix} . \tag{3.11}$$

3.2.1 Central Field

We will rewrite the Dirac equation using the polar coordinates. We first represent $\boldsymbol{\nabla}_{\boldsymbol{r}}$ in polar coordinates

$$\boldsymbol{\nabla}_{\boldsymbol{r}} = \hat{\boldsymbol{r}}\frac{\partial}{\partial r} - i\frac{\hat{\boldsymbol{r}}}{r} \times \boldsymbol{l} , \tag{3.12}$$

where $\boldsymbol{l}$ is the orbital angular momentum

$$\boldsymbol{l} = -i\boldsymbol{r} \times \boldsymbol{\nabla} . \tag{3.13}$$

By using this equation, the kinetic energy term of the Dirac equation is obtained in polar coordinates as

$$-ic\boldsymbol{\alpha} \cdot \boldsymbol{\nabla}_{\boldsymbol{r}} = -ic\gamma_5\sigma_r \left(\frac{\partial}{\partial r} + \frac{1}{r} - \frac{\beta}{r}K \right) , \tag{3.14}$$

where the operator σ_r is the projection of $\boldsymbol{\sigma}$

$$\sigma_r = \boldsymbol{\sigma} \cdot \hat{\boldsymbol{r}} \ , \tag{3.15}$$

and K is called the spin-orbit operator defined as

$$K = \beta(\boldsymbol{\sigma} \cdot \boldsymbol{l} + 1) \ . \tag{3.16}$$

The matrix γ_5 is given by

$$\gamma_5 = \begin{pmatrix} 0 & I_2 \\ I_2 & 0 \end{pmatrix} \ . \tag{3.17}$$

3.2.2 Spin-angular Part of the Dirac Equation

In non-relativistic quantum theory, the angular momentum is represented by the (l, m_l)-bases which is evident from Sec. 3.1. On the other hand, the relativistic quantum state is represented by using the (l, s, m_l, m_s)-bases, since further angular momentum $\boldsymbol{s}$ is included in the Dirac equation.

Schrödinger formalism	:	$\langle \hat{\boldsymbol{r}} \vert l, m_l \rangle = Y_l^{m_l}(\hat{\boldsymbol{r}})$
Dirac formalism	:	$\langle \hat{\boldsymbol{r}} \vert l, s; m_l, m_s \rangle = \langle \hat{\boldsymbol{r}} \vert \left(\vert l, m_l \rangle \otimes \vert s, m_s \rangle \right) = Y_l^{m_l}(\hat{\boldsymbol{r}}) \chi^{m_s}$

We can continue to develop the relativistic theory by using the (l, s, m_l, m_s)-bases in Dirac equations. However, it is more natural to add the angular momentum and represent the relativistic states by means of the (l, s, j, μ)-bases.

$$\langle \hat{\boldsymbol{r}} \vert l, s; j, \mu \rangle = \sum_{m_s} C(l, s, j; m_l, m_s, \mu) Y_l^{\mu - m_s}(\hat{\boldsymbol{r}}) \chi^{m_s} \tag{3.18}$$

Here, $C(l, s, j; m_l, m_s, \mu)$ indicates the Clebsch-Gordan coefficients. Especially in the theory of spin 1/2 of the Dirac equation, we use the quantum number called the relativistic spin-orbit quantum number $\kappa(l, j)$ and express the bases as

$$\begin{aligned} \chi_\kappa^\mu(\hat{\boldsymbol{r}}) &= \langle \hat{\boldsymbol{r}} \vert \kappa, \mu \rangle \\ &= \sum_{m_s = \pm \frac{1}{2}} C(l \tfrac{1}{2} j; \mu - m_s, m_s, \mu) Y_l^{\mu - m_s}(\hat{\boldsymbol{r}}) \chi^{m_s} \end{aligned} \tag{3.19}$$

which is called the spin-angular function or the spin spherical function. Here, the Clebsch-Gordan coefficients in case of the spin 1/2 are given by the following lists:

$$\begin{array}{c|cc} C(l\tfrac{1}{2}j;\mu-m_s,m_s,\mu) & m_s=\frac{1}{2} & m_s=-\frac{1}{2} \\ \hline j=l+\frac{1}{2} & \sqrt{\frac{l+\mu+\frac{1}{2}}{2l+1}} & \sqrt{\frac{l-\mu+\frac{1}{2}}{2l+1}} \\ j=l-\frac{1}{2} & -\sqrt{\frac{l-\mu+\frac{1}{2}}{2l+1}} & \sqrt{\frac{l+\mu+\frac{1}{2}}{2l+1}} \end{array} \tag{3.20}$$

3.2.3 Properties of Spin-angular Function

The relativistic spin-orbit quantum number κ is defined so that the eigen value of

$$(\boldsymbol{\sigma}\cdot\boldsymbol{l}+1)=\boldsymbol{j}^2-\boldsymbol{l}^2-\left(\frac{\boldsymbol{\sigma}}{2}\right)^2+1 \tag{3.21}$$

becomes $-\kappa$. If we explicitly write down the value of κ using the quantum numbers l and j, we obtain

$$\kappa=\begin{cases} -l-1 & (j=l+\frac{1}{2})\,, \\ l & (j=l-\frac{1}{2})\,. \end{cases} \tag{3.22}$$

Using the quantum number κ, we can express the properties of the spin-angular function as follows:

$$\boldsymbol{j}^2\chi_\Lambda(\hat{\boldsymbol{r}})=j(j+1)\chi_\Lambda(\hat{\boldsymbol{r}})\,, \tag{3.23}$$

$$j_z\chi_\Lambda(\hat{\boldsymbol{r}})=\mu\chi_\Lambda(\hat{\boldsymbol{r}})\,, \tag{3.24}$$

$$\boldsymbol{l}^2\chi_\Lambda(\hat{\boldsymbol{r}})=l(l+1)\chi_\Lambda(\hat{\boldsymbol{r}})\,, \tag{3.25}$$

$$\boldsymbol{\sigma}^2\chi_\Lambda(\hat{\boldsymbol{r}})=3\chi_\Lambda(\hat{\boldsymbol{r}})\,, \tag{3.26}$$

$$\sigma_r\chi_\Lambda(\hat{\boldsymbol{r}})=-\chi_{\bar{\Lambda}}(\hat{\boldsymbol{r}})\,, \tag{3.27}$$

$$K\begin{pmatrix}\chi_\Lambda(\hat{\boldsymbol{r}})\\ \chi_{\bar{\Lambda}}(\hat{\boldsymbol{r}})\end{pmatrix}=-\kappa\begin{pmatrix}\chi_\Lambda(\hat{\boldsymbol{r}})\\ \chi_{\bar{\Lambda}}(\hat{\boldsymbol{r}})\end{pmatrix}\,. \tag{3.28}$$

where we describe the combination of the quantum numbers κ and μ by the short form $\Lambda=(\kappa,\mu)$.

3.2.4 Quantum Numbers in spin 1/2 Dirac Equations

In the previous subsection, we define the relativistic spin-orbit quantum number κ in terms of l and j and vice versa the relation

$$l = \begin{cases} -\kappa - 1 & (\kappa < 0) \\ \kappa & (\kappa > 0) \end{cases} \tag{3.29}$$

can be obtained for the quantum number l. We will use some more quantum numbers which is defined in this subsection. First, we define the size and sign of κ as

$$k = |\kappa| \ , \tag{3.30}$$

$$S_\kappa = \kappa / k \ . \tag{3.31}$$

By using these quantities, the quantum number j can be expressed simply as

$$j = k - \frac{1}{2} = l - \frac{1}{2} S_\kappa \ . \tag{3.32}$$

We also define $\bar{l}$ which is the same as l but the sign of κ is different

$$\bar{l} = l_{-\kappa} = \begin{cases} -\kappa & (\kappa < 0) \ , \\ \kappa - 1 & (\kappa > 0) \ . \end{cases} \tag{3.33}$$

We listed the quantum numbers for selected orbitals in Table 3.1.

3.3 Solution of the Free Particle Dirac Equation

Since we obtained the free-particle Dirac equation in polar coordinates, we will focus on the solution of the Dirac equation. Unlike the case of the Schrödinger formalism, there are two solutions, namely right-hand side and left-hand side solutions in the case of the Dirac equation.

3.3.1 Right-hand Side Solution

Since we have defined all of the basic properties of the Dirac equation, we will derive the right-hand side solution of the Dirac equation for free-particle.

$$[E - \hat{H}_0(r)]\psi(\boldsymbol{r}, E) = \left[E + ic\gamma_5\sigma_r \left(\frac{\partial}{\partial r} + \frac{1}{r} - \frac{\beta}{r} K \right) - \frac{1}{2}\beta c^2 \right] \psi(\boldsymbol{r}, E) = 0 \ . \tag{3.34}$$

Table 3.1: Quantum Numbers for Selected Orbitals

Symbol of Orbital	l	$\bar{l}$	j	κ	μ
$s_{1/2}$	0	1	1/2	-1	-1/2
					+1/2
$p_{1/2}$	1	0	1/2	+1	-1/2
					+1/2
$p_{3/2}$	1	2	3/2	-2	-3/2
					-1/2
					+1/2
					+3/2
$d_{3/2}$	2	1	3/2	+2	-3/2
					-1/2
					+1/2
					+3/2
$d_{5/2}$	2	3	5/2	-3	-5/2
					-3/2
					-1/2
					+1/2
					+3/2
					+5/2
$f_{5/2}$	3	2	5/2	+3	-5/2
					-3/2
					-1/2
					+1/2
					+3/2
					+5/2

To obtain the radial equation, we separate the variables

$$\psi(\boldsymbol{r}, E) = \frac{1}{r} \sum_{\Lambda} \begin{pmatrix} P_{\Lambda}(r, E)\chi_{\Lambda}(\hat{\boldsymbol{r}}) \\ iQ_{\Lambda}(r, E)\chi_{\bar{\Lambda}}(\hat{\boldsymbol{r}}) \end{pmatrix} , \tag{3.35}$$

and substitute $\psi(\boldsymbol{r}, E)$ into the Dirac equation. It is straightforward to obtain the following coupled radial equations

$$\frac{\partial}{\partial r} P_{\Lambda}(r, E) + \frac{\kappa}{r} P_{\Lambda}(r, E) - \frac{E + c^2/2}{c} Q_{\Lambda}(r, E) = 0 , \tag{3.36}$$

$$\frac{\partial}{\partial r} Q_{\Lambda}(r, E) - \frac{\kappa}{r} Q_{\Lambda}(r, E) + \frac{E - c^2/2}{c} P_{\Lambda}(r, E) = 0 . \tag{3.37}$$

From these equations we can obtain relativistic spherical Bessel function

$$j_{\Lambda}(\boldsymbol{r}, E) = \sqrt{\frac{E + c^2/2}{c^2}} \begin{pmatrix} j_l(pr)\chi_{\Lambda}(\hat{\boldsymbol{r}}) \\ \frac{iS_{\kappa}pc}{E+c^2/2} j_{\bar{l}}(pr)\chi_{\bar{\Lambda}}(\hat{\boldsymbol{r}}) \end{pmatrix} \tag{3.38}$$

as a regular solution for $r \to 0$ and relativistic spherical Hankel function

$$h^{(+)}_{\Lambda}(\boldsymbol{r}, E) = \sqrt{\frac{E + c^2/2}{c^2}} \begin{pmatrix} h^{(+)}_{l}(pr)\chi_{\Lambda}(\hat{\boldsymbol{r}}) \\ \frac{iS_{\kappa}pc}{E+c^2/2} h^{(1)}_{\bar{l}}(pr)\chi_{\bar{\Lambda}}(\hat{\boldsymbol{r}}) \end{pmatrix} \tag{3.39}$$

as an irregular solution.

3.3.2 Left-hand Side Solution

Similarly, we can obtain the left-hand side solution of the Dirac equation

$$\psi^{\times}(\boldsymbol{r}, E)[E - \hat{H}_0(r)] = 0 \tag{3.40}$$

using the same method as the right-hand side case. We can obtain the relativistic spherical Bessel function for left-hand side solution

$$j^{\times}_{\Lambda}(\boldsymbol{r}, E) = \sqrt{\frac{E + c^2/2}{c^2}} \left(j_l(pr)\chi^{\dagger}_{\Lambda}(\hat{\boldsymbol{r}}) \quad \frac{-iS_{\kappa}pc}{E + c^2/2} j_{\bar{l}}(pr)\chi^{\dagger}_{\bar{\Lambda}}(\hat{\boldsymbol{r}}) \right) , \tag{3.41}$$

and relativistic spherical Hankel function

$$h^{(+)\times}_{\Lambda}(\boldsymbol{r}, E) = \sqrt{\frac{E + c^2/2}{c^2}} \left(h^{(+)}_{l}(pr)\chi^{\dagger}_{\Lambda}(\hat{\boldsymbol{r}}) \quad \frac{-iS_{\kappa}pc}{E + c^2/2} h^{(+)}_{\bar{l}}(pr)\chi^{\dagger}_{\bar{\Lambda}}(\hat{\boldsymbol{r}}) \right) . \tag{3.42}$$

3.4 Relativistic Free Particle Green's Function

We are now in the position of deriving the Green's function in Dirac formalism. For the derivation we exploit the following relation

$$[E - \hat{H}_0(\boldsymbol{r})][E + \hat{H}_0(\boldsymbol{r})] = c^2(\nabla^2 + p^2) \ , \tag{3.43}$$

where the moment p is given by $p^2c^2 = E^2 - c^2/4$ for relativistic case. By using this relation the relativistic Green's function for free paticle is given by

$$G_0(\boldsymbol{r}, \boldsymbol{r}', E) = \frac{1}{c^2}[E + H_0(\boldsymbol{r})]G_{\mathrm{nr}0}(\boldsymbol{r}, \boldsymbol{r}', E) \ . \tag{3.44}$$

Substituting the explicit expression for the non-relativistic Green's function $G_{\mathrm{nr}0}(\boldsymbol{r}, \boldsymbol{r}', E)$ in Eq. (3.4) we can obtain $G_0(\boldsymbol{r}, \boldsymbol{r}', E)$ as

$$\begin{aligned} G_0(\boldsymbol{r}, \boldsymbol{r}', E) = -ip \sum_{\Lambda} \big[& j_\Lambda(\boldsymbol{r}, E) h_\Lambda^{(+)\times}(\boldsymbol{r}', E)\theta(r' - r) \\ & + h_\Lambda^{(+)}(\boldsymbol{r}, E) j_\Lambda^{\times}(\boldsymbol{r}', E)\theta(r - r')\big] \ . \end{aligned} \tag{3.45}$$

3.5 Fourier Transform

The Green's function of the system under the potential $V(\boldsymbol{r})$ can be formally written as

$$G(\boldsymbol{r}, \boldsymbol{r}', E) = G_0(\boldsymbol{r}, \boldsymbol{r}', E) + \int_{\mathrm{all}} \mathrm{d}\boldsymbol{r}'' G_0(\boldsymbol{r}, \boldsymbol{r}'', E) V(\boldsymbol{r}'') G(\boldsymbol{r}'', \boldsymbol{r}, E) \ . \tag{3.46}$$

Using this equation we have to integrate over the whole region in a crystal. In the crystal the potential is periodic

$$V(\boldsymbol{r}_I + \boldsymbol{R}_I) = V(\boldsymbol{r}_I) \ , \tag{3.47}$$

where $\boldsymbol{R}_I$ is the Bravais lattice vector and subscript I indicates the I-th unit cell. Therefore, we Fourier transfer the Green's function

$$\mathcal{G}_{\boldsymbol{k}}(\boldsymbol{r}, \boldsymbol{r}'_0, E) = \sum_I G(\boldsymbol{r}, \boldsymbol{r}'_0 + \boldsymbol{R}_I, E) e^{i\boldsymbol{k}\cdot\boldsymbol{R}_I} \ , \tag{3.48}$$

and rewrite the Eq. (3.46) as

$$\mathcal{G}_{\boldsymbol{k}}(\boldsymbol{r}, \boldsymbol{r}'_0, E) = \mathcal{G}_{0\boldsymbol{k}}(\boldsymbol{r}, \boldsymbol{r}'_0, E) + \int_\Omega \mathrm{d}\boldsymbol{r}''_0 \mathcal{G}_{\boldsymbol{k}}(\boldsymbol{r}, \boldsymbol{r}''_0, E) V(\boldsymbol{r}''_0) \mathcal{G}_{0\boldsymbol{k}}(\boldsymbol{r}''_0, \boldsymbol{r}'_0, E) \ . \tag{3.49}$$

Here, the integral is changed to the one over a unit cell whose size is Ω.

3.6 Structure Constants

In the previous section, we successfully incorporate the crystal periodicity into the Green's function by using the Fourier transform. Next, we will manage the atomic-sites dependence in a unit cell. The strategy is to isolate the contribution of the atomic sites from the free particle Green's function. For simplicity, we will start in case of the non-relativistic Green's function $G_{\mathrm{nr0}}(\boldsymbol{r}, \boldsymbol{r}', E)$.

Suppose that the position vectors $\boldsymbol{r}_0$ and $\boldsymbol{r}'_0$ are located in the atomic site i and site j, respectively, of the reference unit cell

$$\boldsymbol{r}_0 = \boldsymbol{r}_i + \boldsymbol{Q}_i \quad \boldsymbol{r}'_0 = \boldsymbol{r}'_j + \boldsymbol{Q}_j \ , \tag{3.50}$$

where $\boldsymbol{Q}_i$ indicates the position vector of atomic site i. We can rewrite the Green's function as

$$\begin{aligned}\mathcal{G}_{\mathrm{nr0}\boldsymbol{k}}(\boldsymbol{r}_i + \boldsymbol{Q}_i, \boldsymbol{r}'_j + \boldsymbol{Q}_j, E) = \sum_{L,L'} j_L(\boldsymbol{r}_i, E)\mathcal{G}^{ij}_{\mathrm{nr0}LL'}(\boldsymbol{k}, E)\bar{j}_{L'}(\boldsymbol{r}'_j, E) \\ + \delta_{ij} G_{\mathrm{nr0}}(\boldsymbol{r}_i, \boldsymbol{r}'_j, E) \ .\end{aligned} \tag{3.51}$$

Here, all of the information about the configuration of atomic sites is included in $\mathcal{G}^{ij}_{\mathrm{nr0}LL'}(\boldsymbol{k}, E)$ which is called the structure constants

$$\begin{aligned}&\mathcal{G}^{ij}_{\mathrm{nr0}LL'}(\boldsymbol{k}, E) = \\ &\quad - 4\pi i p i^{l-l'} \sum_{L''} i^{-l''} \left[\sum_J (1 - \delta_{0J}\delta_{ij}) \bar{h}^{(+)}_{L''}(\boldsymbol{R}_J + \boldsymbol{Q}_j - \boldsymbol{Q}_i, E) e^{i\boldsymbol{k}\cdot\boldsymbol{R}_J} \right] C^{L''}_{LL'} \ ,\end{aligned} \tag{3.52}$$

where $C^{L''}_{LL'}$ is the Gaunt coefficients

$$C^{L''}_{LL'} = \int \mathrm{d}\hat{\boldsymbol{p}}\ Y^*_L(\hat{\boldsymbol{p}}) Y_{L'}(\hat{\boldsymbol{p}}) Y_{L''}(\hat{\boldsymbol{p}}) \ . \tag{3.53}$$

In the case of the Dirac formalism, we express the Green's function as

$$\begin{aligned}\mathcal{G}_{0\boldsymbol{k}}(\boldsymbol{r}_i + \boldsymbol{Q}_i, \boldsymbol{r}'_j + \boldsymbol{Q}_j, E) = \sum_{\Lambda,\Lambda'} j_\Lambda(\boldsymbol{r}_i, E)\mathcal{G}^{ij}_{0\Lambda\Lambda'}(\boldsymbol{k}, E)\bar{j}_{\Lambda'}(\boldsymbol{r}'_j, E) \\ + \delta_{ij} G_0(\boldsymbol{r}_i, \boldsymbol{r}'_j, E) \ .\end{aligned} \tag{3.54}$$

where the relativistic structure constant $\mathcal{G}^{ij}_{0\Lambda\Lambda'}(\boldsymbol{k}, E)$ is expressed using the non-relativistic one $\mathcal{G}^{ij}_{\mathrm{nr}0LL'}(\boldsymbol{k}, E)$ as follows:

$$\mathcal{G}^{ij}_{0\Lambda\Lambda'}(\boldsymbol{k}, E) = \sum_{m_s} C(l\tfrac{1}{2}j; \mu - m_s, m_s, \mu)\mathcal{G}^{ij}_{\mathrm{nr}0LL'}(\boldsymbol{k}, E) \times C(l'\tfrac{1}{2}j'; \mu' - m_s, m_s, \mu') \; . \tag{3.55}$$

For the purpose of the numerical calculation, we usually do not use the formulation given by Eq. (3.52). Since the Gaunt coefficients are calculated separately using the formulation

$$C^{L''}_{LL'} = \sqrt{\frac{(2l'+1)(2l''+1)}{2l+1}} C(l'l''l; m'm''m)C(l'l''l; 000) \; , \tag{3.56}$$

we introduce a new function $D^{ij}_L(\boldsymbol{k}, E)$

$$D^{ij}_L(\boldsymbol{k}, E) = -ip{\sum_J}' e^{i\boldsymbol{k}\cdot\boldsymbol{R}_J} \bar{h}^{(+)}_{L''}(\boldsymbol{R}_J + \boldsymbol{Q}_j - \boldsymbol{Q}_i, E) \; , \tag{3.57}$$

which is the rest part of the non-relativistic structure constants. Here, ${\sum_J}'$ indicates the sum over the J-th unit cell, but exclude the unit cell J if $\boldsymbol{R}_J + \boldsymbol{Q}_j - \boldsymbol{Q}_i$ vanishes. In integral form $D^{ij}_L(\boldsymbol{k}, E)$ can be rewritten as

$$D^{ij}_L(\boldsymbol{k}, E) = -\frac{2^{l+1}}{\sqrt{\pi}} p^{-l} {\sum_J}' |\boldsymbol{R}_J - (\boldsymbol{Q}_i - \boldsymbol{Q}_j)|^l e^{i\boldsymbol{k}\cdot\boldsymbol{R}_J} Y^*_L(\widehat{\boldsymbol{R}_J - (\boldsymbol{Q}_i - \boldsymbol{Q}_j)}) \times \int_0^\infty \mathrm{d}\zeta \; \zeta^{2l} \exp\left[-|\boldsymbol{R}_J - (\boldsymbol{Q}_i - \boldsymbol{Q}_j)|^2\zeta^2 + \frac{p^2}{4\zeta^2}\right] \; . \tag{3.58}$$

The problem for calculationg the equation above is that the integrand diverges when $\zeta \to 0$. Therefore, we have to break up the integral into two parts $[0, \sqrt{\eta}/2]$ and $[\sqrt{\eta}/2, \infty]$ with positive η. For the integral in the interval $[0, \sqrt{\eta}/2]$, we apply the Ewald's methods. For the final results, see the original work done by Ham and Segall [63].

3.7 Multiple Scattering

Since we have obtained the structure constants for the free particle Green's function, our next task is to derive a similar formalism for the Green's function in a periodic potential.

3.7.1 Dyson Equation

Suppose a Hamiltonian with an unperturbed reference system $\hat{H}_0$ and a potential V

$$\hat{H} = \hat{H}_0 + V \ . \tag{3.59}$$

The Green's function for the unperturbed system is the inverse operator of $(E - \hat{H}_0)$

$$G_0 = (E - \hat{H}_0)^{-1} \ . \tag{3.60}$$

The Green's function corresponding to the Hamiltonian $\hat{H}$ is then obtained by using G_0 as

$$\begin{aligned} G &= (E - \hat{H}_0 - V)^{-1} \\ &= (1 - G_0 V)^{-1} G_0 \\ &= G_0 + G_0 V G \ . \end{aligned} \tag{3.61}$$

This is the so-called Dyson equation which gives G in terms of self-consistent relation. The Dyson equation can also be rewritten as

$$\begin{aligned} G &= G_0 + G_0 V G_0 + G_0 V G_0 V + \cdots \\ &= G_0 + G_0 (V + V G_0 V + V G_0 V G_0 V + \cdots) G_0 \\ &= G_0 + G_0 T G_0 \ , \end{aligned} \tag{3.62}$$

where T is called the transition operator or T-operator

$$\begin{aligned} T &= V + V G_0 V + V G_0 V G_0 V + \cdots \\ &= V + V G_0 T \\ &= V + V G V \ . \end{aligned} \tag{3.63}$$

3.7.2 Scattering Path Operator

So far, we only considered the general potential V. To develop the theory to multiple scattering event, we split the potential V into a sum of non-overlapping potentials v_i centered at the atomic site i.

$$V = \sum_i v_i \tag{3.64}$$

There are several methods to divide the atomic sites in a crystal. The most sophisticated way is to use the Voroni polyhedra which is implemented in the full-potential calculations. In this case the potential is expanded by the spherical harmonics in the polyhedra which requires high computational effort. A better approach to reduce the computational time is to use the atomic sphere approximation (ASA). In the ASA method, we exploit spherical symmetric potentials to fill a unit cell. The total volume of the region where the potential is applied is taken to be the same as the volume of the unit cell, so that we allows for the overlap of the potential in the crystal. We can set the spread of the potential the same for all the atomic sites. However, it is often fail to obtain accurate physical quantities if we use the atomic sites having the same radius for all the components in the crystal. In the KKR methods, there are two prescriptions to resolve the problem. The easiest way is to use the experimental values of the muffin-tin radius and enlarge them to fit the size of the unit cell. We can also exploit the Hartree potential and avoid to use the empirical values. In the case of using the Hartree potential, we first calculate the Hartree potential in the crystal space and divide between the atomic sites at the point where the potential takes minimum. The problem of the ASA method is that we cannot get good results when the overlap of the potential is large. To avoid the problem the vacancy is set in the empty space of the crystal structure.

Now, the T-operator is written as

$$T = \sum_i v_i + \sum_i v_i G_0 T \ . \tag{3.65}$$

As an alternative expression of the scattering events, we express the T-operator in terms of the so-called scattering path operator τ^{ij}

$$T = \sum_{i,j} \tau^{ij} \ , \tag{3.66}$$

which was first introduced by Gyorffy and Stott [64]. Here, τ^{ij} describes the scattering events starting at site i and finishing at site j. Using the scattering path operator, we can rewrite Eq. (3.65) as

$$\tau^{ij} = t^i \delta_{ij} + \sum_k t^i G_0 (1 - \delta_{ik}) \tau^{kj} \ , \tag{3.67}$$

where t-matrix t^i is given by

$$t^i = v^i + v^i G_0 t^i \ . \tag{3.68}$$

3.7.3 Multiple Scattering in the KKR Methods

For a practical calculation we will describe the scattering path operator for a set of specific basis functions. We explicitly write down Eq. (3.67) in terms of the position vector

$$\begin{aligned}\tau^{0iJj}(\boldsymbol{r}_i, \boldsymbol{r}'_j, E) = t^i(\boldsymbol{r}_i, \boldsymbol{r}'_j, E)\delta_{0J}\delta_{ij} \\ + \sum_{Ss(\neq 0i)} \int_{\text{all}} \mathrm{d}\boldsymbol{r}'' \int_{\text{all}} \mathrm{d}\boldsymbol{r}''' t^i(\boldsymbol{r}_i, \boldsymbol{r}'' - \boldsymbol{Q}_i, E) G_0(\boldsymbol{r}'', \boldsymbol{r}''', E) \\ \times \tau^{SsJj}(\boldsymbol{r}''' - \boldsymbol{R}_S - \boldsymbol{Q}_s, \boldsymbol{r}'_j, E)\end{aligned} \tag{3.69}$$

where we express the indices of the unit cell by uppercase and the indices of the atomic site in lowercase. Expressed the above scattering path operator as the basis of the Bessel functions, we obtain the following equation:

$$\begin{aligned}\tau^{ij}_{\Lambda\Lambda'}(\boldsymbol{k}, E) =& \int_{\Omega_i} \mathrm{d}\boldsymbol{r}_i \int_{\Omega_j} \mathrm{d}\boldsymbol{r}'_j j^{i\times}_{\Lambda}(\boldsymbol{r}_i, E) \sum_J \tau^{0iJj}(\boldsymbol{r}_i, \boldsymbol{r}'_j, E) e^{i\boldsymbol{k}\cdot\boldsymbol{R}_J} j^j_{\Lambda'}(\boldsymbol{r}'_j, E) \\ =& t^i_{\Lambda\Lambda'}(E)\delta_{ij} + \sum_{\Lambda'',\Lambda'''} \sum_s t^i_{\Lambda''\Lambda'''}(E) \mathcal{G}^{is}_{0\Lambda''\Lambda'''}(\boldsymbol{k}, E) \tau^{sj}(\boldsymbol{k}, E)\end{aligned} \tag{3.70}$$

In matrix form this equation can be written as

$$\underline{\underline{\tau}}(\boldsymbol{k}, E) = \left[\underline{\underline{t}}^{-1}(E) - \underline{\underline{\mathcal{G}}}_0(\boldsymbol{k}, E)\right]^{-1} \tag{3.71}$$

where

$$\left[\underline{\underline{\tau}}(\boldsymbol{k}, E)\right]^{ij}_{\Lambda\Lambda'} = \tau^{ij}_{\Lambda\Lambda'}(\boldsymbol{k}, E) \ , \tag{3.72}$$

$$\left[\underline{\underline{t}}(E)\right]^{ij}_{\Lambda\Lambda'} = \delta_{ij} t^i_{\Lambda\Lambda'}(E) \ , \tag{3.73}$$

$$\left[\underline{\underline{\mathcal{G}}}_0(\boldsymbol{k}, E)\right]^{ij}_{\Lambda\Lambda'} = \mathcal{G}^{ij}_{0\Lambda\Lambda'}(\boldsymbol{k}, E) \ . \tag{3.74}$$

Using the scattering path operator $\underline{\underline{\tau}}(\boldsymbol{k}, E)$ we can derive the following multiple scattering Green's function:

$$\begin{aligned}\mathcal{G}_{\boldsymbol{k}}(\boldsymbol{r}_i + \boldsymbol{Q}_i, \boldsymbol{r}'_j + \boldsymbol{Q}_j, E) = \sum_{\Lambda,\Lambda'} R^i_{\Lambda}(\boldsymbol{r}_i, E) \mathcal{G}^{ij}_{\Lambda\Lambda'}(\boldsymbol{k}, E) R^{j\times}_{\Lambda'}(\boldsymbol{r}'_j, E) \\ + \delta_{ij} G(\boldsymbol{r}_i, \boldsymbol{r}'_j, E) \ ,\end{aligned} \tag{3.75}$$

where $R^i_\Lambda(\boldsymbol{r}_i, E)$ and $R^{i\times}_\Lambda(\boldsymbol{r}_i, E)$ are the angular momentum Lippmann-Schwinger equations for the regular solutions

$$\begin{aligned} R^i_\Lambda(\boldsymbol{r}_i, E) &= j^i_\Lambda(\boldsymbol{r}_i, E) \\ &\quad + \int_{\Omega_i} \mathrm{d}\boldsymbol{r}'_i \int_{\Omega_i} \mathrm{d}\boldsymbol{r}''_i G_0(\boldsymbol{r}_i, \boldsymbol{r}'_i, E) t^i(\boldsymbol{r}'_i, \boldsymbol{r}''_i, E) j^i_\Lambda(\boldsymbol{r}''_i, E) \ , \end{aligned} \tag{3.76}$$

$$\begin{aligned} R^{i\times}_\Lambda(\boldsymbol{r}_i, E) &= j^{i\times}_\Lambda(\boldsymbol{r}_i, E) \\ &\quad + \int_{\Omega_i} \mathrm{d}\boldsymbol{r}'_i \int_{\Omega_i} \mathrm{d}\boldsymbol{r}''_i j^{i\times}_\Lambda(\boldsymbol{r}''_i, E) t^i(\boldsymbol{r}''_i, \boldsymbol{r}'_i, E) G_0(\boldsymbol{r}'_i, \boldsymbol{r}_i, E) \ , \end{aligned} \tag{3.77}$$

and $G(\boldsymbol{r}_i, \boldsymbol{r}'_i, E)$ is the Green's function for single-site scattering

$$\begin{aligned} G(\boldsymbol{r}_i, \boldsymbol{r}'_i, E) &= G_0(\boldsymbol{r}_i, \boldsymbol{r}'_i, E) \\ &\quad + \int_{\Omega_i} \mathrm{d}\boldsymbol{r}''_i \int_{\Omega_i} \mathrm{d}\boldsymbol{r}'''_i G_0(\boldsymbol{r}_i, \boldsymbol{r}''_i, E) t^i(\boldsymbol{r}''_i, \boldsymbol{r}'''_i, E) G_0(\boldsymbol{r}'''_i, \boldsymbol{r}'_i, E) \\ &= G_0(\boldsymbol{r}_i, \boldsymbol{r}'_i, E) + \int_{\Omega_i} \mathrm{d}\boldsymbol{r}''_i G_0(\boldsymbol{r}_i, \boldsymbol{r}''_i, E) V^i(\boldsymbol{r}''_i) G(\boldsymbol{r}''_i, \boldsymbol{r}'_i, E) \ . \end{aligned} \tag{3.78}$$

The multiple scattering equivalent of the structure constant $\mathcal{G}^{ij}_{\Lambda\Lambda'}(\boldsymbol{k}, E)$ is given by the structure constants $\mathcal{G}^{ij}_{0\Lambda\Lambda'}(\boldsymbol{k}, E)$ and the scattering path operator $\tau^{ij}_{\Lambda'\Lambda'}(\boldsymbol{k}, E)$

$$\begin{aligned} \mathcal{G}^{ij}_{\Lambda\Lambda'}(\boldsymbol{k}, E) &= \mathcal{G}^{ij}_{0\Lambda\Lambda'}(\boldsymbol{k}, E) \\ &\quad + \sum_{\Lambda'',\Lambda'''} \sum_{s,u} \mathcal{G}^{is}_{0\Lambda\Lambda''}(\boldsymbol{k}, E) \tau^{su}_{\Lambda''\Lambda'''}(\boldsymbol{k}, E) \mathcal{G}^{uj}_{0\Lambda'''\Lambda'}(\boldsymbol{k}, E) \ . \end{aligned} \tag{3.79}$$

3.8 Green's Function for a Particle in a Potential

In the previous section, we found that the multiple scattering Green's function is provided using the Lippmann-Schwinger equations $R^i_\Lambda(\boldsymbol{r}_i, E)$, multiple scattering equivalent of the structure constants $\mathcal{G}^{ij}_{\Lambda\Lambda'}(\boldsymbol{k}, E)$, and the Green's function for the single-site scattering $G(\boldsymbol{r}_i, \boldsymbol{r}'_i, E)$. We have presented the formulation of $\mathcal{G}^{ij}_{\Lambda\Lambda'}(\boldsymbol{k}, E)$ in the previous section. Concerning $R^i_\Lambda(\boldsymbol{r}_i, E)$, we will discuss in the next section. The Green's function for the single-site scattering has a structure very similar to that of free particle in Eq. (3.45)

$$\begin{aligned} G_0(\boldsymbol{r}_i, \boldsymbol{r}'_i, E) = -ip \sum_\Lambda \big[& R^i_\Lambda(\boldsymbol{r}_i, E) S^{i\times}_\Lambda(\boldsymbol{r}'_i, E) \theta(r'_i - r_i) \\ & + S^i_\Lambda(\boldsymbol{r}_i, E) R^{i\times}_\Lambda(\boldsymbol{r}'_i, E) \theta(r_i - r'_i) \big] \ . \end{aligned} \tag{3.80}$$

where $R^i_\Lambda(\boldsymbol{r}_i, E)$ is the angular momentum Lippmann-Schwinger equation for the regular solutions defined by Eq. (3.76). On the contrary, $S^i_\Lambda(\boldsymbol{r}_i, E)$ and $S^{i\times}_\Lambda(\boldsymbol{r}_i, E)$ are the angular momentum Lippmann-Schwinger equations for the irregular solutions

$$S^i_\Lambda(\boldsymbol{r}_i, E) = \sum_{\Lambda'} h^i_{\Lambda'}(\boldsymbol{r}_i, E)\beta_{\Lambda'\Lambda} + \int_{\Omega_i} \mathrm{d}\boldsymbol{r}'_i \; G_0(\boldsymbol{r}_i, \boldsymbol{r}'_i, E)V^i(\boldsymbol{r}'_i)S^i_\Lambda(\boldsymbol{r}'_i, E) \; , \tag{3.81}$$

$$S^{i\times}_\Lambda(\boldsymbol{r}_i, E) = \sum_{\Lambda'} \bar{\beta}_{\Lambda\Lambda'} h^i_{\Lambda'}(\boldsymbol{r}_i, E) + \int_{\Omega_i} \mathrm{d}\boldsymbol{r}'_i \; S^{i\times}_\Lambda(\boldsymbol{r}'_i, E)V^i(\boldsymbol{r}'_i)G_0(\boldsymbol{r}'_i, \boldsymbol{r}_i, E) \; . \tag{3.82}$$

where $\beta_{\Lambda'\Lambda}$ and $\bar{\beta}_{\Lambda\Lambda'}$ are given by

$$\beta_{\Lambda'\Lambda} = \delta_{\Lambda\Lambda'} + ip \int_{\Omega_i} \mathrm{d}\boldsymbol{r}'_i \; j^{i\times}_\Lambda(\boldsymbol{r}'_i, E)V^i(\boldsymbol{r}'_i)S^i_\Lambda(\boldsymbol{r}'_i, E) \; , \tag{3.83}$$

$$\bar{\beta}_{\Lambda\Lambda'} = \delta_{\Lambda\Lambda'} + ip \int_{\Omega_i} \mathrm{d}\boldsymbol{r}'_i \; S^{i\times}_\Lambda(\boldsymbol{r}'_i, E)V^i(\boldsymbol{r}'_i)j^i_\Lambda(\boldsymbol{r}'_i, E) \; , \tag{3.84}$$

so that the wavefunction outside the potential is set to match the Hankel function of the first kind.

3.9 Radial Equations

In this section we mention the calculation method of the Lippmann-Schwinger equations for the regular solutions $R^i_\Lambda(\boldsymbol{r}_i, E)$ and irregular solutions $S^i_\Lambda(\boldsymbol{r}_i, E)$. Here, again, we explicitly write down the solutions $R^i_\Lambda(\boldsymbol{r}_i, E)$ and $S^i_\Lambda(\boldsymbol{r}_i, E)$ in the same way as in Eq. (3.35). Substituting Eq. (3.35) for the Kohn-Sham-Dirac equations [Eq. (2.20)] we can obtain the following equations:

$$\begin{aligned}\frac{\partial}{\partial r}P_\Lambda(r, E) = &-\frac{\kappa}{r}P_\Lambda(r, E) + \left[\frac{E - V_{\text{eff}}(r)}{c} + \frac{c}{2}\right] Q_\Lambda(r, E) \\ &+ \frac{B_{\text{eff}}(r)}{c} \sum_{\Lambda'} \langle \chi_{\bar{\Lambda}} | \sigma_z | \chi_{\bar{\Lambda}'} \rangle Q_{\Lambda'}(r, E)\end{aligned} \tag{3.85}$$

$$\begin{aligned}\frac{\partial}{\partial r}Q_\Lambda(r, E) = &\frac{\kappa}{r}Q_\Lambda(r, E) - \left[\frac{E - V_{\text{eff}}(r)}{c} - \frac{c}{2}\right] P_\Lambda(r, E) \\ &+ \frac{B_{\text{eff}}(r)}{c} \sum_{\Lambda'} \langle \chi_{\Lambda} | \sigma_z | \chi_{\Lambda'} \rangle P_{\Lambda'}(r, E)\end{aligned} \tag{3.86}$$

where $\langle\chi_\Lambda|\sigma_z|\chi_{\Lambda'}\rangle$ is given by

$$\langle\chi_\Lambda|\sigma_z|\chi_{\Lambda'}\rangle = \begin{cases} -\dfrac{\mu}{\kappa+\frac{1}{2}}\ , & (\kappa=\kappa') \\ -\sqrt{1-\dfrac{\mu^2}{(\kappa+\frac{1}{2})^2}}\ , & (\kappa=-\kappa'-1) \\ 0\ . & (\text{otherwise}) \end{cases} \tag{3.87}$$

Here, we only use the expected values of the Pauli matrix in the z-direction. This is because that the expected values of other matrices σ_x and σ_y have more complicated forms. Since $R^i_\Lambda(\boldsymbol{r}_i, E)$ is regular at the center of the atomic sites, we start the calculation from the center of the atomic sites and perform the outward integral to obtain the wave function of the whole space. On the contrary, we perform the inward integral to obtain irregular solutions $S^i_\Lambda(\boldsymbol{r}_i, E)$ since we know $S^i_\Lambda(\boldsymbol{r}_i, E)$ is the same as the Hankel function of the first kind outside the potential as is evident from Eq. (3.81).

Chapter 4

Calculation of the Disordered System

In this chapter we focus on the calculation method of electronic structure of substitutional alloy systems. It has a long history from the 1930s [9, 10, 11]. The only practical way for the calculation of the alloy systems is the coherent potential approximation. However, we also mention the formulation of other methods such as virtual crystal approximation and average t-matrix approximation to compare with the methods we will use later. We will also present the formulation of the coherent potential approximation in terms of the scattering path operators to represents methods used in the KKR calculations. In the last section of this chapter, we will introduce the specific algorithm for the calculation of alloys.

4.1 Virtual Crystal Approximation (VCA)

The simplest approach for calculations on alloys is the virtual crystal approximation first introdued by Nordheim [12] and Muto [13]. Let us consider the Hamiltonian $\hat{H} = \hat{H}_0 + V$, where $\hat{H}_0$ is the periodic part of the Hamiltonian and V is the potential that reflects the randomness of the configuration of components in alloys. As the Green's function of the system G is given formally by $G = G_0 + G_0 V G$ using the Green's function G_0 derived from $\hat{H}_0$, the configuration average of the Green's function $\langle G \rangle$ can be written as

$$\langle G \rangle = G_0 + G_0 \langle VG \rangle \ . \tag{4.1}$$

If we make the approximation

$$\langle VG \rangle \approx \langle V \rangle \langle G \rangle \ , \tag{4.2}$$

and take into account that the configuration average of the potential can be expressed by the concentration average of the potential of the components that forms an alloy

$$\langle V \rangle \approx \sum_{\alpha} c_{\alpha} v_{\alpha} \ , \tag{4.3}$$

we obtain the VCA. Here, the subscript α is the index for the atom types in the alloy, c_{α} and and v_{α} are the concentration and the on-site potential, respectively, of atom α.

The VCA seems to be a good approximation for metals having a simple free-electron like electronic structure such as Na, K, and Al. However, it is known that the VCA completely fails to yield correct physical properties for the transition-metal alloys [10]. In particular, the VCA fails to describe element specific properties of an alloy as it is relevant for example in hyperfine interaction [9].

4.2 Average t-matrix Approximation (ATA)

The short coming of the VCA has been removed by Korringa [14] and Beeby [15] by introducing the so-called average t-matrix approximation (ATA). Within this approach, the concentration average of the single-site scattering matrix, the t-matrix, is used instead of the potential allowing to consider component-projected properties. We summarize the concept of the ATA in the following.

We first express the Green's function of the substitutional random alloys using the total scattering operator T,

$$G = G_0 + G_0 T G_0 \ . \tag{4.4}$$

The total scattering operator T can be divided depending on its scattering path as follows:

$$T = \sum_{mn} \tau^{mn} \ . \tag{4.5}$$

where the operator τ^{mn} is the scattering path operator that accounts for all scattering events connecting site m and site n. By using the single-site scattering matrix, t-matrix, we can apply the following Dyson equation:

$$\begin{aligned}\tau^{mn} &= t^m\delta_{mn} + \sum_k t^m G_0(1-\delta_{mk})\tau^{kn} \\ &= t^m\delta_{mn} + \sum_k t^m G_0(1-\delta_{mn})t^n \ + \sum_k t^m G_0(1-\delta_{mk})t^k G_0(1-\delta_{kn})t^n + \cdots \ .\end{aligned} \tag{4.6}$$

In the case of the ATA, we use the concentration average of the t-matrix

$$\langle t^n \rangle = \sum_\alpha c_\alpha t_\alpha^n \ , \tag{4.7}$$

instead t^n when we take the configuration average of the total scattering operator $\langle T \rangle$.

The ATA became a big step to the calculation of alloys. However, the ATA still has formal problems leading sometimes to unphysical results [9].

4.3 Coherent Potential Approximation (CPA)

The most sophisticated single-site method available for the calculation of homogeneous random alloys that solves these problems is provided by the coherent potential approximation (CPA). The CPA is a mean-filed theory that treats alloys by introducing an effective medium that can be defined by its average scattering properties first proposed by Soven [16] and Taylor [17]. In case of the CPA, we express the Green's function as follows:

$$G = G_c T_{c\to\mathrm{exa}} G_c \ , \tag{4.8}$$

where G_c is the Green's function derived from the fictitious coherent potential and $T_{c\to\mathrm{exa}}(E)$ is the scattering operator that replace the coherent potential to the exact potential of the substitutional random alloys. Although the Green's function of the exact system G does not have the crystal symmetry, G_c is determined so that it has the full symmetry of the periodic crystals. The basic concept of the CPA is that we find the G_c such that the configuration average of the scattering operator vanishes:

$$\langle T_{c\to\mathrm{exa}} \rangle = 0 \ . \tag{4.9}$$

In other words, embedding one of the alloy components into the CPA should in average lead to no additional scattering within the framework of multiple scattering formalism. Accordingly, unlike for the VCA and ATA methods, one has to determine the effective medium self-consistently in the case of the CPA calculations.

In the following section, we first derive the CPA condition. There are several approaches to the CPA that use perturbation method, interpolation method, cumulant expansion method, etc. summarized in the review [65]. However, all of these methods give the same results.

4.3.1 Derivation of the CPA Condition

In this subsection, we derive the CPA condition that is common to all of the calculation methods. For the specific case of the KKR-CPA method, we derive the condition in the following subsection. Here, we follow the approach given by Veliký et al. [66] for the derivation of the CPA condition.

We express the Hamiltonian of a certain substitutional random alloys as H_{exa}. The Green's function of the system is given by

$$G(E) = (E - H_{\mathrm{ext}})^{-1} \, . \tag{4.10}$$

We then divide the Hamiltonian into the priodic part H_c having the crystal symmetry and the remains $V_{\mathrm{exa}-c} = H_{\mathrm{exa}} - H_c$. By defining the Green's function given by the periodic Hamiltonian H_c as

$$G_c(E) = (E - H_c(E))^{-1} \, , \tag{4.11}$$

the Green's function of the exact Hamiltonian $G(E)$ is expressed by $G_c(E)$ as follows:

$$G(E) = G_c(E) + G_c(E)\tilde{T}(E)G_c(E) \tag{4.12}$$

where $\tilde{T}(E)$ is given by

$$\tilde{T}(E) = V_{\mathrm{exa}-c}[1 + G_c(E)\tilde{T}(E)] \, . \tag{4.13}$$

Here, $\tilde{T}(E)$ is not the total scattering operator in the usual sense. The operator $\tilde{T}(E)$ changes the Green's function $G_c(E)$ to the Green's function of the exact system $G(E)$.

We represent the operator using tilde. By taking the random average of $G(E)$, we obtain

$$\langle G(E)\rangle = G_c(E) + G_c(E)\,\langle \tilde{T}(E)\rangle\, G_c(E)\ . \tag{4.14}$$

If $\langle \tilde{T}(E)\rangle$ vanishes, the random average of the Green's function $\langle G(E)\rangle$ becomes the same as $G_c(E)$. Concerning the Hamiltonian, we assume that $\langle G(E)\rangle$ is expressed by the Hamiltonian $H_{\rm CPA}$ as

$$\langle G(E)\rangle = (E - H_{\rm CPA})^{-1}\ . \tag{4.15}$$

If we rewrite the Hamiltonian in terms of $H_{\rm CPA}$, we obtain

$$H_{\rm CPA} = H_c + \langle \tilde{T}(E)\rangle\,[1 + G_c(E)\,\langle \tilde{T}(E)\rangle]\ . \tag{4.16}$$

Here, again, we obtain $H_{\rm CPA} = H_c$ in case of the condition $\langle \tilde{T}(E)\rangle = 0$.

The CPA condition $\langle \tilde{T}(E)\rangle = 0$ is not useful in actual calculations, the single-site approximation (SSA) is usually applied. Next, we derive the CPA-SSA condition. Suppose that we can divide the disordered potential $V_{{\rm exa}-c}$ by site

$$V_{{\rm exa}-c}(E) = \sum_i v^i_{{\rm exa}-c}(E)\ . \tag{4.17}$$

Therefore, $\tilde{T}(E)$ can be divided as well

$$\tilde{T}(E) = \sum_i Q^i(E) = \sum_i v^i_{{\rm exa}-c}(E)[1 + G_c(E)\tilde{T}(E)]\ , \tag{4.18}$$

where $Q^i(E)$ is given by

$$Q^i(E) = \tilde{t}^i(E)\left[1 + G_c(E)\sum_{j(\neq i)} Q^j(E)\right]\ . \tag{4.19}$$

Here, we use the expression $\tilde{t}^i(E) = v^i_{{\rm exa}-c}(E)[1 - G_c(E)v^i_{{\rm exa}-c}(E)]^{-1}$. The $\tilde{t}^i(E)$ is the single-site correspondence of the operator $\tilde{T}(E)$ in which the fictitious coherent potential of site i is replaced by the potential of the exact atom of a substitutional random alloy. If we take the random average of $Q^i(E)$ in the equation above, we obtain the following equation:

$$\langle Q^i(E)\rangle = \langle \tilde{t}^i(E)\rangle\left[1 + G_c(E)\sum_{j(\neq i)}\langle Q^j(E)\rangle\right] + \left\langle \tilde{t}^i(E)G_c(E)\sum_{j(\neq i)}[Q^j(E) - \langle Q^j(E)\rangle]\right\rangle\ . \tag{4.20}$$

Here, the first term is the average in site i, and the second term is the fluctuation. The SSA condition refers to the approximation that ignores this second term.

$$\langle Q^i(E)\rangle \approx \langle \tilde{t}^i(E)\rangle \left[1 + G_c(E) \sum_{j(\neq i)} \langle Q^j(E)\rangle\right] . \tag{4.21}$$

Under the condition of the SSA, we can exploit

$$\langle \tilde{t}^i(E)\rangle = 0 , \qquad (\forall i) \tag{4.22}$$

in stead of $\tilde{T}(E) = 0$.

4.4 KKR-CPA Method

Since the CPA condition is obtained in the previous section, we then focus on how to apply the CPA to the KKR method. This is a quite important step for the application of the CPA method to actual calculations because the methodology of the CPA is well-established from 1970s as well as the several effective algorithm for solving the CPA condition is well-developed in the KKR formalism. In the following, we will rewrite the CPA condition in terms of the scattering path operator, projection matrix, and the excess scattering operator that can be applied to the KKR-CPA calculations. Then, we mention the computational method used for the KKR-CPA method.

4.4.1 Representation by the Scattering Path Operator

In this subsection, we follow the discussion in Ref. [20] to derive the CPA condition in terms of the scattering path operator for the application of the KKR formalism. We consider the Hamiltonian with a potential v^i_α of atom α on site i of the crystal

$$H_\alpha = H_0 + V_\alpha , \tag{4.23}$$

and the Hamiltonian having coherent potential v^i_c on site i.

$$H_{\rm c} = H_0 + V_{\rm c}(E) . \tag{4.24}$$

If each atoms is randomly mixed with the concentration of c_α on site i, we can write the CPA condition as

$$\langle \tilde{t}^i(E) \rangle = \sum_\alpha c_\alpha \tilde{t}^i_\alpha(E) = 0 \ , \tag{4.25}$$

$$\tilde{t}^i_\alpha(E) = (v^i_\alpha - v^i_c(E)) + (v^i_\alpha - v^i_c(E)) G_c(E) \tilde{t}^i_\alpha(E) \ . \tag{4.26}$$

Using the operator $\tilde{t}^i_\alpha(E)$, we can express the Green's function given by the Hamiltonian H_α as follows:

$$G_\alpha(E) = G_c(E) + G_c(E) \tilde{t}^i_\alpha(E) G_c(E) \ . \tag{4.27}$$

The equation above is also rewritten formally as

$$G_\alpha(E) = G_0(E) + G_0(E) T_\alpha(E) G_0(E) \ . \tag{4.28}$$

Using Eq. (4.25) the CPA condition can be expressed using the Green's function as

$$\sum_\alpha c_\alpha G_\alpha(E) = G_c(E) + G_c(E) \sum_\alpha c_\alpha \tilde{t}^i_\alpha(E) G_c(E) = G_c(E) \ , \tag{4.29}$$

but this is the same as

$$G_c(E) = G_0(E) + G_0(E) T_c(E) G_0(E) \ , \tag{4.30}$$

$$T_c(E) = \sum_\alpha c_\alpha T_\alpha(E) \ . \tag{4.31}$$

Since we can rewrite the CPA condition in terms of the total scattering operator, we then represent it exploiting the scattering path operator. There is a relation between the total scattering operator and the scattering path operator expressed as

$$T(\boldsymbol{r}_i, \boldsymbol{r}'_j + \boldsymbol{R}_J + \boldsymbol{Q}_j, E) = \tau^{0iJj}(\boldsymbol{r}_i, \boldsymbol{r}'_j, E) \ . \tag{4.32}$$

Here, we use the real-space representation. In the KKR-CPA method, we can obtain the expected value of the scattering path operator in the Bessel function

$$\begin{aligned} \tau^{0iJj}_{\Lambda\Lambda'}(E) &= \int_{\Omega_i} \mathrm{d}\boldsymbol{r}_i \int_{\Omega_j} \mathrm{d}\boldsymbol{r}_j \ \bar{j}^i_\Lambda(\boldsymbol{r}_i, E) \tau^{0iJj}(\boldsymbol{r}_i, \boldsymbol{r}'_j, E) \bar{j}^j_{\Lambda'}(\boldsymbol{r}_i, E) \\ &= \frac{1}{\Omega_{\mathrm{BZ}}} \int_{\mathrm{BZ}} \mathrm{d}\boldsymbol{k} \ \tau^{ij}_{\Lambda\Lambda'}(\boldsymbol{k}, E) e^{-i\boldsymbol{k}\cdot\boldsymbol{R}_J} \ . \end{aligned} \tag{4.33}$$

For the actual computation of the CPA, it is sufficient to take into account for the scattering in site i of the reference unit cell

$$\tau_{c\,\Lambda\Lambda'}^{0i0i}(E) = \sum_{\alpha} c_\alpha \tau_{\alpha\,\Lambda\Lambda'}^{0i0i}(E) \; . \tag{4.34}$$

This is the CPA condition represented by the scattering path operator. Here, $\tau_{c\,\Lambda\Lambda'}^{0i0i}(E)$ is the site-diagonal CPA scattering path operator

$$\tau_{c\,\Lambda\Lambda'}^{0i0i}(E) = \frac{1}{\Omega_{\mathrm{BZ}}} \int_{\mathrm{BZ}} \mathrm{d}\boldsymbol{k} \; \left[\left\{ \underline{\underline{t}}_{\mathrm{c}}^{-1}(E) - \underline{\underline{\mathcal{G}}}_0(\boldsymbol{k}, E) \right\}^{-1} \right]_{\Lambda\Lambda'}^{ii} \; . \tag{4.35}$$

The information on the coherent potential in a random alloy is contained in $\underline{\underline{t}}_c(E)$ which is the single-site scattering matrix for the coherent potential. For ordered systems, the CPA scattering path operator is given by a Brillouin zone integral in terms of the CPA single-site scattering matrix and so-called KKR structure constant $\underline{\underline{\mathcal{G}}}_0(\boldsymbol{k}, E)$. Here, the single underline indicates matrices with respect to the combined spin-angular momentum index Λ and the double underline indicates matrices with respect to the combined spin-angular momentum index and the atomic site. The scattering path operator $\tau_{\alpha\,\Lambda\Lambda'}^{0i0i}(E)$ is given by

$$\underline{\tau}_{\alpha}^{0i0i}(E) = \left[\underline{t}_{\alpha}^{i\,-1}(E) - \underline{t}_{c}^{i\,-1}(E) + \underline{\tau}_{c}^{0i0i}(E) \right]^{-1} \; , \tag{4.36}$$

which gives the scattering path operator for an embedded α-atom on the site i into the CPA medium.

4.4.2 Representation by the Projection Matrix

We rewrite the scattering path operator as follows:

$$\begin{aligned} \underline{\tau}_{\alpha}^{0i0i}(E) &= \left[\underline{\tau}_{\mathrm{c}}^{0i0i}(E) \left(\underline{t}_{\alpha}^{i\,-1}(E) - \underline{t}_{c}^{i\,-1}(E) \right) + 1 \right]^{-1} \underline{\tau}_{c}^{0i0i}(E) \\ &= \underline{D}_{\alpha}^{ii}(E) \underline{\tau}_{c}^{0i0i}(E) \; , \end{aligned} \tag{4.37}$$

$$\begin{aligned} \underline{\tau}_{\alpha}^{0i0i}(E) &= \underline{\tau}_{c}^{0i0i}(E) \left[\left(\underline{t}_{\alpha}^{i\,-1}(E) - \underline{t}_{c}^{i\,-1}(E) \right) \underline{\tau}_{c}^{0i0i}(E) + 1 \right]^{-1} \\ &= \underline{\tau}_{c}^{0i0i}(E) \tilde{\underline{D}}_{\alpha}^{ii}(E) \; . \end{aligned} \tag{4.38}$$

where operators

$$\underline{D}_{\alpha}^{ii}(E) = \left[\underline{\tau}_{\mathrm{c}}^{0i0i}(E) \left(\underline{t}_{\alpha}^{i\,-1}(E) - \underline{t}_{c}^{i\,-1}(E) \right) + 1 \right]^{-1} \; , \tag{4.39}$$

$$\tilde{\underline{D}}_{\alpha}^{ii}(E) = \left[\left(\underline{t}_{\alpha}^{i\,-1}(E) - \underline{t}_{c}^{i\,-1}(E) \right) \underline{\tau}_{c}^{0i0i}(E) + 1 \right]^{-1} \; , \tag{4.40}$$

are called projection matrices. Using these operators, the CPA condition is rewritten as

$$\sum_{\alpha} c_{\alpha} \underline{\tilde{D}}_{\alpha}^{ii}(E) = \sum_{\alpha} c_{\alpha} \underline{D}_{\alpha}^{ii}(E) = 1 \ . \tag{4.41}$$

4.4.3 Representation by the Excess Scattering Matrix

We further rewrite the CPA condition using excess scattering matrix. This is a necessary step to apply Mills' algorithm that is a commonly used technique for solving the CPA condition numerically in the KKR method. We rewrite the projection matrix $\underline{D}_{\alpha}^{ii}$ as follows:

$$\begin{aligned} \underline{D}_{\alpha}^{ii}(E) &= 1 + \underline{\tau}_{\mathrm{c}}^{0i0i}(E) \left[\left(\underline{t}_{c}^{i\,-1}(E) - \underline{t}_{\alpha}^{i\,-1}(E) \right)^{-1} - \underline{\tau}_{c}^{0i0i}(E) \right]^{-1} \\ &= 1 + \underline{\tau}_{c}^{0i0i}(E) \underline{X}_{\alpha}^{ii}(E) \ . \end{aligned} \tag{4.42}$$

where the operator

$$\underline{X}_{\alpha}^{ii}(E) = \left[\left(\underline{t}_{c}^{i\,-1}(E) - \underline{t}_{\alpha}^{i\,-1}(E) \right)^{-1} - \underline{\tau}_{c}^{0i0i}(E) \right]^{-1} \ , \tag{4.43}$$

is called the excess scattering matrix. Using the excess scattering matrix, the CPA condition is given by

$$\sum_{\alpha} c_{\alpha} \underline{X}_{\alpha}^{ii}(E) = 0 \ . \tag{4.44}$$

4.4.4 Mills' Method

We finally discuss the computational method of the CPA in the KKR formalism. Unlike the mentioned VCA and ATA methods, we have to determine the CPA medium self-consistently for the given t-matrices $\underline{t}_{\alpha}^{i}(E)$ of the components. Several algorithms have been suggested to deal with the above CPA equations. The most commonly used algorithm was worked out by Mills et al. [67], and allows to obtain the CPA scattering path operator $\underline{\tau}_{c}^{0i0i}(E)$ by an iterative process [68].

When the CPA condition is not satisfied by the n-th temporary t-matrix $\underline{t}_{c}^{i\,(n)}(E)$, we can define the concentration average of the n-th excess scattering operator $\underline{X}_{c}^{ii\,(n)}(E)$

as

$$\underline{X}_c^{ii(n)}(E) = \sum_\alpha c_\alpha \underline{X}_\alpha^{ii(n)}(E) \neq 0 \ , \tag{4.45}$$

where the operator $\underline{X}_\alpha^{ii(n)}(E)$ is given by

$$\underline{X}_\alpha^{ii(n)}(E) = \left[\left(\underline{t}_c^{i\,(n)^{-1}}(E) - \underline{t}_\alpha^{i\,^{-1}}(E) \right)^{-1} - \underline{\tau}_c^{0i0i(n)^{-1}}(E) \right]^{-1} \ . \tag{4.46}$$

Here, $\underline{\tau}_c^{0i0i(n)}(E)$ is the n-th temporary scattering path operator

$$\underline{\tau}_c^{0i0i(n)}(E) = \frac{1}{\Omega_{\rm BZ}} \int_{\rm BZ} {\rm d}\boldsymbol{k} \left[\left\{ \underline{t}_c^{\,(n)^{-1}}(E) - \underline{\underline{\mathcal{G}}}_0(\boldsymbol{k}, E) \right\}^{-1} \right]^{ii} \ , \tag{4.47}$$

which is given by the n-th temporary t-matrix and the structure constant $\underline{\underline{\mathcal{G}}}_0(\boldsymbol{k}, E)$. The next update of the t-matrix is obtained as follows:

$$\underline{t}_c^{i\,(n+1)^{-1}}(E) = \underline{t}_{\rm c}^{i\,(n)-1}(E) - \left[\underline{X}_c^{ii(n)^{-1}}(E) + \underline{\tau}_c^{0i0i(n)}(E) \right]^{-1} \ . \tag{4.48}$$

We repeat the cycle until $\underline{X}_\alpha^{ii(n)}(E)$ becomes smaller than a threshold δ. For the initial guess of the t-matrix, we exploit the ATA

$$\underline{t}_c^{i\,(1)}(E) = \sum_\alpha c_\alpha \underline{t}_\alpha^i(E) \ . \tag{4.49}$$

Part II

Application of the CPA on the Basis of Wannier Representation

Chapter 5

Wannier-based Implementation of the CPA Method

In this chapter, we derive a formulation of the CPA on the basis of the Wannier representation for the treatment of homogeneous random alloys. This new method is computationally efficient compared to the existing calculation method and independent on the applied first-principles electronic structure code.

5.1 Wannier Functions

Wannier functions $w_n(\boldsymbol{r}-\boldsymbol{R})$ are defined by the following equation:

$$w_n(\boldsymbol{r}-\boldsymbol{R}) = \frac{\Omega_{\rm cell}}{(2\pi)^3}\int_{\rm BZ} {\rm d}\boldsymbol{k} e^{-i\boldsymbol{k}\cdot\boldsymbol{R}}\tilde{\psi}_{n\boldsymbol{k}}(\boldsymbol{r}) \ , \tag{5.1}$$

Here, $\Omega_{\rm cell}$ is the volume of the unit cell and $\tilde{\psi}_{n\boldsymbol{k}}(\boldsymbol{r})$ is the unitary rotation of the Bloch functions

$$\tilde{\psi}_{n\boldsymbol{k}}(\boldsymbol{r}) = \sum_q U^{(\boldsymbol{k})}_{qn}\psi_{q\boldsymbol{k}}(\boldsymbol{r}) \ , \tag{5.2}$$

where the operator $U^{(\boldsymbol{k})}_{qn}$ is the unitary matrix. The unitary matrix $U^{(\boldsymbol{k})}_{qn}$ is determined so that the spread of the Wannier functions

$$\Omega = \sum_n \left[\langle r^2\rangle_n - \bar{\boldsymbol{r}}_n^2\right] \ , \tag{5.3}$$

has a minimal value [74, 75]. Here, $\langle r^2 \rangle_n$ and $\bar{\boldsymbol{r}}_n$ are given by

$$\langle r^2 \rangle_n = -\frac{\Omega_{\rm cell}}{(2\pi)^3} \int_{\rm BZ} {\rm d}\boldsymbol{k} \int_{\rm cell} {\rm d}\boldsymbol{r} \tilde{u}^*_{m\boldsymbol{k}}(\boldsymbol{r}) \nabla^2_{\boldsymbol{k}} \tilde{u}_{n\boldsymbol{k}}(\boldsymbol{r}) \ , \tag{5.4}$$

$$\bar{\boldsymbol{r}}_n = \frac{\Omega_{\rm cell}}{(2\pi)^3} \int_{\rm BZ} {\rm d}\boldsymbol{k} \int_{\rm cell} {\rm d}\boldsymbol{r} \tilde{u}^*_{m\boldsymbol{k}}(\boldsymbol{r}) (i\nabla_{\boldsymbol{k}}) \tilde{u}_{n\boldsymbol{k}}(\boldsymbol{r}) \ . \tag{5.5}$$

Therefore, n is not the band index in the usual sense. Since the Bloch function is normalized to one unit cell, it obeys the following orthogonalization condition by integrating over the whole space

$$\int_{\rm all} {\rm d}\boldsymbol{r} \psi^*_{n\boldsymbol{k}}(\boldsymbol{r}) \psi_{m\boldsymbol{k}'}(\boldsymbol{r}) = \frac{(2\pi)^3}{\Omega_{\rm cell}} \delta_{nm} \delta^3(\boldsymbol{k} - \boldsymbol{k}') \ . \tag{5.6}$$

On the other hand, Wannier functions are normalized to the whole space

$$\int_{\rm all} {\rm d}\boldsymbol{r} w^*_n(\boldsymbol{r} - \boldsymbol{R}) w_m(\boldsymbol{r} - \boldsymbol{R}') = \delta_{nm} \delta^3_{\boldsymbol{R}\boldsymbol{R}'} \ . \tag{5.7}$$

The expected values of the Hamiltonian in terms of the Wannier functions are obtained from that of the Bloch functions

$$\int_{\rm all} {\rm d}\boldsymbol{r} w^*_n(\boldsymbol{r}) \hat{H}(\boldsymbol{r}) w_m(\boldsymbol{r} - \boldsymbol{R}) = \frac{\Omega_{\rm cell}}{(2\pi)^3} \int_{\rm BZ} {\rm d}\boldsymbol{k} e^{-i\boldsymbol{k}\cdot\boldsymbol{R}} \int_{\rm cell} {\rm d}\boldsymbol{r} \tilde{\psi}^*_{n\boldsymbol{k}}(\boldsymbol{r}) \hat{H}(\boldsymbol{r}) \tilde{\psi}_{m\boldsymbol{k}}(\boldsymbol{r}) \ , \tag{5.8}$$

and vice versa

$$\int_{\rm cell} {\rm d}\boldsymbol{r} \tilde{\psi}^*_{n\boldsymbol{k}}(\boldsymbol{r}) \hat{H}(\boldsymbol{r}) \tilde{\psi}_{m\boldsymbol{k}}(\boldsymbol{r}) = \sum_{\boldsymbol{R}} e^{i\boldsymbol{k}\cdot\boldsymbol{R}} \int_{\rm all} {\rm d}\boldsymbol{r} w^*_n(\boldsymbol{r}) \hat{H}(\boldsymbol{r}) w_m(\boldsymbol{r} - \boldsymbol{R}) \ . \tag{5.9}$$

5.2 Wannier TB Hamiltonian

While the Green's function is directly supplied by the KKR-CPA method, we first have to construct a TB Hamiltonian in case of the Wannier formalism according to the expression:

$$\hat{H} = \sum_{I,J} \sum_{i,j} \sum_{n,n'} |\boldsymbol{R}_I + \boldsymbol{Q}_i, n\rangle \, H^{IiJj}_{nn'} \, \langle \boldsymbol{R}_J + \boldsymbol{Q}_j, n'| \ , \tag{5.10}$$

where n is the index of the Wannier functions including spin. To make use of the CPA, we divide the Hamiltonian into site diagonal and off-diagonal terms as in CPA, in which a single-site theory is formulated only for diagonal terms:

$$H^{IiJj}_{nn'} = (1 - \delta_{IJ}\delta_{ij}) t^{IiJj}_{nn'} + \delta_{IJ}\delta_{ij} v^i_{nn'} \ , \tag{5.11}$$

where v and t are the on-site potential and the site off-diagonal terms of the Hamiltonian of the Wannier basis, respectively.

5.3 Green's Function

To apply the CPA to the Wannier functions, we construct the Green's function of the system from the TB Hamiltonian. We represent the Green's function in the same basis as the Wannier TB Hamiltonian

$$G(E) = \sum_{I,i} \sum_{J,j} \sum_{n,n'} |\boldsymbol{R}_I + \boldsymbol{Q}_i, n\rangle \, G^{IiJj}_{nn'}(E) \, \langle \boldsymbol{R}_J + \boldsymbol{Q}_j, n'| \ . \tag{5.12}$$

Since the Green's function is written formally as $[E - \mathcal{H}]G(E) = 1$, we can obtain the matrix components of the Green's function as

$$\underline{G}^{IiJj}(E) = (E - \underline{v}^i)^{-1}\delta_{IJ}\delta_{ij} + (E - \underline{v}^i)^{-1} \sum_{Ss} (1 - \delta_{IS}\delta_{is}) \underline{t}^{IiSs} \underline{G}^{SsJj}(E) \tag{5.13}$$

By defining the matrices

$$\left[\underline{\underline{G}}(E)\right]^{IiJj}_{nn'} = G^{IiJj}_{nn'}(E) \ , \tag{5.14}$$

$$\left[\underline{\underline{G}}_0(E)\right]^{IiJj}_{nn'} = \delta_{IJ}(\delta_{ij}E - \underline{v}^i_{nn'})^{-1} \ , \tag{5.15}$$

$$\left[\underline{\underline{t}}(E)\right]^{IiJj}_{nn'} = (1 - \delta_{IJ}\delta_{ij}) t^{IiJj}_{nn'} \ , \tag{5.16}$$

we can rewrite the equation above in matrix form

$$\underline{\underline{G}}(E) = \left[\underline{\underline{G}}_0^{-1}(E) - \underline{\underline{t}}(E)\right]^{-1} \ , \tag{5.17}$$

where matrices with both atomic site and the Wannier function indices are indicated by a double-underline. The Green's function of the system is given by this equation. However, from the point of view of the numerical calculation, it is not preferable to directly use the equation since we have to calculate the inverse of a large matrix. In stead, we exploit the Fourier transform of the above Green's function

$$\mathcal{G}^{ij}_{nn'}(\boldsymbol{k}, E) = \sum_J G^{0iJj}_{nn'}(E) e^{i\boldsymbol{k}\cdot\boldsymbol{R}_J} \ . \tag{5.18}$$

Using the Fourier transform $\mathcal{G}^{ij}_{nn'}(\boldsymbol{k}, E)$ we can reduce the number of components

$$\underline{\underline{\mathcal{G}}}(\boldsymbol{k}, E) = \left[\underline{\underline{\mathcal{G}}}_0^{-1}(E) - \underline{\underline{\mathcal{T}}}(\boldsymbol{k})\right]^{-1} \tag{5.19}$$

where each elements of the matrices is given by

$$\left[\underline{\underline{\mathcal{G}}}(\boldsymbol{k},E)\right]^{ij}_{nn'} = \mathcal{G}^{ij}_{nn'}(\boldsymbol{k},E)\ , \tag{5.20}$$

$$\left[\underline{\underline{\mathcal{G}}}_0^{-1}(E)\right]^{ij}_{nn'} = \delta_{ij}(\delta_{nn'}E - v^i_{nn'})\ , \tag{5.21}$$

$$\left[\underline{\underline{\mathcal{T}}}(\boldsymbol{k})\right]^{ij}_{nn'} = \sum_J (1-\delta_{0J}\delta_{ij}) t^{0iJj}_{nn'} e^{i\boldsymbol{k}\cdot\boldsymbol{R}_J}\ . \tag{5.22}$$

5.4 CPA in Wannier Formalism

The KKR multiple scattering formulation for the CPA condition cannot be used within the Wannier formalism. This is because of the complexity in defining the scattering path operator in the TB model. Therefore, we used an equation mathematically equivalent to the equation in the KKR-CPA condition [see Eq. (4.34)]. For this purpose, we exploit the representation of the scattering operator $\underline{t}^i_\alpha(E)$ in Eq. (4.25).

For the numerical calculation of the coherent potential, $\underline{v}^i_c(E)$, we use an iterative method that is similar to the Mills' algorithm. We update the n-th temporary coherent potential $\underline{v}_c^{i\,(n)}(E)$ in the following way. When the CPA condition is not satisfied by the n-th temporary coherent potential, we can define the concentration averaged scattering operator as

$$\langle \underline{t}^i \rangle^{(n)} = \sum_\alpha c_\alpha \underline{t}_\alpha^{i\ (n)} \neq 0\ . \tag{5.23}$$

The next update for the coherent potential is obtained as follows:

$$\underline{v}_c^{i\,(n+1)}(E) = \underline{v}_c^{i\,(n)}(E) + \langle \underline{t}^i \rangle^{(n)} \left(1 + \underline{G}_c^{0i0i\,(n)}(E)\, \langle \underline{t}^i \rangle^{(n)}\right)^{-1}\ , \tag{5.24}$$

where the Green's function is obtained from the n-th coherent potential $\underline{v}_c^{i\,(n)}(E)$. We repeat the cycle until $\langle \underline{t}_i \rangle^{(n)}$ becomes smaller than a threshold δ. We exploit the VCA for the initial guess of the coherent potential as follows:

$$\underline{v}_c^{i\,(1)}(E) = \sum_\alpha c_\alpha \underline{v}^i_\alpha\ . \tag{5.25}$$

To apply this formalism to real alloys, we have to consider the following two points. One is the on-site potentials of the two pure components, since the DFT-based Wannier Hamiltonian does not give information on the reference value of these potentials. To

determine the relative on-site potential energies, we use the supercell calculations as follows. Let us consider an A-B binary alloy. First, we perform DFT calculations for a supercell of eight-atoms, A_1B_7 and A_7B_1, and construct the TB Hamiltonian in the Wannier basis. Then, we derive the difference of the on-site potential of the $3d$ orbitals between component A and B in both A_1B_7 and A_7B_1, and set its average as $\Delta v_{A-B}^{\rm supercell}$. Then, we perform DFT calculations for pure A and pure B, and construct the Wannier TB Hamiltonian. We use this Hamiltonian for the calculation of the CPA Green's function, but before starting the CPA calculation, we subtract a constant from the diagonal terms of the on-site potential so that the potential difference of $3d$ orbitals in pure A and pure B becomes $\Delta v_{A-B}^{\rm supercell}$.

The other point to consider is the determination of the site off-diagonal term in the TB Hamiltonian since the site diagonal terms as well as the site off-diagonal terms are different for the two components. This is in sharp contrast to the KKR-CPA formalism, where only the scattering path operator depends on the component. In this paper, since we consider the alloys consisting of two transition metal elements, we simply take a concentration average [19, 41].

The accurate determination of the Fermi energy is important for examining the magnetic properties of alloys. We set the Fermi energy so that the total number of electrons

$$N = -\frac{1}{\pi}{\rm Im}{\rm Tr}\int^{E_{\rm F}} {\rm d}E\underline{\underline{G}}_c(E)\ , \tag{5.26}$$

is consistent with the number of electrons in the A-B alloy. A complex contour Gauss-Legendre integral is used to calculate the above integral. The Fermi energy of the system is determined iteratively using the DOS and the difference between the total number of electrons of the alloy and the number of electrons obtained by integrating the Green's function up to the temporary Fermi energy. We present the schematic illustration in Appendix A.

Chapter 6

Application of the Wannier-CPA Method to Fe-based Transition-metal Alloys

In this chapter, we exploit the formulation of the CPA on the basis of the Wannier representation we developed in the previous chapter. This new method is computationally efficient compared to the existing calculation method and independent on the applied first-principles electric structure code. To verify the performance of this CPA implementation within the Wannier representation we have examined the Bloch spectral function, the density of states (DOS), and the magnetic moment in Fe-based transition-metal alloys Fe-X (X = V, Co, Ni, and Cu) as well as the spin-resolved Bloch spectral function and the element specific properties of the DOS, and compared the results with those of the well-established CPA implementation based on the KKR Green's function method.

Here, we only discuss the Bloch spectral function, the DOS, and the magnetic moment. However, this new approach can be a significant step toward the other physical quantities such as the extrinsic contribution of the anomalous and spin Hall effect that cannot be handled by the conventional Wannier representation. Furthermore, the Wannier-CPA method has potential applicability to large compound systems because of its low computational effort required.

6.1 Computational Steps of a Wannier-CPA Calculation

The CPA calculations using the Wannier formalism have been organized as follows: First, we performed DFT calculations using the QUANTUM ESPRESSO package [69, 70] based on plane waves and pseudopotentials. We use the ultrasoft pseudopotentials [71] in the PSlibrary [72] with the functional type of GGA-PBE exchange-correlation functional [73] and with relativistic effects included. Here, we set the lattice constant as the experimental value of bcc Fe $a = 2.86$ Å assuming that bcc Fe is alloyed with other transition-metal elements.

The wannierization process is conducted by using WANNIER90 package [74, 75, 76, 77, 78] to reproduce the DFT energy bands below $E_{\mathrm{F}} + 3$ eV, with E_{F} being the Fermi energy. We construct for each spin a nine-orbital model, which contains one 4s, five 3d, and three 4p atomic orbitals.

The electric structure calculation of KKR-CPA method is performed self-consistently by the fully relativistic spin-polarized Munich SPR-KKR package [79, 80]. For the exchange-correlation functional, the parametrization given by Vosko *et al.* [81] has been used. An angular momentum cutoff of $l_{\max} = 4$ was used for the KKR multiple-scattering calculations. Here, we used the same lattice parameter $a = 2.86$ Å as in the Wannier-CPA calculation.

As the Green's function of a random alloy is obtained by the process described above, we can calculate the Bloch spectral function, the DOS, and the magnetic moment from the obtained CPA Green's function. In the following section, we describe results of calculations of these quantities in transition-metal alloys and compare them with the results obtained by the KKR-CPA method.

6.2 Reference of the On-site Potential

Since the relative values of the reference for the on-site potential is not given by the Wannier Hamiltonian, we have to somehow determine the difference of the on-site potential between Fe and X (X = V, Co, Ni, and Cu) components before we perform the CPA calculations. In Sec. 5.4 we devised a way to use supercell calculations. We

Table 6.1: $\Delta v_{\mathrm{Fe-V}}^{\mathrm{supercell}}$ and its difference in Fe-V supercell

Orbitals	$\Delta v_{\mathrm{Fe-V}}^{\mathrm{supercell}}$ (Fe_1V_7) [eV]	$\Delta v_{\mathrm{Fe-V}}^{\mathrm{supercell}}$ (Fe_7V_1) [eV]	Difference [eV]
all 3d (nonmag)	-2.163	-1.339	-0.824
d_{z^2} (nonmag)	-2.141	-1.309	-0.832
all 3d (mag)	-2.162	-1.363	-0.799
d_{z^2} (mag)	-2.140	-1.295	-0.845

Table 6.2: $\Delta v_{\mathrm{Fe-Co}}^{\mathrm{supercell}}$ and its difference in Fe-Co supercell

Orbitals	$\Delta v_{\mathrm{Fe-Co}}^{\mathrm{supercell}}$ (Fe_1Co_7) [eV]	$\Delta v_{\mathrm{Fe-Co}}^{\mathrm{supercell}}$ (Fe_7Co_1) [eV]	Difference [eV]
all 3d (nonmag)	-0.770	-0.836	0.065
d_{z^2} (nonmag)	0.628	0.709	0.080
all 3d (mag)	1.557	1.379	0.179
d_{z^2} (mag)	1.429	1.270	-0.159

Table 6.3: $\Delta v_{\mathrm{Fe-Ni}}^{\mathrm{supercell}}$ and its difference in Fe-Ni supercell

Orbitals	$\Delta v_{\mathrm{Fe-Ni}}^{\mathrm{supercell}}$ (Fe_1Ni_7) [eV]	$\Delta v_{\mathrm{Fe-Ni}}^{\mathrm{supercell}}$ (Fe_7Ni_1) [eV]	Difference [eV]
all 3d (nonmag)	0.855	0.915	-0.060
d_{z^2} (nonmag)	0.628	0.709	-0.080
all 3d (mag)	0.436	1.686	-1.250
d_{z^2} (mag)	0.359	1.594	-1.235

Table 6.4: $\Delta v_{\mathrm{Fe-Cu}}^{\mathrm{supercell}}$ and its difference in Fe-Cu supercell

Orbitals	$\Delta v_{\mathrm{Fe-Cu}}^{\mathrm{supercell}}$ (Fe_1Cu_7) [eV]	$\Delta v_{\mathrm{Fe-Cu}}^{\mathrm{supercell}}$ (Fe_7Cu_1) [eV]	Difference [eV]
all 3d (nonmag)	2.545	2.015	0.530
d_{z^2} (nonmag)	2.451	1.919	0.532
all 3d (mag)	2.047	2.323	0.276
d_{z^2} (mag)	2.011	2.243	-0.232

performed the calculation of $\Delta v_{\mathrm{Fe}-X}^{\mathrm{supercell}}$ (X = V, Co, Ni, and Cu) using 3d orbitals and d_{z^2} orbitals in Fe_1X_7 and Fe_7X_1 supercell. The obtained results are summarized in Tables 6.1-6.4. According to these tables, we found that the differences in $\Delta v_{\mathrm{Fe}-X}^{\mathrm{supercell}}$ calculated by using Fe_1X_7 and Fe_7X_1 are relatively small when we exploit the average of all 3d orbitals in nonmagnetic mode. Therefore, we exploit this method for the CPA calculations. We will discuss the dependence of the results on the constants subtracted from the on-site potential of X in magnetic moment in the last part of the discussion of magnetic moments.

6.3 Bloch Spectral Function

First, we show results for the Bloch spectral function of bcc Fe-X (X = V, Co, Ni, and Cu) alloys calculated by both the Wannier-CPA and the KKR-CPA methods to compare the basic electric structure that determines all physical quantities. The Bloch spectral function is the imaginary part of the trace of the Green's function given as follows:

$$A(\boldsymbol{k}, E) = -\frac{1}{\pi}\mathrm{Im\ Tr}\ \underline{\underline{\mathcal{G}}}_c(\boldsymbol{k}, E)\ . \tag{6.1}$$

If we plot the wave vector and energy region where the Bloch spectral function takes finite values, it shows a structure very similar to the band structure or dispersion relation $E(\boldsymbol{k})$ of the pure systems. Figures 6.1, 6.2, 6.3, and 6.4 shows the Bloch spectral function for bcc Fe_xV_{1-x}, Fe_xCo_{1-x}, Fe_xNi_{1-x}, and Fe_xCu_{1-x} (x = 0.0, 0.2, 0.4, 0.6, 0.8, and 1.0) alloys, respectively, calculated by both the Wannier-CPA (left side) and the KKR-CPA (right side) methods. The calculations were performed by using the bcc structure for all the calculations on Fe-X alloys for simplicity, although Co takes hexagonal structure, and Ni and Cu take fcc structure in the pure form. For the calculation for pure Fe and X components, we added a small imaginary part of 0.1 mRy to the energy to obtain visible Bloch spectra because the spectral structure consists of a delta function for pure Fe and X components. As shown in Figs. 6.1, 6.2, 6.3, and 6.4, we obtain very close spectral structures from the Wannier-CPA and the KKR-CPA methods, but we can see some small differences in the detailed structure. In the case of the Wannier-CPA method, spectra near -4 eV split for $Fe_{0.20}V_{0.80}$ as

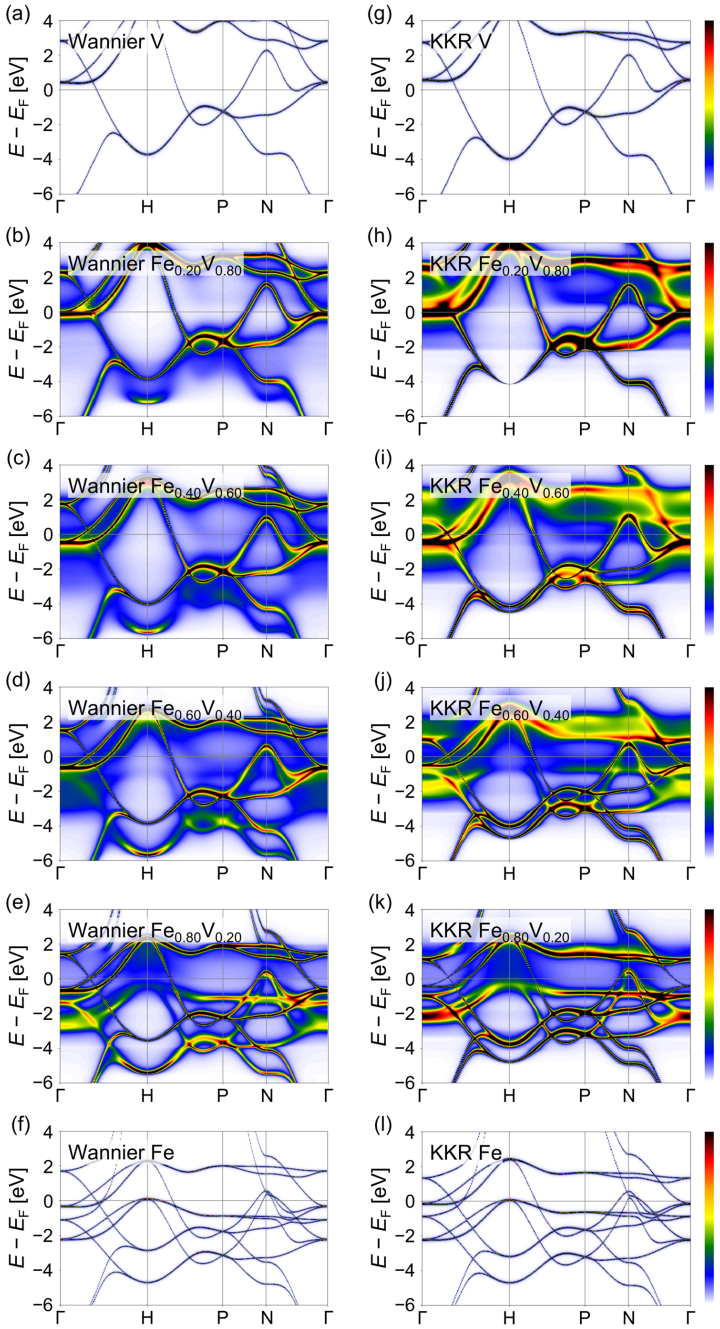

Figure 6.1: Bloch spectral functions along the high symmetry lines Γ-H-P-N-Γ for Fe_xV_{1-x} with the concentrations (a) $x = 0.00$, (b) $x = 0.20$, (c) $x = 0.40$, (d) $x = 0.60$, (e) $x = 0.80$, (f) $x = 1.00$ calculated by the Wannier-CPA method, and (g) $x = 0.00$, (h) $x = 0.20$, (i) $x = 0.40$, (j) $x = 0.60$, (k) $x = 0.80$, (l) $x = 1.00$ calculated by the KKR-CPA method.

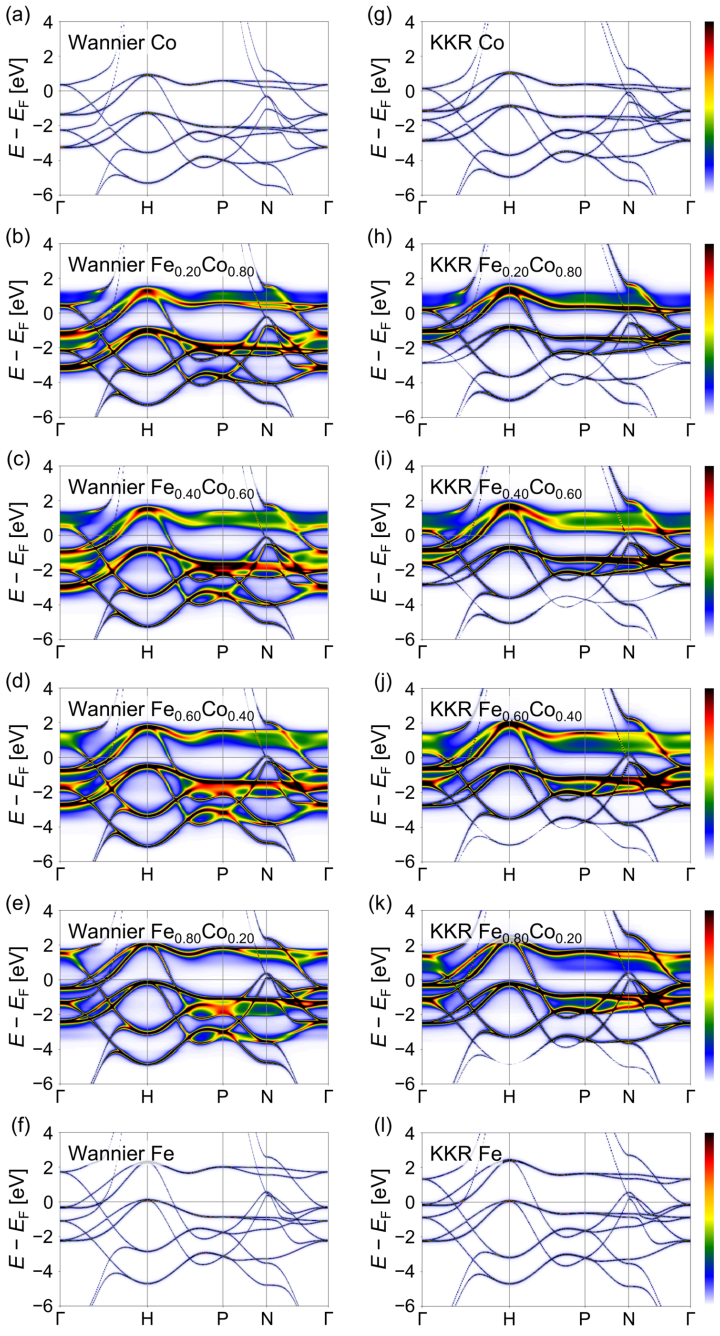

Figure 6.2: As for Fig. 6.1 but for Fe-Co alloys.

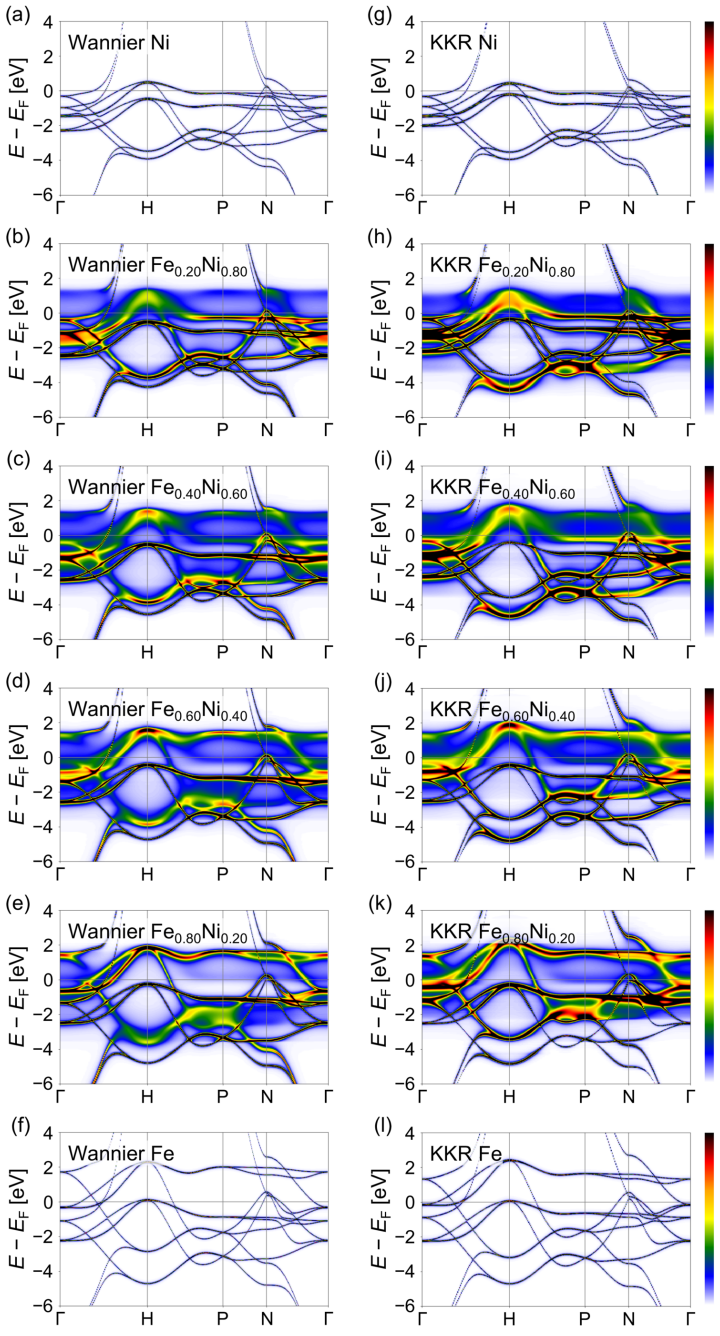

Figure 6.3: As for Fig. 6.1 but for Fe-Ni alloys.

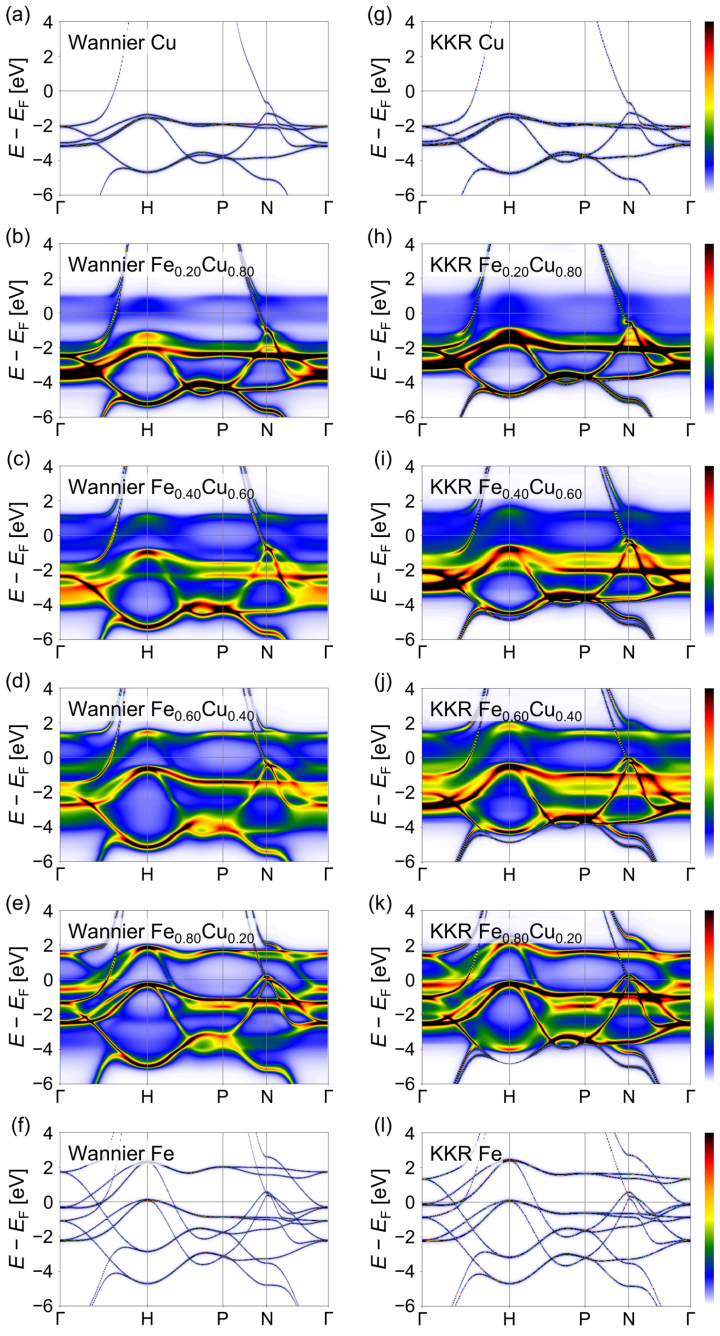

Figure 6.4: As for Fig. 6.1 but for Fe-Cu alloys.

shown in Fig. 6.1(b), which was not observed in the results of the KKR-CPA method [Fig. 6.1(h)]. For $Fe_{0.40}V_{0.60}$, the gap of the spectra is rather smaller in the KKR-CPA calculations compered with the Wannier-CPA method [see Figs. 6.1(c) and 6.1(i)]. In the KKR method, the CPA is performed within the SCF cycle, but in the Wannier-CPA method, the CPA is performed independently of the SCF process. Therefore, the magnetic moment originated from Fe remains in the V-rich region for the Wannier-CPA method. We expect that the gap of the spectral structures in the Wannier-CPA method was caused due to this residual magnetic moment of Fe.

Since the Bloch spectral functions of the total state have a rather complex structure, we resolved them with respect to the spin directions. The corresponding Bloch spectral functions for the spin-down states in Fe-X (X = V, Co, Ni, Cu) are represented in Figs. 6.5, 6.6, 6.7 and 6.8, respectively. We also show the Bloch spectral functions for the spin-up states in Figs. 6.9-6.12.

Concerning the spin-down states, we observe relatively clear spectral structures at all Fe concentrations in Fe-V, Fe-Co, Fe-Ni alloys [Figs. 6.5, 6.6, and 6.7]. The spectra gradually shifts from the structure of X to that of Fe in these alloys as the concentration of Fe is increased. On the other hand, as the concentration is changed from Cu to $Fe_{0.20}Cu_{0.80}$, blurred spectral structure of Fe appears between -1 eV and 1 eV for Fe-Cu alloys in both the Wannier-CPA and KKR-CPA results [Figs. 6.8(b) and 6.8(h)], which is about 2 eV lower than that for the pure Fe. This spectral structure becomes clear and shifts to higher energies as the concentration of Fe is increased to 0.40 and 0.60 in both the methods.

The only major difference of the Bloch spectral function for spin-down states between the Wannier-CPA and the KKR-CPA results appears in a spectral structure of $Fe_{0.80}Cu_{0.20}$ near the H-point in the reciprocal lattice. We observed a pronounced structure near -2 eV in the case of the Wannier-CPA method as shown in Fig. 6.8(e), which is strongly affected by the spectral structure of Fe. On the other hand, in the KKR-CPA method, this feature is mixed with the spectrum of Cu at around -5 eV forming a single peak spectral structure [Fig. 6.8(k)].

For pure bcc Fe, we observed weak spectral features in the spin-down channel that reflect the main spectra of the spin-up states between -2 eV and 2 eV in the results obtained by the Wannier-CPA and the KKR-CPA methods [Figs. 6.5(f) and 6.5(l)].

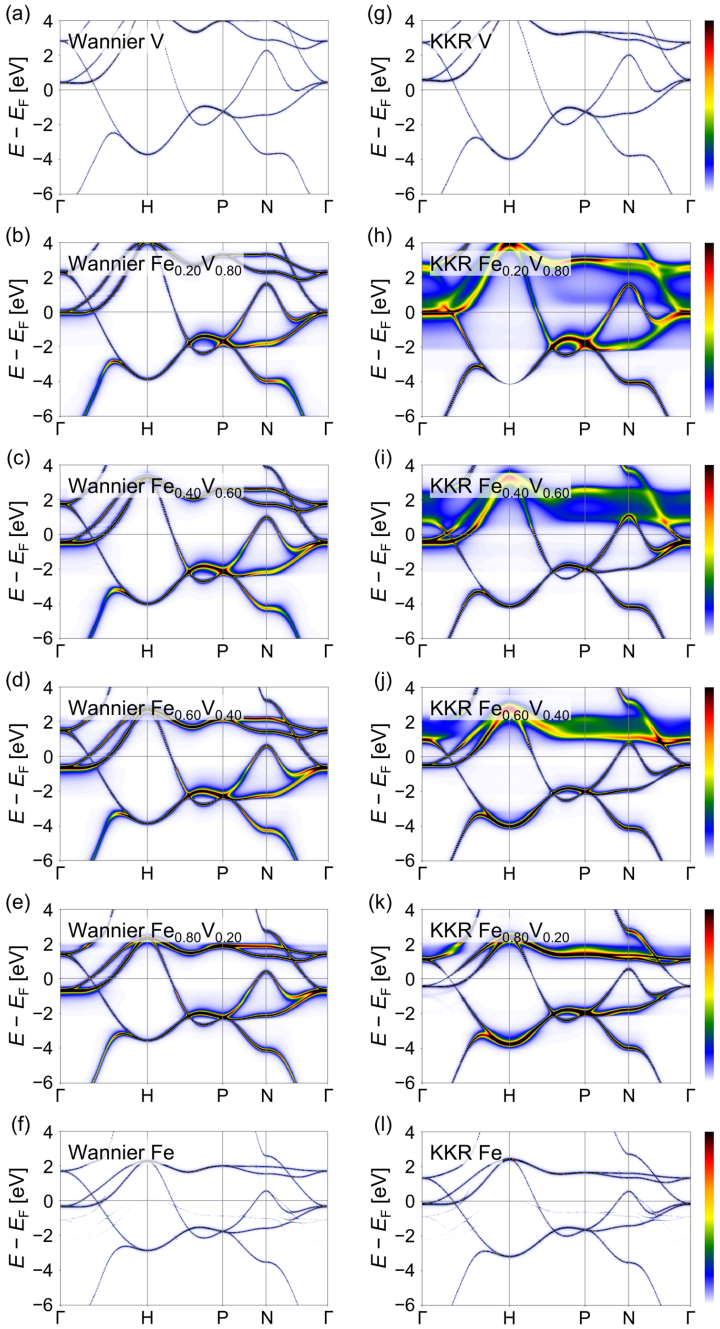

Figure 6.5: Bloch spectral functions for the spin-down states along the high symmetry lines Γ-H-P-N-Γ for Fe_xV_{1-x} with the concentrations (a) $x = 0.00$, (b) $x = 0.20$, (c) $x = 0.40$, (d) $x = 0.60$, (e) $x = 0.80$, (f) $x = 1.00$ calculated by the Wannier-CPA method, and (g) $x = 0.00$, (h) $x = 0.20$, (i) $x = 0.40$, (j) $x = 0.60$, (k) $x = 0.80$, (l) $x = 1.00$ calculated by the KKR-CPA method.

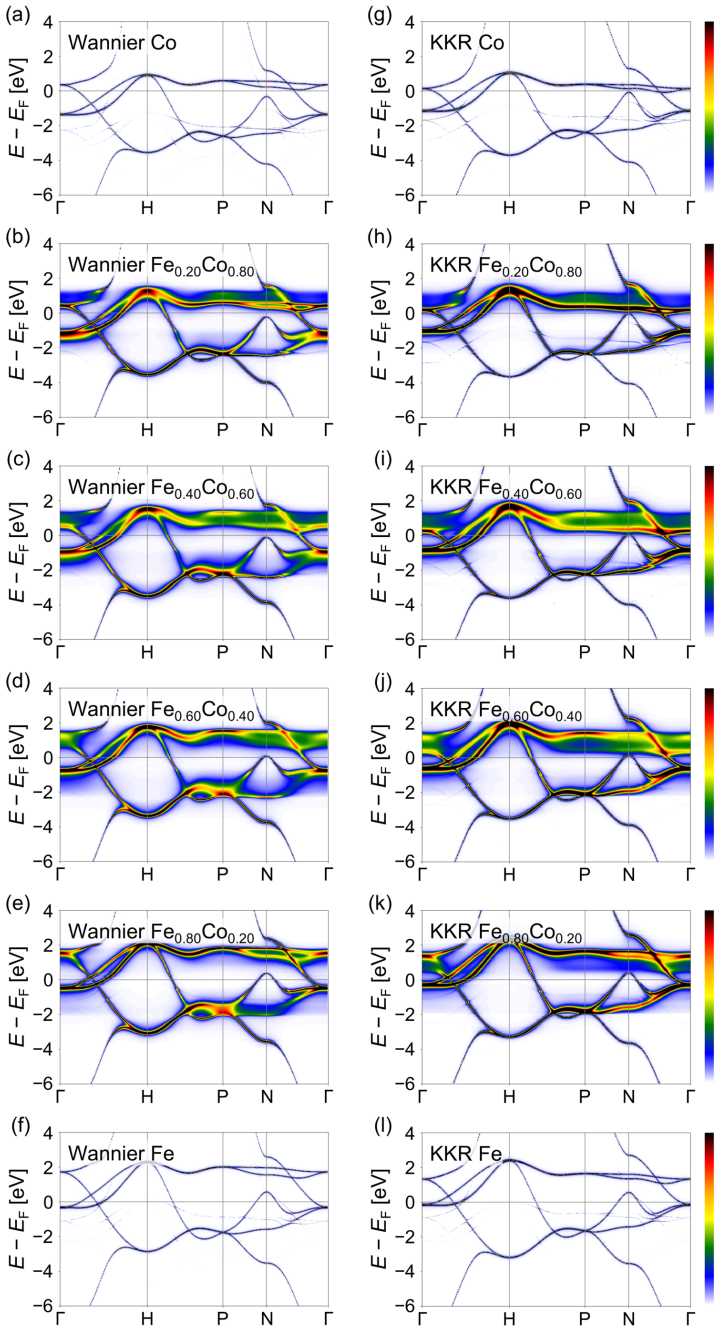

Figure 6.6: As for Fig. 6.5 but for Fe-Co alloys.

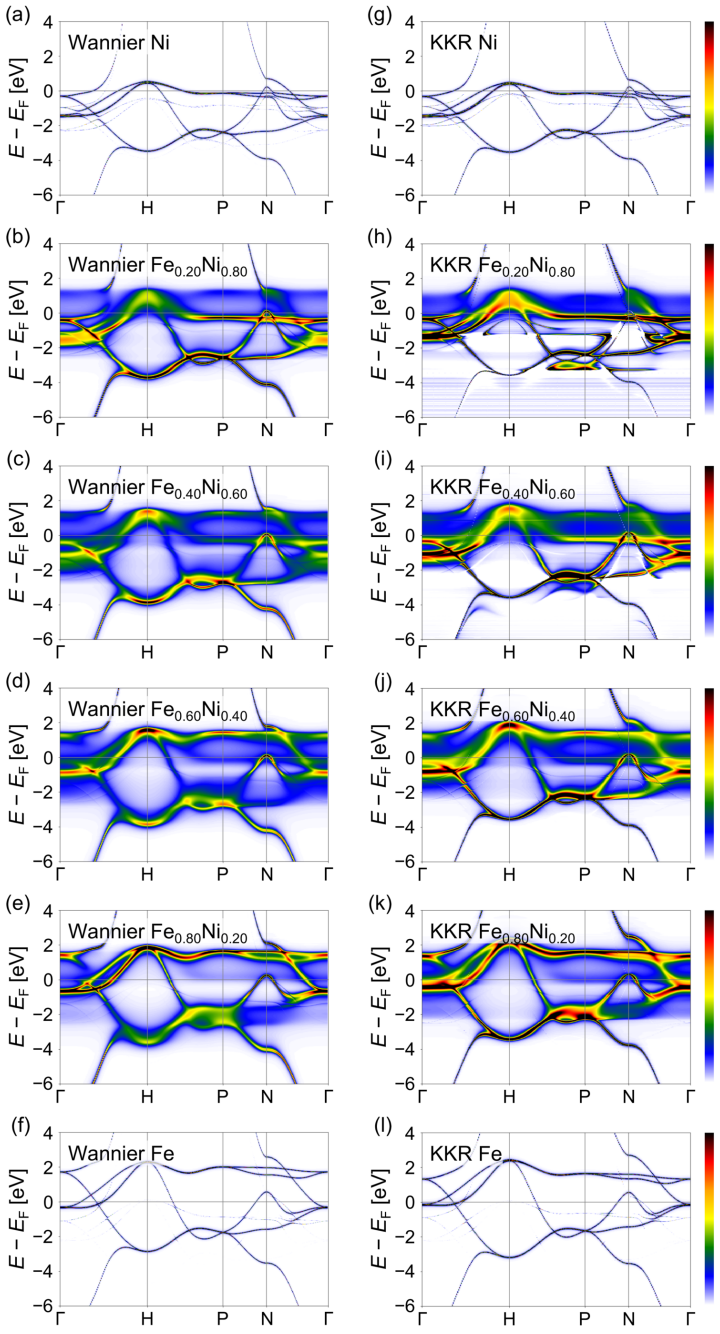

Figure 6.7: As for Fig. 6.5 but for Fe-Ni alloys.

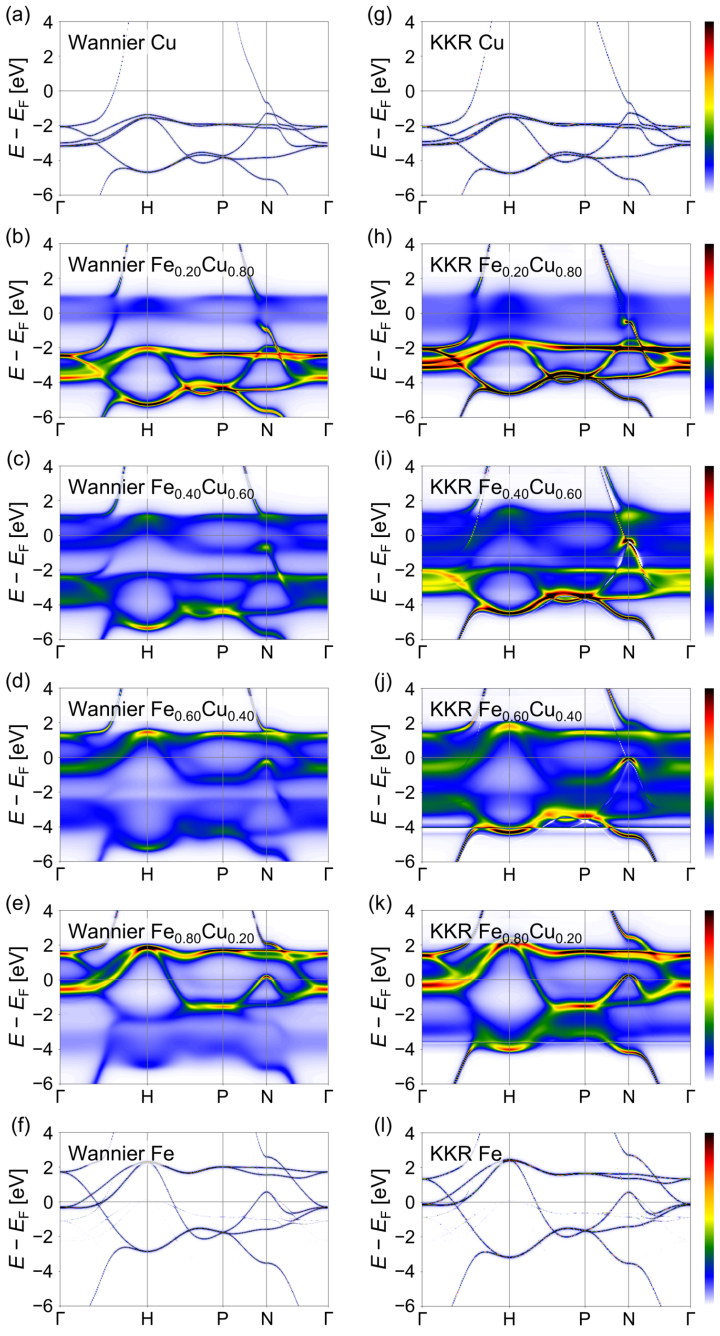

Figure 6.8: As for Fig. 6.5 but for Fe-Cu alloys.

These weak features can be ascribed to the relativistic effect of the mixing of spin-up and spin-down states by the spin-orbit coupling. This feature of the spin-orbit coupling is also observed for pure Co [Figs. 6.6(a) and 6.6(g), pure Ni [Figs. 6.7(a) and 6.7(g)], as well as some alloy systems having high Fe, Co, or Ni concentration.

Figures 6.9, 6.10, 6.11, and 6.12 shows the Bloch spectral functions for the spin-up states in Fe-X (X = V, Co, Ni, and Cu), respectively, calculated by both the Wannier-CPA and the KKR-CPA methods. Unlike the spectral structure of $Fe_{0.20}Cu_{0.80}$ in the spin-down state, the blurred spectral structure near the Fermi energy does not show up in the spin-up state as shown in Figs. 6.12(b) and 6.12(h), forming a sharper structure over the entire region. This so called virtual crystal like behavior indicates that the spin-up spectra of pure Fe and Cu are energetically closer to each other than those of the spin-down states. For the same reason, the spectral structures between -6 eV and -4 eV are less blurred compared with those between -3 eV and -1 eV in Fe_xCu_{1-x} ($x = 0.20 \sim 0.80$) alloys since the spectral structure of the pure Fe and Cr are energetically closer to each other between -6 eV and -4 eV. This behavior was observed for both the Wannier-CPA and the KKR-CPA methods [Figs. 6.12(b)-(e) and 6.12(h)-(k)]. The spectral structures of spin-up states in Fe-Co and Fe-Ni are also clearer than that of spin-down states [Figs. 6.10(b)-(e) and 6.10(h)-(k) for Fe-Co alloys, and Figs. 6.11(b)-(e) and 6.11(h)-(k) for Fe-Ni alloys] which also represents the structural similarity of the spectra of spin-up states of Co and Ni with that of Fe. However, on the other hand, the spectra of spin-up states is blurry compared with that of spin-down states for Fe-V alloys [Figs. 6.9(b)-(e) and 6.9(h)-(k)]. We again observed weak spectral feature corresponding to the main spectral structure of the spin-down states in the pure Fe between the energy of -2 eV and 1 eV [Figs. 6.9(f) and 6.9(l)] as well as pure Co, and pure Ni [Figs. 6.10(a) and 6.10(g) for Co, and Figs. 6.11(a) and 6.11(g) for Ni].

6.4 Density of States

Figure 6.13 shows the computational results for the DOS near the Fermi energy (-2 eV to 2 eV) obtained by the Wannier-CPA and the KKR-CPA methods for bcc Fe-X (X = V, Co, Ni, and Cu) alloys to monitor the occupation trend of the states in each

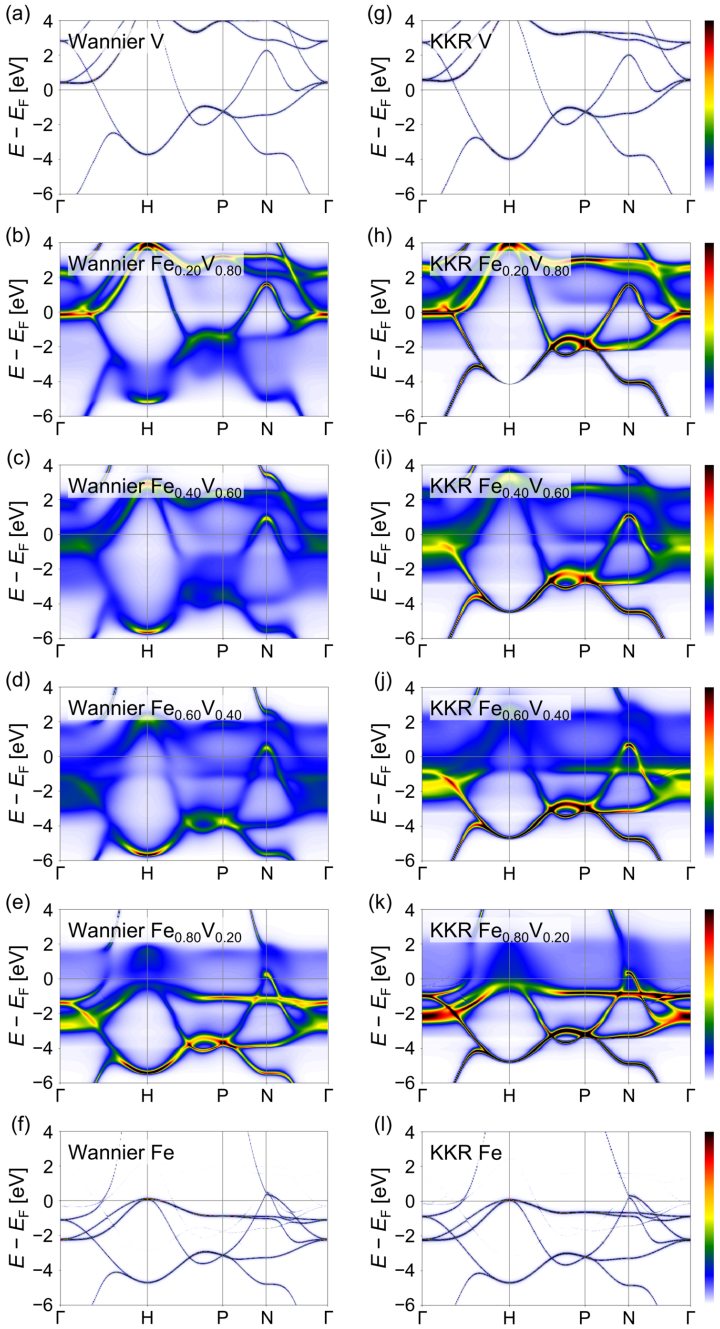

Figure 6.9: Bloch spectral functions for the spin-up states along the high symmetry lines Γ-H-P-N-Γ for Fe_xV_{1-x} with the concentrations (a) $x = 0.00$, (b) $x = 0.20$, (c) $x = 0.40$, (d) $x = 0.60$, (e) $x = 0.80$, (f) $x = 1.00$ calculated by the Wannier-CPA method, and (g) $x = 0.00$, (h) $x = 0.20$, (i) $x = 0.40$, (j) $x = 0.60$, (k) $x = 0.80$, (l) $x = 1.00$ calculated by the KKR-CPA method.

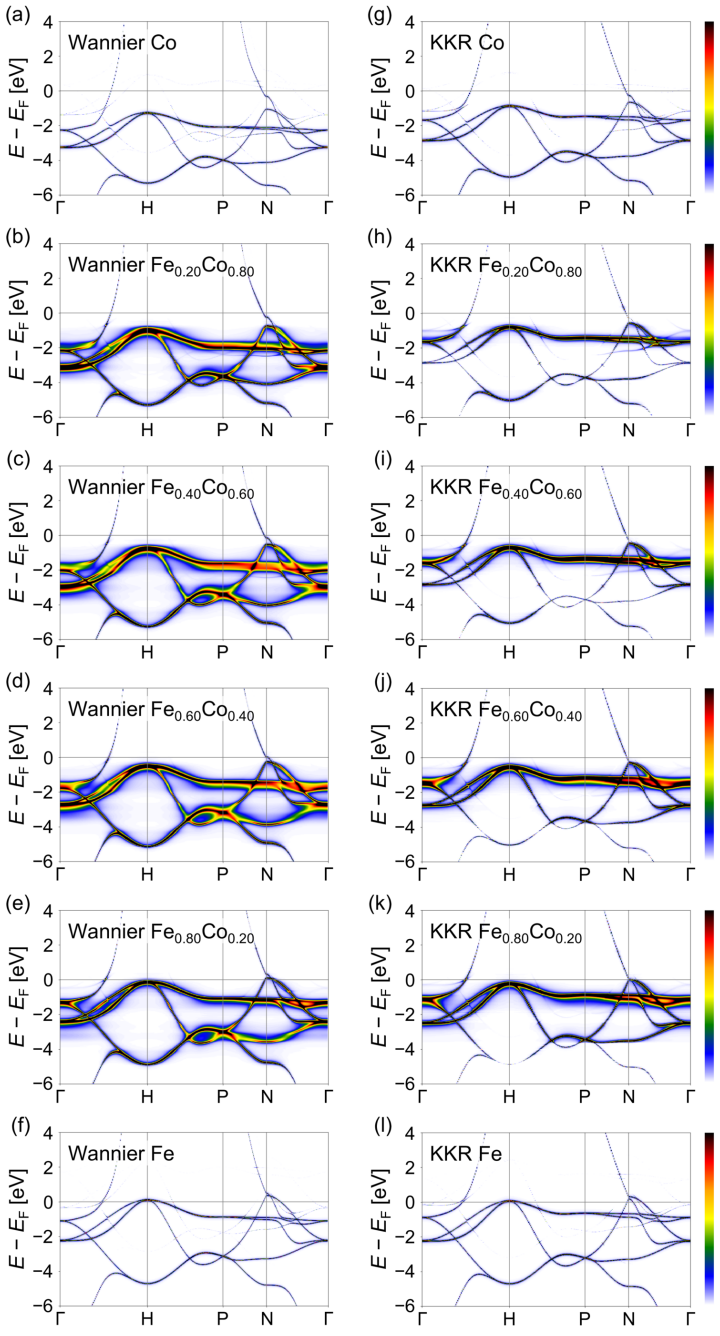

Figure 6.10: As for Fig. 6.9 but for Fe-Co alloys.

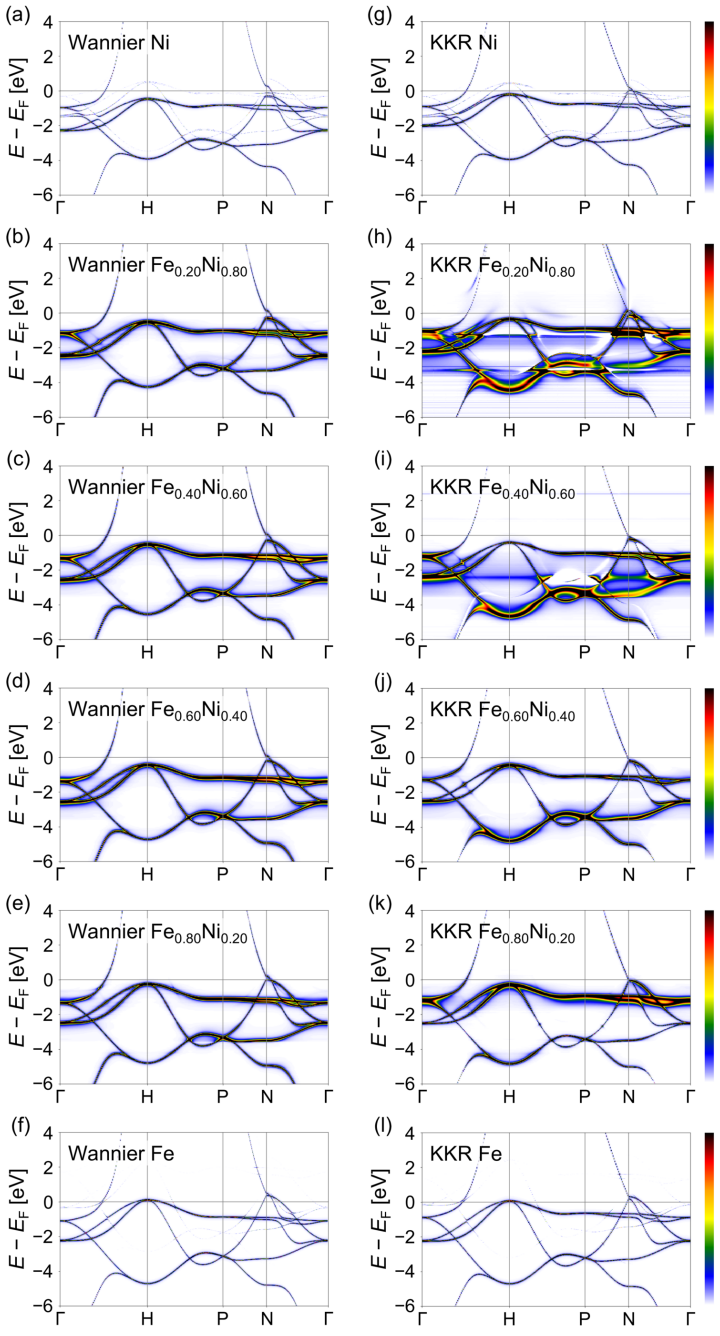

Figure 6.11: As for Fig. 6.9 but for Fe-Ni alloys.

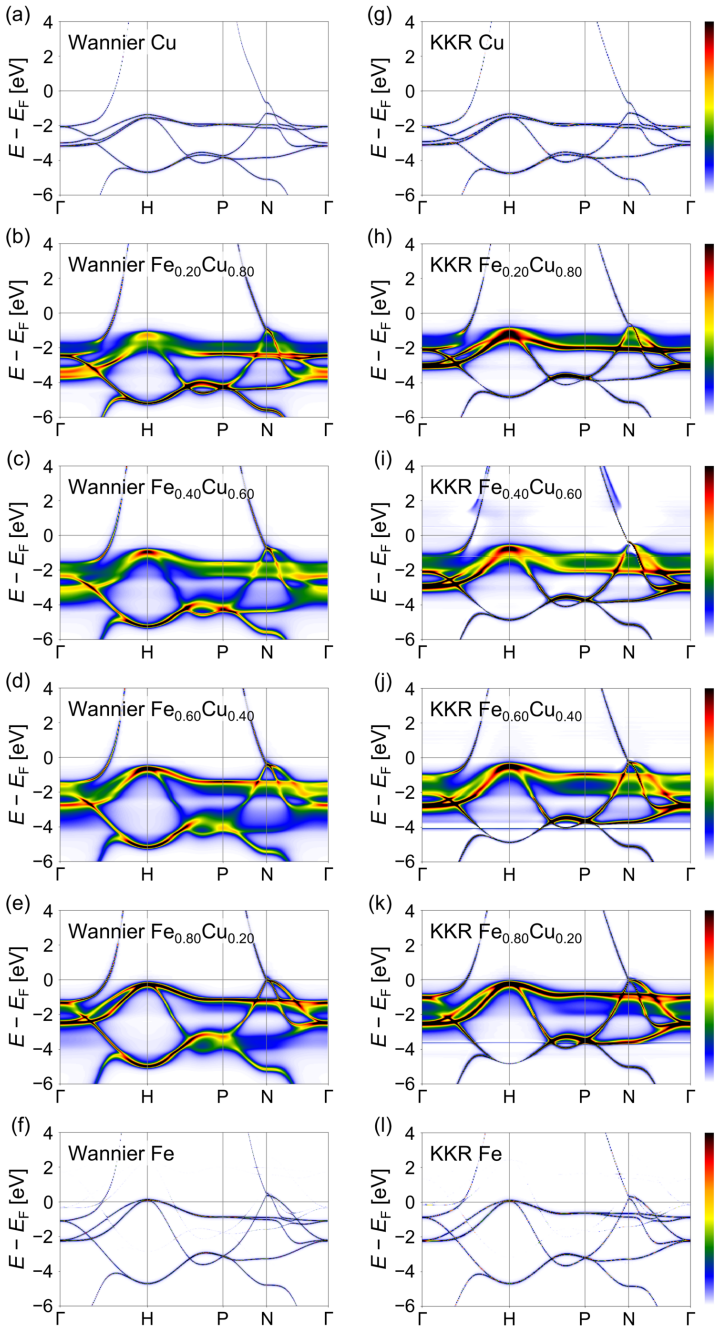

Figure 6.12: As for Fig. 6.9 but for Fe-Cu alloys.

alloy. Here, the DOS is given by integrating the Bloch spectral functions over the BZ:

$$D(E) = \int_{\mathrm{BZ}} \mathrm{d}^3k \; A(\boldsymbol{k}, E) \; . \tag{6.2}$$

or alternatively, the DOS is written using the CPA Green's function as follows:

$$D(E) = -\frac{1}{\pi} \mathrm{Im} \; \mathrm{Tr} \; \underline{\underline{G}}_c(E) \; . \tag{6.3}$$

We plotted the DOS of pure Fe and the pure X component with red and blue lines, respectively. For the alloy systems, we plotted the DOS with a neutral color between red and blue depending on the concentration of Fe and X. Figure 6.13 shows that the qualitative behavior of the DOS energy shift with increasing X concentration is fully consistent for both the Wannier-CPA and the KKR-CPA methods. A representative example can be seen in the up-DOS of Fe-Ni alloys. For the KKR-CPA method [Fig. 6.13(g)], the peak structure arising from Fe at around -1 eV is shifted to lower energies as the concentration of Ni increases, taking a minimum at around $\mathrm{Fe}_{0.50}\mathrm{Ni}_{0.50}$, and is then shifted to higher energies. This behavior is reproduced quite well by the Wannier-CPA calculations as shown in Fig. 6.13(c).

To examine the element-specific properties of the DOS, we define the component projection of the Green's function. According to the discussion in Sec. 4.4, the CPA condition can be rewritten using the Green's function as follows:

$$\underline{G}_c^{0i0i}(E) = \sum_\alpha c_\alpha \underline{G}_\alpha^{0i0i}(E) \; , \tag{6.4}$$

where $\underline{G}_\alpha^{0i0i}(E)$ is given by

$$\underline{G}_\alpha^{0i0i}(E) = \underline{G}_c^{0i0i}(E) + \underline{G}_c^{0i0i}(E) \underline{t}_\alpha^i(E) \underline{G}_c^{0i0i}(E) \; . \tag{6.5}$$

Here, $\underline{G}_\alpha^{0i0i}(E)$ gives the Green's function when for the site i of the 0-th unit cell the t-matrix of the CPA medium is replaced by that for component α. Therefore, $\underline{G}_\alpha^{0i0i}(E)$ corresponds to the α-component projection of the CPA Green's function. As the component projection of the Green's function is determined in the CPA cycle, the calculation of the element-specific properties of the DOS is straightforward. Figures 6.14 and 6.15 show the Fe and X-specific DOS of Fe-X (X = V, Co, Ni, and Cu) alloys, respectively. Here, again, the DOS of the alloy with a high Fe concentration is

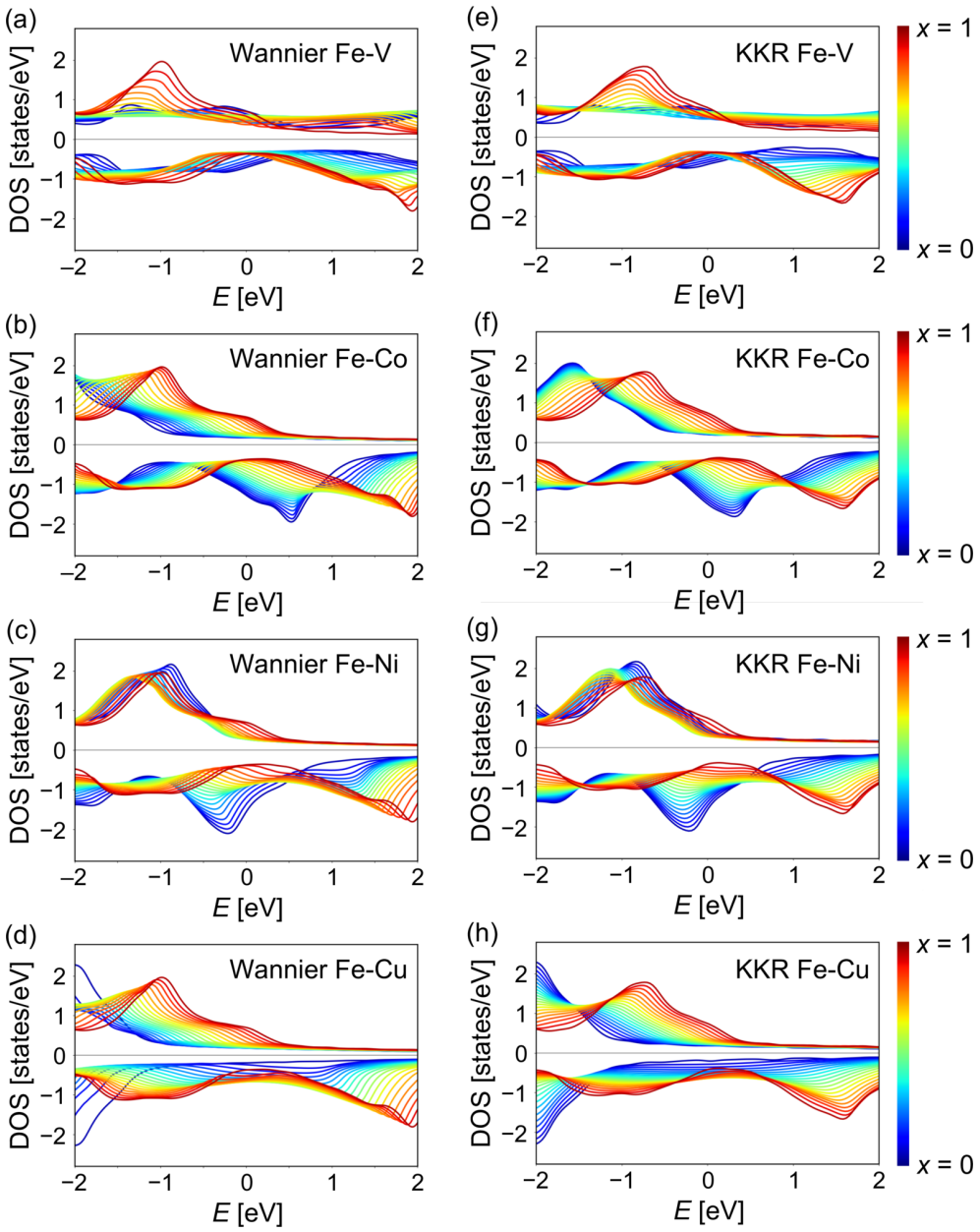

Figure 6.13: DOS of Fe_xX_{1-x} where X atoms are (a) V, (b) Co, (c) Ni, and (d) Cu alloys calculated by the Wannier-CPA method, and (e) V, (f) Co, (g) Ni, and (h) Cu alloys calculated by the KKR-CPA method. The DOS of pure Fe is given by red lines, and that of X is given by blue lines. For alloys, we give the DOS by intermediate colors between red and blue depending on the concentration of Fe and X.

plotted with reddish lines, and that with a high X concentration is given with bluish lines. On the whole, structural similarities in the element specific DOS calculated by both the Wannier-CPA and the KKR-CPA methods can be found in these figures, but we can also see some small differences in the detailed structure. For example, the Fe-component projection of the DOS of Fe-V alloys in the V-rich region obtained by KKR-CPA method has a peak structure near -1.5 eV [Fig. 6.14(e)], which are not observed in the up-DOS and quite small in the down-DOS of the Wannier-CPA calculation [Fig. 6.14(a)].

6.5 Magnetic Moment

In the previous two subsections, we found that the Wannier-CPA method can reproduce the Bloch spectral function and the DOS of Fe-based transition-metal alloys quite well. Finally, we discuss the predicted physical quantities by the Wannier-CPA method. As an example, we focused on the magnetic moment. Concerning the magnetic moment in Fe-based transition-metal alloys, one of the best benchmarks is the Slater-Pauling curve [84]. The Slater-Pauling curve is a convex curve that appears when the saturation magnetization of these alloys is plotted against the number of electrons per atom. In Fe-Co alloys, it is known that the maximum of the saturation magnetization occurs near $Fe_{0.7}Co_{0.3}$. The left and right sides of the curve form a straight line with an angle of 45 degrees with the horizontal axis of the Fe-based alloys when the scale of one electron on the horizontal axis and one Bohr magneton on the vertical axis are equal. Previous research shows that the experimental results of the Slater-Pauling curve are excellently reproduced by the KKR-CPA calculations [85, 39]. Here, we compare our results for the magnetic moment obtained by our Wannier-CPA method with those of the KKR-CPA method.

Figure 6.16 shows the magnetic moment in the Fe-X (X = V, Co, Ni, and Cu) alloys calculated by the Wannier-CPA and the KKR-CPA methods. There is a structural transition from bcc to fcc in the Fe-based alloys when the number of electrons exceeds about 26.7. However, all the calculations were done in bcc structure for the one-to-one comparison between the Wannier-CPA and the KKR-CPA methods. We can conclude from Fig. 6.16 that the Wannier-CPA calculation gives reliable calculation results con-

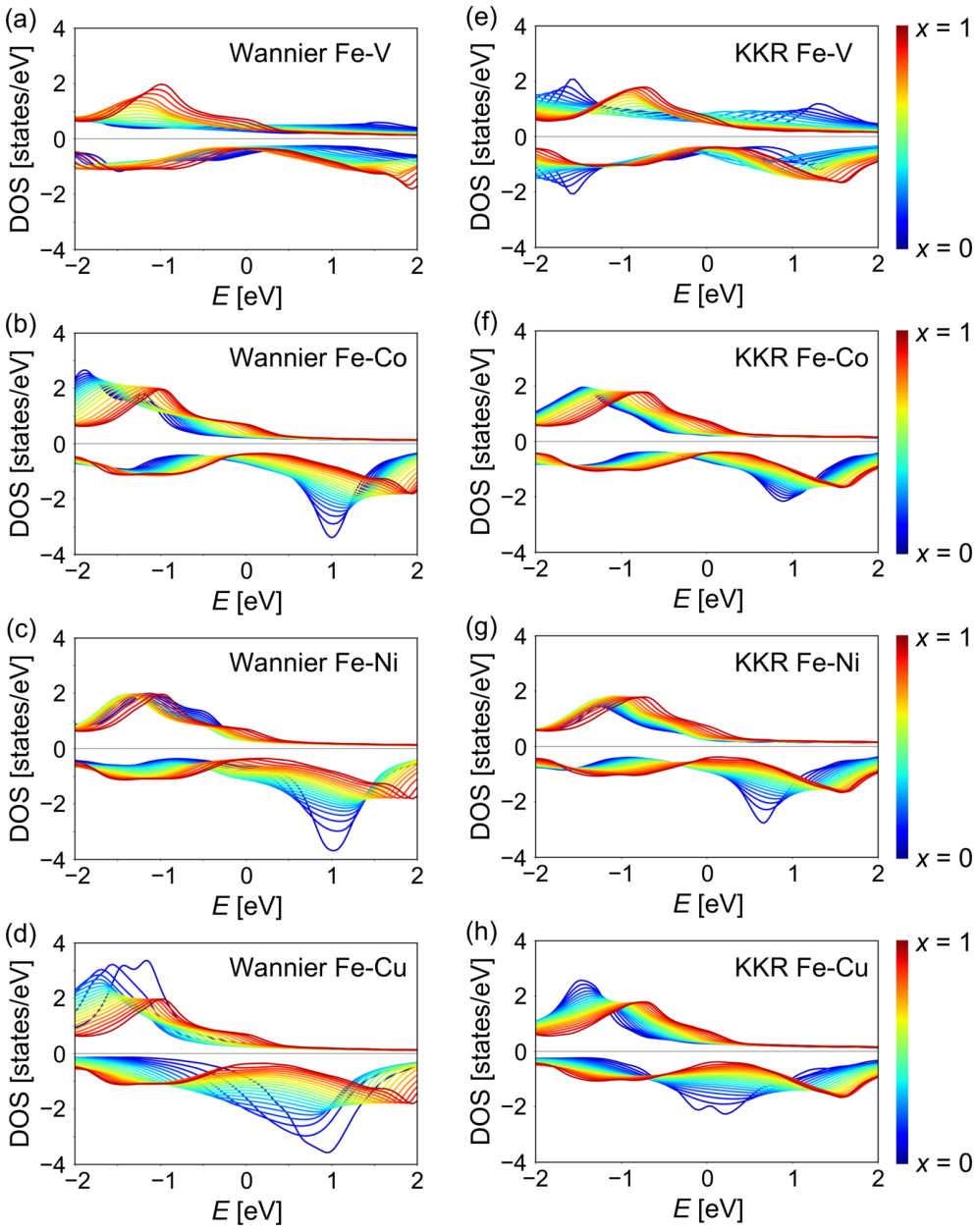

Figure 6.14: As for FIG. 6.13 but projected to Fe-component.

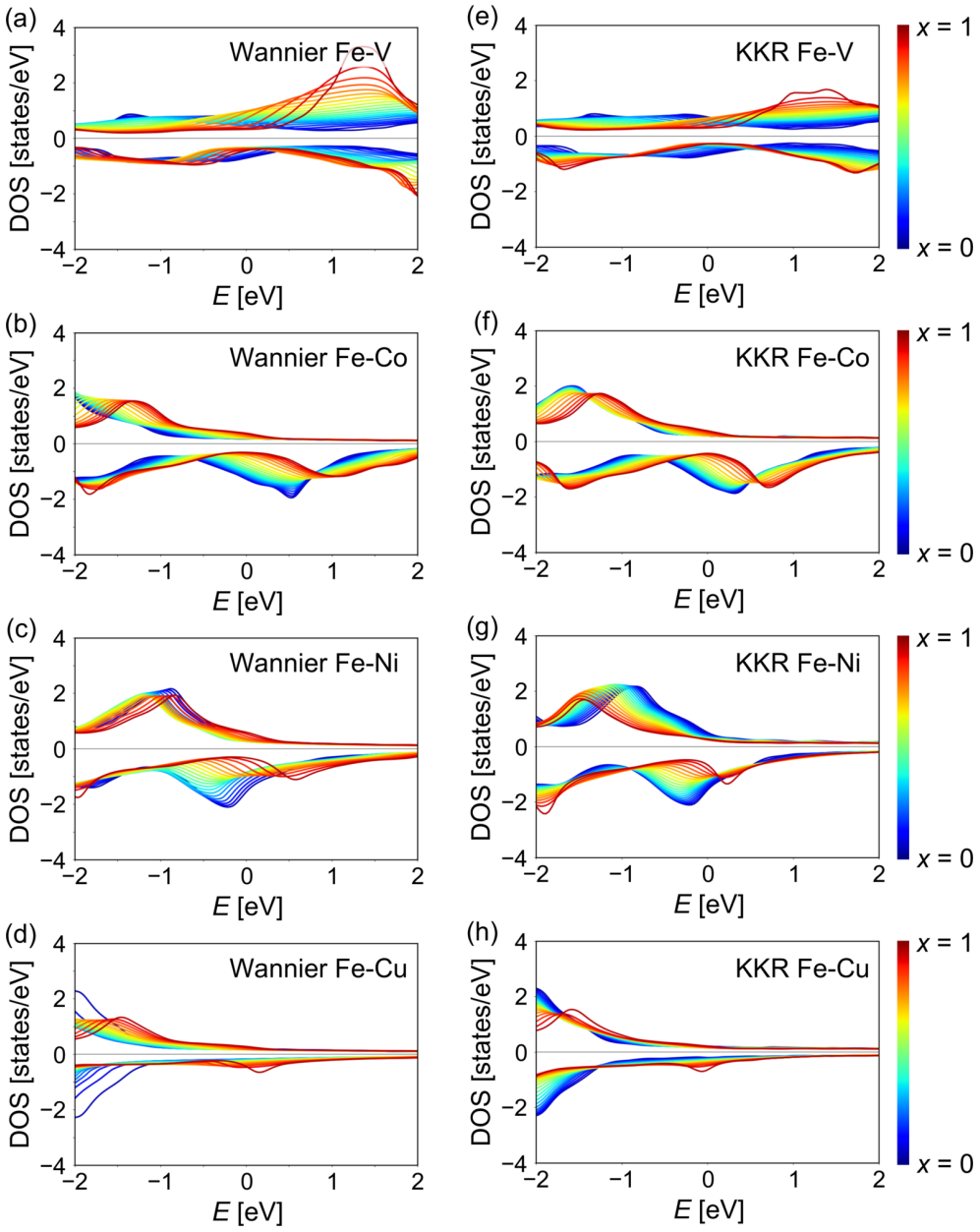

Figure 6.15: As for FIG. 6.13 but projected to X-component (X = V, Co, Ni, and Cu).

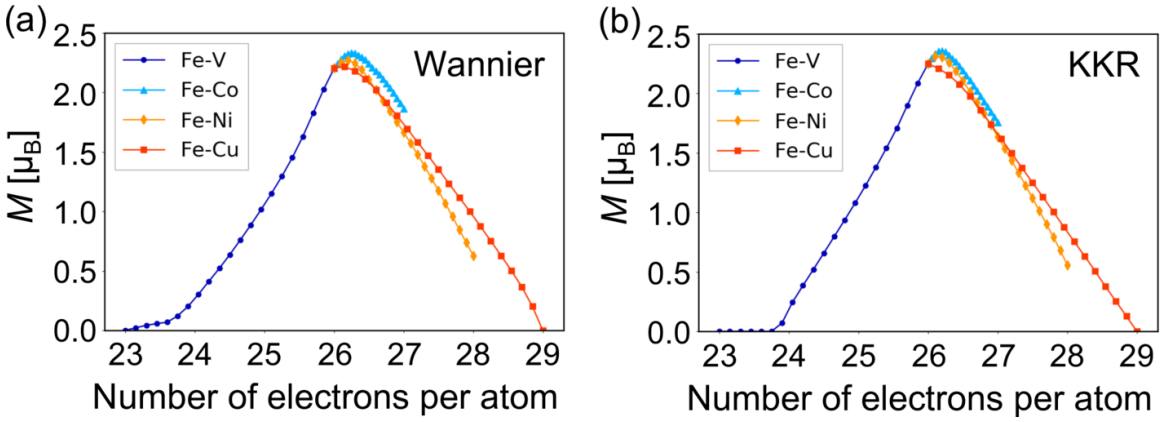

Figure 6.16: Magnetic moment of Fe-X (X = V, Co, Ni, and Cu) calculated by (a) the Wannier-CPA and (b) the KKR-CPA methods.

cerning the calculation of magnetic moments for the following reasons. First of all, the magnetic moments calculated by the Wannier-CPA method form a typical Slater-Pauling curve, which takes a maximum moment in the case of $Fe_{0.75}Co_{0.25}$ and intersects the horizontal axis at an angle of almost 45 degrees. Furthermore, the calculated magnetic moments in the bcc Fe-X (X = V, Co, Ni, and Cu) alloys by the Wannier-CPA method are in good agreement with those by the KKR-CPA method, since the average values of the deviation in magnetic moments are only 0.057, 0.064, 0.036, and 0.080 μ_B, respectively. These results represent that the Wannier-CPA method can be a powerful tool for the prediction of physical quantities expressed by the integral up to Fermi energy despite its simple formulation.

Since we set the reference values of the on-site potential by a simple method using supercell calculations, we discuss the effect of the change in the magnetic moment due to deviation from the actual reference values of the on-site potential. Since the difference of $\Delta v^{\text{supercell}}_{\text{Fe}-X}$ (X = V, Co, Ni, and Cu) obtained from Fe_1X_7 and Fe_7X_1 is within 1 eV [1], we calculated the magnetic moment of $Fe_{0.5}X_{0.5}$ by adding 0.5 eV to the diagonal terms of the on-site potential of X in the Wannier-CPA method. Then,

[1]The average and the difference of $\Delta v^{\text{supercell}}_{\text{Fe}-X}$ obtained from Fe_1X_7 and Fe_7X_1 (X = V, Co, Ni, and Cu) are -1.75 eV and 0.824 eV for V, 0.803 eV and 0.0656 eV for Co, 0.885 eV and 0.0599 eV for Ni, and 2.28 eV and 0.530 eV for Cu. For the detailed values, see Sec. 6.1.

we calculated the magnetic moment by subtracting 0.5 eV from the diagonal terms of the on-site potential of X and derived the difference between the two moments. We divided it by the magnetic moment calculated without changing the on-site potential and derived the rates of change in magnetic moment. These rates of change in the magnetic moment were only 6.55%, 2.07%, 0.23%, and 4.72% in $Fe_{0.5}V_{0.5}$, $Fe_{0.5}Co_{0.5}$, $Fe_{0.5}Ni_{0.5}$, and $Fe_{0.5}Cu_{0.5}$, respectively, even with the large difference of 1 eV in the on-site potential. Since the difference in the reference values of the on-site potentials between Fe and X from the actual values has only little effect on the physical quantities, this method using supercell can be a simple and valuable way for determining the relative difference of the on-site potentials of Fe and X.

6.6 Conclusion

We have formulated the CPA in the Wannier representation to develop a calculation method for homogeneous random alloys, which can be readily accessed from any first principles calculation methods. This Wannier-CPA method significantly reduces the computation time compared with those of the existing methods. Compared to the KKR-CPA method, this Wannier-CPA method can be expected to reduce the computational time by a factor of ten. To investigate the performance of this Wannier-CPA method, we have examined the Bloch spectral function, the DOS, and the magnetic moment for various Fe-based transition-metal alloys from the Green's function obtained by the Wannier-CPA method, and compared with the results of the calculation by the well-developed KKR-CPA method. Regarding the Bloch spectral function, the spectral structures of the Fe-Cu alloys were compared by both the Wannier-CPA and the KKR-CPA methods. We observed a blurred spectral structure of Fe near the Fermi energy in the spin-down state when the Fe content is low. On the other hand, we observed a clear virtual crystal-like spectral structure in the spin-up state. This is because of the similarity in the energy structure of Fe and Cu spin-up states. These behaviors are the same in both the Wannier-CPA and the KKR-CPA methods. Furthermore, by changing the concentration of Fe, we also found an energy shift in the peak structure of the DOS. This is the same for the Wannier-CPA and the KKR-CPA calculations for all of the Fe-X (X = V, Co, Ni, and Cu) alloys. Finally, we calculated the magnetic moment of the

Fe-X alloys. We can reproduce the well-known Slater-Pauling curve by the Wannier-CPA method that is quite similar to the KKR-CPA method, which confirms the good predictive power for physical quantities for the Wannier-CPA method. In this paper, we have discussed only the Bloch spectral function, the DOS, and the magnetic moment in the Wannier-CPA method. Nevertheless, one may conclude that this Wannier-CPA method have great applicability to other physical quantities and also large compound systems, which have many restrictions concerning the calculation time as the main bottleneck. The transport calculation should be one such example. Although there are many works on the anomalous and spin Hall effect using the Wannier functions, only the intrinsic contribution of the conductivity is considered in all these works. Using this formulation we have given, it can be possible to calculate the conductivity including the extrinsic contributions as well. To evaluate the potential of the developed Wannier-CPA method, we expect further applications of the method to various materials in addition to transition-metal alloys.

Chapter 7

Magnetic Properties of Fe-Cr Alloys

In the previous section, we dealt with the Fe-based transition metal alloys as target materials for the CPA calculations. However, we only focused on the Fe-V, Fe-Co, Fe-Ni, and Fe-Cu alloys and omit Fe-Cr and Fe-Mn alloys. This is because that antiferromagnetic phase transitions are predicted in these alloy systems in Cr-rich or Mn-rich regions [82, 83] which cannot be treated using one unit cell. Especially for pure bcc Cr, the ordered states is the sinusoidal spin density wave (SDW) and furthermore its wave vector is incommensurate with the bcc lattice. For the calculation of pure Cr having SDW states, we have to deal with a large number of Cr atoms such as 40 Cr per unit cell. It is a quite tough work to perform DFT calculations even for pure Cr as indicated in Ref. [82]. However, as a more practical calculation method of Cr, we performed the electronic structure calculations not for SDW state but for antiferromagnetic states having commensurate wave vector. In this chapter, we investigate the magnetic phase transition for Fe-Cr alloys by changing the relative concentration of Fe and Cr using unit cell having two atomic sites.

7.1 Computational Steps

The electric structure calculation of the KKR Green's function method is performed self-consistently by the fully relativistic spin-polarized Munich SPR-KKR package [79, 80]. For the exchange-correlation functional, the parametrization given by Vosko *et al.* [81] has been used. An angular momentum cutoff of $l_{\max} = 4$ was used for the KKR multiple-

scattering calculations. For the calculation of homogeneous random alloys, we exploited coherent potential approximation (CPA) [For the methodology and algorithm for the CPA calculation in the KKR method, see Sec. 4.4]. We set the lattice parameter a = 2.96 Å in KKR-CPA calculations that is about 3% larger than that of pure bcc Fe and Cr obtained by experiments. This is because that the magnetic structure of pure bcc Cr is not antiferromagnetic but nonmagnetic if we use the experimental lattice parameter. This is the artifact of the calculation of Cr that the ground state is nonmagnetic with equilibrium lattice constant about 1.6% below the experimental value [82]. To consider the antiferromagnetic phase transition in high Cr concentration, we prepared diatomic supercell having bcc structure. Each of the two sites in the supercell, we fill the same amount of Fe and Cr, but the direction of magnetic moments are not always the same. We refer to these two sites as site 1 and site 2, and Fe and Cr contained in each site as Fe1 and Cr1, and Fe2 and Cr2, respectively.

7.2 Magnetic Structure

To determine the magnetic structure of Fe-Cr alloys, we first performed SCF calculation in Fe-Cr diatonic supercell. There are six spin configurations in the diatomic supercell that can be written as {Fe1, Cr1, Fe2, Cr2} = {up, up, up, up}, {up, up, up, down}, {up, up, down, up}, {up, up, down, down}, {up, down, up, down}, and {up, down, down, up}. We performed SCF calculation using all of these configurations. However, we cannot obtain {Fe1, Cr1, Fe2, Cr2} = {up, up, down, up} state in all concentration of Fe and Cr because of its instability of the spin configuration. Figure 7.1 shows the Fe-concentration dependence of the total energy in Fe_xCr_{1-x} ($x = 0.0 \sim 0.3$). As the rate of change in total energy due to the concentration of Fe and Cr is much larger than the energy deference due to the difference in spin configurations, we subtracted $-886.73468 \times x - 4195.5871$ Ry, the regression curve in all configurations, from the total energy. Here, we only show the results in Cr-rich region since only {Fe1, Cr1, Fe2, Cr2} = {up, down, up, down} configuration is extremely stable in Fe-rich region. Therefore, there is no need to discuss the stability of other configuration in Fe-rich region.

In Fig. 7.1, some curves of the total energy with respect to Fe concentrations are ended in the middle. For {Fe1, Cr1, Fe2, Cr2} = {up, down, down, up} state which

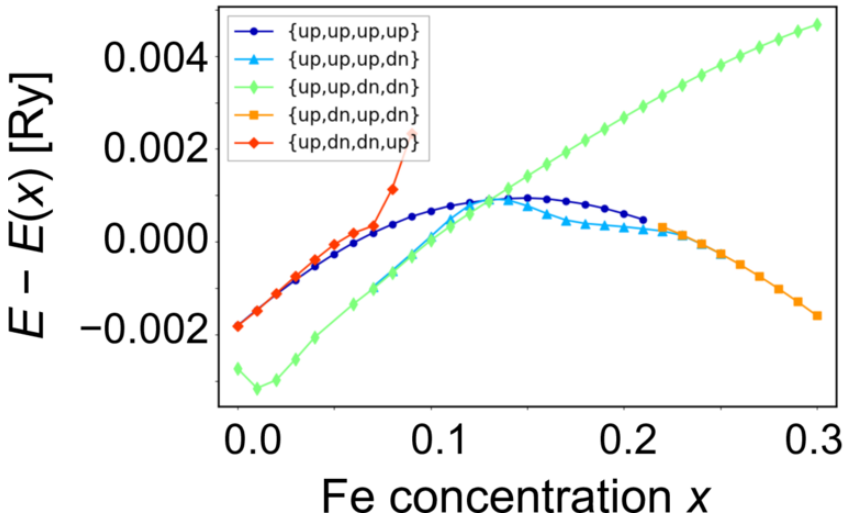

Figure 7.1: Fe-concentration dependence of the total energy in Fe_xCr_{1-x} alloys, where the Fe concentration is changed from $x = 0.0$ to $x = 0.3$. Since the energy deference due to the concentration of Fe is quite large, we subtracted $-886.73468 \times x - 4195.5871$ Ry from the total energy. The blue curve refers to the spin configuration of {Fe1, Cr1, Fe2, Cr2} = {up, up, up, up}, light-blue curve refers to {up, up, up, down}, green curve refers to {up, up, down, down}, orange curve refers to {up, down, up, down}, and red curve refers to {up, down, down, up} states.

is shown in red curve in Fig. 7.1, the configuration is not stable higher than Fe concentration of $x = 0.01$. The {Fe1, Cr1, Fe2, Cr2} = {up, up, up, up} state [blue curve in Fig. 7.1] changes continuously to {up, down, up, down} state [orange curve in Fig. 7.1] as the Fe concentration gets higher than $x = 0.22$. The {Fe1, Cr1, Fe2, Cr2} = {up, up, up, down} state [light-blue curve in Fig. 7.1] also changes continuously to {up, down, up, down} states when the Fe concentration is higher than $x = 0.26$, and Fe2 spin suddenly flip from spin-up to spin-down state when the Fe concentration is lower than $x = 0.06$. In Cr-rich region where the Fe concentration is lower than $x = 0.13$, the most stable configuration is {Fe1, Cr1, Fe2, Cr2} = {up, up, down, down} state. In this configuration, the magnetic moment of Cr becomes 1.0872 μ_B in pure Cr limit. This is a reasonable result since the magnetic moments of Cr are quite small values of

0.0000 μ_B and 0.0008 μ_B in the case of the {Fe1, Cr1, Fe2, Cr2} = {up, up, up, up} and {up, down, down, up} states, respectively. In $Fe_{0.13}Cr_{0.87}$, the total energy of {Fe1, Cr1, Fe2, Cr2} = {up, up, up, up}, {up, up, up, down}, and {up, up, down, down} are almost the same. This is consistent with the experimental results that there is the antiferromagnetic-to-ferromagnetic phase transition at about $x = 0.14$ and the spin-glass phase between the two magnetic phases [87, 88, 89, 90, 91, 92]. The most stable configuration is {Fe1, Cr1, Fe2, Cr2} = {up, up, up, down} when the Fe concentration is between $x = 0.13$ and $x = 0.24$. The magnetic structure is then changed to {Fe1, Cr1, Fe2, Cr2} = {up, down, up, down} state when the Fe concentration is larger than $x = 0.24$.

7.3 Magnetic Moment

To further investigate the element-specific magnetic properties in Fe-Cr alloys, we focus on the magnetic moment. Table 7.3 shows the total magnetic moment and the magnetic moment of each element in Fe-Cr alloys. The calculation was done for the spin configuration having lowest energy, that is, we exploit {Fe1, Cr1, Fe2, Cr2} = {up, up, down, down} state for the Fe-concentration of $x = 0.00 \sim 0.12$, {up, up, up, down} state for $x = 0.14 \sim 0.24$, and {up, down, up, down} state for $x = 0.26 \sim 0.30$. Here, we do not list the magnetic moment of Fe-Cr alloys having Fe-concentration larger than $x = 0.30$ since we only observed the gradual change in magnetic moments without phase transition in Fe-rich region.

We found that the magnetic moments of Fe and Cr tend to be aligned in the same direction in Cr-rich region. However, in Fe-rich side, the magnetic moments of Fe and Cr are arranged in opposite directions. Concerning the trsansition of the magnetic structure of Cr-Fe alloys, we observed a sudden flip of the magnetic moment of Fe2 between $x = 0.12$ and $x = 0.14$. On the contrary, the second transition of the magnetic structure between $x = 0.24$ and $x = 0.26$ is an gradual change of the magnetic moment of Cr1.

Table 7.1: Magnetic Moment of Fe-Cr Alloys

Concentration of Fe	Total Magnetic Moment [μ_B]	Magnetic Moment of Fe1 [μ_B]	Magnetic Moment of Cr1 [μ_B]	Magnetic Moment of Fe2 [μ_B]	Magnetic Moment of Cr2 [μ_B]
0.00	0.0000	1.4823	1.0872	-1.4823	-1.0872
0.02	0.0000	1.9704	1.0912	-1.9704	-1.0912
0.04	0.0000	2.2205	1.0664	-2.2205	-1.0664
0.06	0.0000	2.2973	1.0400	-2.2973	-1.0400
0.08	0.0000	2.3324	1.0131	-2.3324	-1.0131
0.10	0.0000	2.3495	0.9874	-2.3495	-0.9874
0.12	0.0000	2.3585	0.9618	-2.3585	-0.9618
0.14	0.5400	2.2947	0.8332	1.8439	-0.8791
0.16	0.6581	2.2967	0.7437	1.9805	-0.7750
0.18	0.7728	2.2967	0.6297	2.0732	-0.6465
0.20	0.8758	2.2919	0.5067	2.1323	-0.5179
0.22	0.9710	2.2834	0.3706	2.1760	-0.3835
0.24	1.0664	2.2476	0.0036	2.2446	-0.0191
0.26	1.1507	2.2528	-0.0141	2.2528	-0.0141
0.28	1.2349	2.2599	-0.0213	2.2599	-0.0213
0.30	1.3191	2.2670	-0.0294	2.2670	-0.0294

7.4 Anomalous Hall Conductivity

We performed the calculation of the anomalous Hall conductivity using the KKR-CPA method. We exploited the Kubo-Bastin formula implemented in the SPR-KKR code for the calculation of the conductivity. For the diatomic Fe-Cr supercell, we couldn't make the calculation converged even with the 10 million $\boldsymbol{k}$-vector mesh. Therefore, we performed the calculation only for the unit cell having single atomic site. This calculation cannot describe the magnetic transition of Fe-Cr alloys in Cr-rich region since it cannot present the antiferromagnetic configuration of the magnetic moments. However, we can obtain reasonable results for the Fe-rich region where the Fe-Cr alloys have ferromagnetic spin configurations.

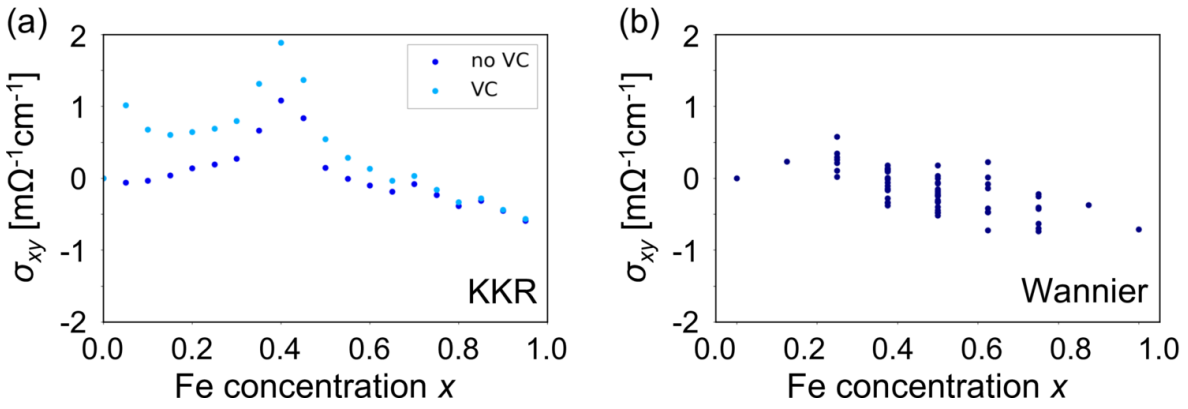

Figure 7.2: (a) Anomalous Hall conductivity calculated by the KKR-CPA method for Fe-Cr alloys exploiting Kubo-Bastin formula. The blue dots indicate the calculation results of the conductivity without vertex corrections, while light-blue dots indicate the results with vertex corrections. (b) Intrinsic contribution of the anomalous Hall conductivity calculated by using the Wannier function in Fe-Cr eight-atomic supercell.

Figure 7.2(a) shows the anomalous Hall conductivity calculated by the KKR-CPA methods. In the figure, blue dots shows the intrinsic contribution of the anomalous Hall conductivity, whereas the light-blue dots shows the conductivity including external contributions. Here, we performed the calculation using the lattice constant $a = 2.86$ Å which is the experimental value of bcc Fe. We observed a peak structure in the conductivity near the flipping point of the magnetic moment of Cr.

We have an interest whether the peak structure of the anomalous Hall conductivity can be reproduced by the supercell calculation using Wannier formalism. For the calculation of the conductivity, we prepared the eight-atomic supercell. We filled the eight-atomic sites by Fe or Cr and performed the SCF calculations with all possible atomic configurations. Since we have to exploited as much as 27 million $\boldsymbol{k}$-vector mesh to make the calculation converged, we reduced the calculation time by using the crystal symmetry. The calculation method of the anomalous Hall conductivity and its symmetry operations are summarized in Appendix B.

Figure 7.2(b) shows the anomalous Hall conductivity calculated by Wannier formalism. Here, we excluded the results of some atomic configurations in which the SCF calculations were not converged because of the energy instability. We only focused on

the intrinsic contribution of the anomalous Hall conductivity. Concerning the extrinsic contributions, the calculation method has not been developed in Wannier representation. As shown in Fig. 7.2(b) the anomalous Hall conductivity is gradually increased and changes its sign as the Cr concentration is increased. However, the values of the anomalous Hall conductivity differ significantly depending on the arrangement of Fe and Cr atoms even though the concentration of Fe and Cr is the same. In real alloys the ensemble average with randomly arranged Fe and Cr should be measured depending on the energy stability of the Fe and Cr configurations in the crystal. The results present the limits of the application of the supercell for the calculation of the physical quantities in random alloys. For a more sophisticated way for the calculation of supercell, a method using the special quasirandom structure (SQS) developed by Zunger et al. [86] is known. In this methods the minimally-sized supercell that mimics physically most relevant radial correlation functions of a perfectly random structure is used.

7.5 Conclusion

In this chapter, we performed the CPA calculation in bcc Fe-Cr alloys. To investigate the transition of the magnetic structure in these alloys, we performed the SCF calculations using a diatomic supercell. Form the relative size difference in the total energy of the diatomic supercell, we concluded that there are two transition of the magnetic structure in Fe-Cr alloys as the concentration of Fe is increased. In Cr-rich region, the Fe-Cr alloys have the antiferromagnetic configuration as suggested by the antiferromagnetism of pure bcc Cr and the magnetic moments of Fe and Cr are in the same directions. On the other hand, the Fe-Cr alloys have the ferromagnetic configuration in Fe-rich region where the magnetic moments of Fe and Cr are in opposite directions. We examined the magnetic moment of Fe and Cr at each site of the supercell and found that the magnetic moment of one of the Fe sites sharply flips at the first transition in the Cr-rich region. On the contrary, the second transition is a gradual change in the magnetization of Cr. Finally, we performed the calculation of the anomalous Hall conductivity. In the results of the KKR-CPA methods, we observed a peak structure in conductivity. However, we could not reproduce the peak structure when we calculated the intrinsic contribution of the anomalous Hall conductivity in eight-atomic supercell

using Wannier representation. One of the reason is that the conductivity changes a lot depending on the configuration of Fe and Cr in the supercell. Further investigations are necessary for the calculation of Fe-Cr alloys.

Chapter 8

Summary

In this study, we aimed to develop an efficient method for the calculation of alloy systems. To achieve this purpose, we focused on the Wannier formulation. This is because that Wannier functions can be constructed from any kind of first-principles calculation method if the wave function is available. Therefore, we can obtain the computation method that is independent on the applied first-principles electric structure code. We exploited the CPA method which is the most sophisticated method for treating homogeneous random alloys. To incorporate the CPA into Wannier representation, we investigated the KKR Green's function method in which the implementation of CPA is well-established and developed the algorithm that has the same structure as the Mills' algorithm used in the KKR method. This Wannier-CPA method required quite low computational effort compared to the KKR method.

Chapter 6: Application of the Wannier-CPA Method to Fe-based transition-metal alloys

In this chapter we applied the Wannier-CPA method we have developed in Chapter 5 to Fe-based 3d transition-metal alloys Fe-X (X = V, Co, Ni, and Cu). To verify the performance of the Wannier-CPA methods we compared the Bloch spectral function, the DOS, and the magnetic moment calculated by the Wannier-CPA method in Fe-X alloys with those calculated by the KKR-CPA method. Concerning the ambiguity of the reference values of the on-site potential, we proposed a simple method to exploit the supercell calculations and took concentration average for the site off-diagonal terms

which was suggested by the previous studies on the TB-CPA and the LCAO-CPA methods. Even though the calculation time in the Wannier-CPA method was reduced to about 1/10 compared to that in the KKR-CPA method, these physical quantities obtained by the Wannier-CPA method well reproduced the results by the KKR-CPA method.

Chapter 7: Magnetic Properties of Fe-Cr Alloys

In this chapter we focused on the Fe-Cr alloys which have antiferromagnetism in Cr-rich region. To investigate the magnetic structure of these alloys, we exploited the diatomic supercell with a bcc structure. As we expected we observed an antiferromagnetic phase in Cr-rich region while we obtained ferromagnetic phase in Fe-rich region. We also observed an intermediate phase in which the magnetic moments in the two atomic sites are asymmetric. We performed the calculation of the anomalous Hall conductivity for Fe-Cr alloys. In the results of the conductivity calculated by the KKR-CPA method, a peak structure appeared when we changed the concentration of Fe and Cr. However, we could not reproduce the peak structure by the supercell calculations in Wannier representation. Further investigations such as the SQS and the Wannier-CPA implementation of the conductivity calculations might be necessary to treat these alloy systems.

Concerning the Wannier-CPA methods, we only presented the computation results of the physical quantities expressed by single Green's function in this thesis. However, we are confident that this new approach can be a significant step towards an efficient calculation of other physical quantities such as the anomalous and spin Hall effect in homogeneous random alloys that cannot be handled by the conventional Wannier representation. Furthermore, the Wannier-CPA method has potential applicability to large compound systems because of its low computational cost needed. This new CPA method will open a new avenues for developing future material researches in alloy systems.

Appendix A

Determination of the Fermi Energy

In this section we schematically illustrate the calculation method of the Fermi energy in the Wannier-CPA method [Fig. A.1]. Since the coherent potential depends on the energy, we have to perform complex integration on the Green's function to determine the number of states. For the obtained number of states, we determine the Fermi energy as follows.

The number of states $N(E)$ for a certain energy E is given by

$$N(E) = \int_0^E \mathrm{d}E' \rho(E') \ . \tag{A.1}$$

Here, $\rho(E)$ is the density of states for the energy E. Considering the shaded area in Fig. A.1, we can approximate the difference of the number of states ΔN in the case we exploit the temporary Fermi energy $\tilde{E}_{\mathrm{F}}$ as

$$\Delta N \approx \rho(\tilde{E}_{\mathrm{F}}) \times \Delta E \ . \tag{A.2}$$

Therefore, we can estimate the actual Fermi energy for the system as

$$E_{\mathrm{F}} = \tilde{E}_{\mathrm{F}} + \Delta E = \tilde{E}_{\mathrm{F}} + \frac{N - N(\tilde{E}_{\mathrm{F}})}{\rho(\tilde{E}_{\mathrm{F}})} \ . \tag{A.3}$$

For the computation, we repeat this scheme until the difference ΔN becomes smaller than the threshold.

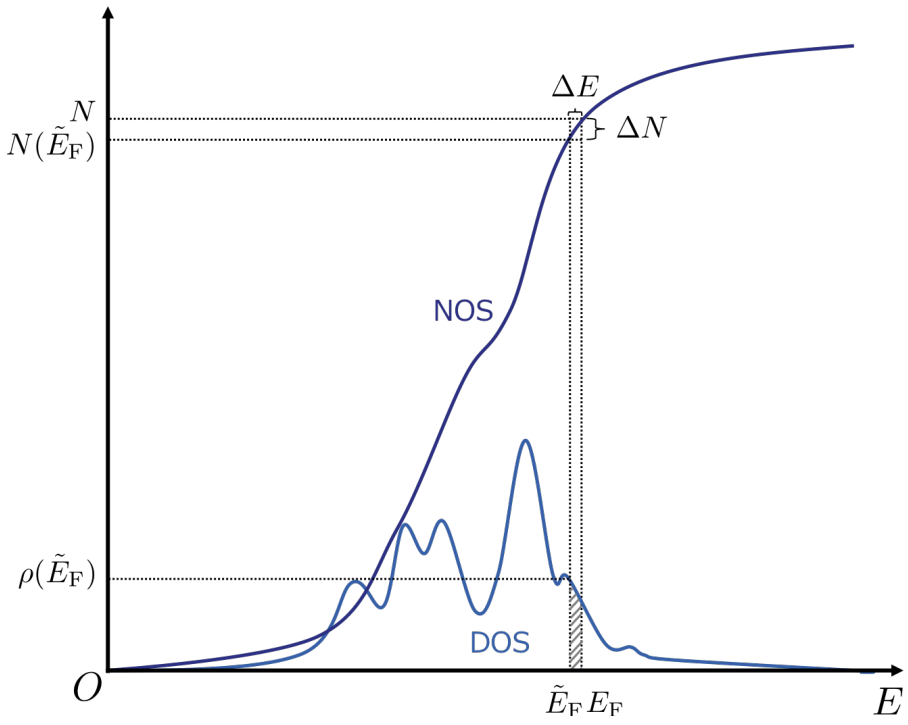

Figure A.1: The schematic illustration of the method to determine the Fermi energy where $\tilde{E}_{\mathrm{F}}$ is the temporary Fermi energy while E_{F} used in the calculation is the actual Fermi energy.

Appendix B

Anomalous Hall Conductivity Calculation in Wannier Representation

In Sec. 7.4 we performed the calculation of the intrinsic contribution of the anomalous Hall conductivity in Wannier representation. We exploited the method given by Wang et. al. [47]. In this appendix, we briefly summarize the calculation methods using Wannier functions and its symmetry operations.

B.1 Formulation

The intrinsic contribution of the anomalous Hall conductivity is given by the following BZ integral

$$\sigma_{\alpha\beta}(\mu, T) = -\frac{e^2}{\hbar} \sum_n \int_{\mathrm{BZ}} \frac{\mathrm{d}\boldsymbol{k}}{(2\pi)^3} \Omega_{n,\alpha\beta}(\boldsymbol{k}) f(\varepsilon_{n\boldsymbol{k}} - \mu, T) \ , \tag{B.1}$$

where $f(\varepsilon_{n\boldsymbol{k}} - \mu, T)$ is the Fermi distribution function

$$f(\varepsilon_{n\boldsymbol{k}} - \mu, T) = \frac{1}{e^{\beta(\varepsilon_{n\boldsymbol{k}} - \mu)} + 1} \ , \tag{B.2}$$

with $\beta = 1/k_{\mathrm{B}}T$ and $\Omega_{n,\alpha\beta}(\boldsymbol{k})$ is called the Berry curvature that is the rotation of the Berry connection $A_{nm,\alpha}(\boldsymbol{k})$

$$\Omega_{n,\alpha\beta}(\boldsymbol{k}) = \frac{\partial A_{nn,\beta}(\boldsymbol{k})}{\partial k_\alpha} - \frac{\partial A_{nn,\alpha}(\boldsymbol{k})}{\partial k_\beta} \ . \tag{B.3}$$

Here, the Berry connection is represented as follows:

$$A_{nm,\alpha}(\boldsymbol{k}) = i \int_{\Omega_{\text{cell}}} \mathrm{d}\boldsymbol{r} u^*_{n\boldsymbol{k}}(\boldsymbol{r}) \frac{\partial u_{m\boldsymbol{k}}(\boldsymbol{k})}{\partial k_\alpha} \ , \tag{B.4}$$

where $u_{n\boldsymbol{k}}(\boldsymbol{k})$ are the cell-periodic Bloch functions and the following relation holds for the Bloch function $\psi_{n\boldsymbol{k}}(\boldsymbol{r})$

$$\psi_{n\boldsymbol{k}}(\boldsymbol{r}) = e^{i\boldsymbol{k}\cdot\boldsymbol{r}} u_{n\boldsymbol{k}}(\boldsymbol{r}) \ . \tag{B.5}$$

B.2 Gauge Transformation

We perform a gauge transform to the Berry connection

$$\tilde{\boldsymbol{A}}_{nm}(\boldsymbol{k}) = i \int_{\text{cell}} \mathrm{d}\boldsymbol{r} \tilde{u}^*_{n\boldsymbol{k}}(\boldsymbol{r}) \nabla_{\boldsymbol{k}} \tilde{u}_{m\boldsymbol{k}}(\boldsymbol{r}) \ , \tag{B.6}$$

where $\tilde{u}_{n\boldsymbol{k}}(\boldsymbol{r})$ is given by

$$\tilde{u}_{n\boldsymbol{k}}(\boldsymbol{r}) = \sum_q U^{(\boldsymbol{k})}_{qn} u_{q\boldsymbol{k}}(\boldsymbol{r}) \ . \tag{B.7}$$

The operator $U^{(\boldsymbol{k})}_{qn}$ is the unitary matrix which is defined in Sec. 5.1. We will represent the Berry connection $\boldsymbol{A}_{nm}(\boldsymbol{k})$ in terms of the gauge transformed one $\tilde{\boldsymbol{A}}_{nm}(\boldsymbol{k})$ since the expected values expressed by Wannier functions such as Eq. (5.8) are the quantities after the transformation. Here, we show the final results

$$\boldsymbol{A}_{nm}(\boldsymbol{k}) = \tilde{\boldsymbol{A}}^{(U^\dagger)}_{nm}(\boldsymbol{k}) + \boldsymbol{D}^{(U^\dagger)}_{nm}(\boldsymbol{k}) \ , \tag{B.8}$$

where $\tilde{\boldsymbol{A}}^{(U^\dagger)}_{nm}(\boldsymbol{k})$ and $\boldsymbol{D}^{(U^\dagger)}_{nm}(\boldsymbol{k})$ are given by

$$\tilde{\boldsymbol{A}}^{(U^\dagger)}_{nm}(\boldsymbol{k}) = \sum_{q,q'} U^{(\boldsymbol{k})}_{nq} \tilde{\boldsymbol{A}}_{qq'}(\boldsymbol{k}) U^{(\boldsymbol{k})\dagger}_{q'm} \ , \tag{B.9}$$

$$\boldsymbol{D}^{(U^\dagger)}_{nm}(\boldsymbol{k}) = i \sum_q U^{(\boldsymbol{k})}_{nq} \nabla_{\boldsymbol{k}} U^{(\boldsymbol{k})\dagger}_{qm} \ . \tag{B.10}$$

For the computation of the values $\boldsymbol{D}^{(U^\dagger)}_{nm}(\boldsymbol{k})$ we exploit the following relation

$$-i\boldsymbol{D}^{(U^\dagger)}_{nm}(\boldsymbol{k}) = \frac{\sum_{q,q'} U^{(\boldsymbol{k})}_{nq} [\nabla_{\boldsymbol{k}} \tilde{H}^{(\boldsymbol{k})}_{qq'}] U^{(\boldsymbol{k})\dagger}_{q'm}}{\varepsilon_{m\boldsymbol{k}} - \varepsilon_{n\boldsymbol{k}} \ .} \tag{B.11}$$

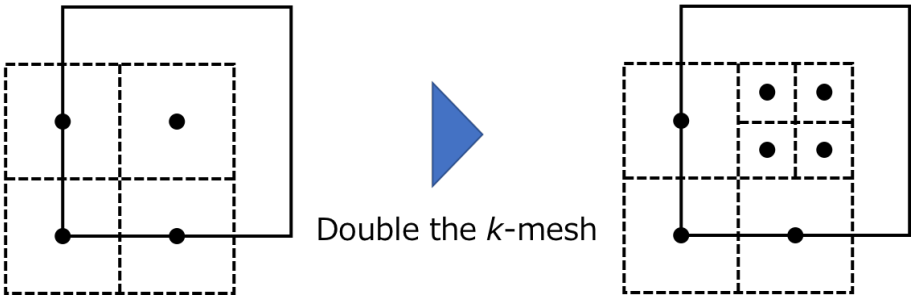

Figure B.1: The schematic illustration of the adaption of the k-mesh. The left-side figure shows the original k-mesh used for the calculation of conductivity. If the conductivity at the upper right point is larger than the threshold, the k-mesh is retaken as shown in the right-side figure.

in the case of $n \neq m$ where $\varepsilon_{n\boldsymbol{k}}$ is the energy eigenfunction of the Bloch function

$$\hat{H}(\boldsymbol{r})\psi_{n\boldsymbol{k}}(\boldsymbol{r}) = \varepsilon_{n\boldsymbol{k}}\psi_{n\boldsymbol{k}}(\boldsymbol{r}) \ , \tag{B.12}$$

and $\tilde{H}^{(\boldsymbol{k})}_{qq'}$ is given by

$$\tilde{H}^{(\boldsymbol{k})}_{nm} = \sum_{\boldsymbol{R}} e^{i\boldsymbol{k}\cdot\boldsymbol{R}} \int_{\text{all}} \mathrm{d}\boldsymbol{r} w^*_n(\boldsymbol{r})\hat{H}(\boldsymbol{r})w_m(\boldsymbol{r}-\boldsymbol{R}) \ . \tag{B.13}$$

According to Ref. [47], the Berry curvature can be approximated as follows:

$$\sum_n \Omega_{n,\alpha\beta}(\boldsymbol{k}) f(\varepsilon_{n\boldsymbol{k}} - \mu) \approx i \sum_{n\neq m} D^{(U^\dagger)}_{nm,\alpha}(\boldsymbol{k}) D^{(U^\dagger)}_{mn,\beta}(\boldsymbol{k}) \ . \tag{B.14}$$

The important point here is that we can perform the calculation of the Berry curvature independently for each k-points. Therefore, it is easy to reduce the number of k-points used for the calculation of the conductivity by symmetry operation which will be discussed in the following sections.

B.3 Symmetry Operation

For the calculation of the intrinsic contribution of the anomalous Hall conductivity, we have to exploit millions to tens of millions of k-vector mesh. Since the intrinsic conductivity is originated in the geometrical structures of the energy band, especially

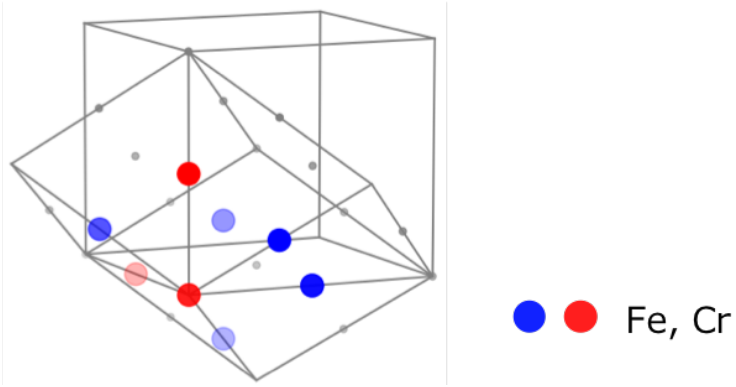

Figure B.2: One of the eight-atomic supercell of Fe-Cr we exploited for the calculation of the anomalous Hall conductivity. The blue and red dots represent the atomic site of Fe and Cr we used for the calculation. The gray dots are the other atomic site for bcc lattice. Here, we also show the unit cell we used and its conventional cell.

the singular structures such as the Weyl points, we have to pick up all the effects of these structures by using fairly large number of k-points. In Sec. 7.4 we exploited eight-atomic supercell for the calculation of the conductivity. However, it is not realistic to apply the formulation of the Berry curvature we present for such a large system. We exploit two methods to reduce the calculation time.

The first method is quite simple: we increase the number of k-points only for the region in k-space where the Berry curvature takes a value larger than the threshold. We present a schematic illustration in Fig. B.1. In this case the upper right k-point is retaken to double the number in each direction. For the actual computation we quadruple the number of k-mesh where the Berry curvature takes a large value.

The other method is to use the crystal symmetry. In the cubic crystal system we used there are up to 48 symmetry operations. Since we are targeting magnetic crystals, the number of symmetry operations is less than 48. Nevertheless, it is still possible to save a considerable amount of computation time by reducing the k-points used for the calculation. As an example, we show one of the eight-atomic supercell of Fe-Cr in Fig. B.2. The atomic site we exploited is represented by red and blue dots. If we perform a symmetric operation around the atom at the corner of the conventional cell,

we obtain

$$\{E|\mathbf{0}\},\ \{C_{2z}|\mathbf{0}\},\ \{C_{4z}^{+}|\tfrac{1}{2}\boldsymbol{c}\},\ \{C_{4z}^{-}|\tfrac{1}{2}\boldsymbol{c}\},\ \{I|\mathbf{0}\},\ \{\sigma_z|\mathbf{0}\},\ \{S_{4z}^{-}|\tfrac{1}{2}\boldsymbol{c}\},\ \{S_{4z}^{+}|\tfrac{1}{2}\boldsymbol{c}\}$$

for unitary operations. For the anti-unitary operations we have

$$\{C_{2x}|\mathbf{0}\},\ \{C_{2y}|\mathbf{0}\},\ \{C_{2a}|\tfrac{1}{2}\boldsymbol{c}\},\ \{C_{2b}|\tfrac{1}{2}\boldsymbol{c}\},\ \{\sigma_x|\mathbf{0}\},\ \{\sigma_y|\mathbf{0}\},\ \{\sigma_{da}|\tfrac{1}{2}\boldsymbol{c}\},\ \{\sigma_{db}|\tfrac{1}{2}\boldsymbol{c}\}\ .$$

Here, we supposed that all of the magnetic moments point in the z-direction. There are as much as 16 symmetry operations and if we use one million k-mesh for the calculation of the conductivity, we can reduce the number of k-points to 65,701. We created a calculation code to determine the crystal symmetry based on the symmetric operation program implemented in the SPR-KKR and QUANTUM ESPRESSO packages.

B.4 Symmetry of Berry Curvature

Finally, we mention the Berry curvature under the symmetry operations. Suppose that the Hamiltonian of a crystal is invariant under the unitary operation U

$$UHU^{-1} = H\ . \tag{B.15}$$

Since we only focus on the symmetry operation in a crystal, the unitary operation U can be written as

$$U = S = \{R|\boldsymbol{t}\}\ , \tag{B.16}$$

where R is the rotation or inversion of the lattice vectors and $\boldsymbol{t}$ represents a translation. Under the operation U, we obtain the following relation for the Bloch functions

$$\psi_{n\boldsymbol{k}}(S^{-1}\boldsymbol{r}) = \psi_{nR\boldsymbol{k}}(\boldsymbol{r})\ . \tag{B.17}$$

Here, the phase is set to one since the phase is arbitrary when calculating the Berry curvature. By directly substituting Eq. (B.17) into the definition of the Berry curvature [Eq. (B.3)], we obtain

$$\boldsymbol{\Omega}_n(R\boldsymbol{k}) = \begin{cases} R^{-1}\boldsymbol{\Omega}_n(\boldsymbol{k}) & \text{(rotation)}\ , \\ -R^{-1}\boldsymbol{\Omega}_n(\boldsymbol{k}) & \text{(inversion)}\ . \end{cases} \tag{B.18}$$

It is evident from Eq. (B.18) that we only need to consider the rotation or inversion in the k-space.

Next, we consider the case that the Hamiltonian of a crystal is invariant under the anti-unitary operation A

$$AHA^{-1} = H \ . \tag{B.19}$$

For the anti-unitary operator, we refer to the operation that the rotation or inversion itself is not the symmetry operation but it can be a symmetry operation when including time reversal

$$A = \Theta S \ . \tag{B.20}$$

Under the operation A, the following relation holds for the Bloch function:

$$\left[\psi_{n\boldsymbol{k}}(S^{-1}\boldsymbol{r})\right]^* = \psi_{n-R\boldsymbol{k}}(\boldsymbol{r}) \ . \tag{B.21}$$

Therefore, we obtain

$$\boldsymbol{\Omega}_n(-R\boldsymbol{k}) = \begin{cases} -R^{-1}\boldsymbol{\Omega}_n(\boldsymbol{k}) & \text{(rotation)} \ , \\ R^{-1}\boldsymbol{\Omega}_n(\boldsymbol{k}) & \text{(inversion)} \ , \end{cases} \tag{B.22}$$

for the anti-unitary operations.

References

[1] See http://www.github.com/materialsproject for downloadable source code and documentation.

[2] S. Curtarolo, W. Setyawan, G. L. W. Hart, M. Jahnatek, R. V. Chepulskii, R. H. Taylor, S. Wang, J. Xue, K. Yang, O. Levy, M. J. Mehl, H. T. Stokes, D. O. Demchenko, and D. Morgan, AFLOW: An automatic framework for high-throughput materials discovery. Comput. Mater. Sci. **58**, 218 (2012).

[3] J. E. Saal, S. Kirklin, M. Aykol, B. Meredig, and C. Wolverton, JOM **65**, 1501 (2013).

[4] S. Kirklin, J. E. Saal, B. Meredig, A. Thompson, J. W. Doak, M. Aykol, S. Rühl, and C. Wolverton, Npj Comput. Mater. **1**, 15010 (2015).

[5] Y. Hinuma, T. Hatakeyama, Y. Kumagai, L.A. Burton, H. Sato, Y. Muraba, S. Iimura, H. Hiramatsu, I. Tanaka, H. Hosono, F. Oba, Nat. Commun. **7**, 11962 (2016Nature).

[6] A. Sakai, S. Minami, T. Koretsune, T. Chen, T. Higo, Y. Wang, T. Nomoto, M. Hirayama, S. Miwa, D. Nishio-Hamane, F. Ishii, R. Arita, S. Nakatsuji, Nature **581**, 53 (2020).

[7] M. Obstbaum, M. Decker, A. K. Greitner, M. Haertinger, T. N. G. Meier, M. Kronseder, K. Chadova, S. Wimmer, D. Ködderitzsch, H. Ebert, and C. H. Back, Phys. Rev. Lett. **117**, 167204 (2016).

[8] J. K. Furdyna, J. Appl. Phys., **64**, R31 (1988).

[9] J. S. Faulkner, Prog. Mater. Sci. **27**, 1 (1982).

[10] W. M. Temmerman and Z. Szotek, Comp. Phys. Rep. **5**, 175 (1987).

[11] E. N. Economou, Green's Functions in Quantum Physics, (Springer, Berlin, 2006).

[12] L. Nordheim, Ann. Physik **9**, 607 (1931).

[13] T. Muto, Sci. Papers Inst. Phys. Chem. Res. (Tokyo) **34**, 377 (1938).

[14] J. Korringa, J. Phys. Chem. Solids **7**, 252 (1958).

[15] J. Beeby, Phys. Rev. **135A**, 130 (1964).

[16] P. Soven, Phys. Rev. **156**, 809 (1967).

[17] D.W. Taylor, Phys. Rev. **156**, 1017 (1968).

[18] H. Shiba, Prog. Theor. Phys. **46**, 77 (1971).

[19] B. L. Gyorffy and G. M. Stocks, J. Phys. (Paris), Colloq. **35**, C4-75 (1974).

[20] B. L. Gyorffy, Phys. Rev. B **5**, 2382 (1972).

[21] J. S. Faulkner and G. M. Stocks, Phys. Rev. B **21**, 3222 (1980).

[22] H. Akai, Phys. Rev. Lett. **81**, 3002 (1998).

[23] K. Sato, P. H. Dederichs, and H. Katayama-Yoshida, Hyperfine Interact. **160**, 57 (2005)

[24] H. Ebert and S. Mankovsky, Phys. Rev. B **79**, 045209 (2009).

[25] S. Lowitzer, D. Ködderitzsch, and H. Ebert, Phys. Rev. Lett. **105**, 266604 (2010).

[26] S. Lowitzer, M. Gradhand, D. Ködderitzsch, D. V. Fedorov, I. Mertig, and H. Ebert, Phys. Rev. Lett. **106**, 056601 (2011).

[27] W. H. Butler, Phys. Rev. B **31**, 3260 (1984).

[28] J. Banhart, Philos. Mag. B **77**, 85 (1998).

[29] J. Banhart, Philos. Mag. B **77**, 105 (1998).

[30] B. Zimmermann, K. Chadova, D. Ködderitzsch, S. Blügel, H. Ebert, D. V. Fedorov, N. H. Long, P. Mavropoulos, I. Mertig, Y. Mokrousov, and M. Gradhand, Phys. Rev. B **90**, 220403(R) (2014).

[31] S. H. Liu, Phys. Rev. B 15, 4281 (1977).

[32] C. S. Wang, R. E. Prange, and V. Korenman, Phys. Rev. B **25**, 5766 (1982).

[33] T. Oguchi, K. Terakura, and N. Hamada, J. Phys. F: Met. Phys. **13**, 145 (1983).

[34] A. I. Liechtenstein, M. I. Katsnelson, and V. A. Gubanov, J. Phys. F: Met. Phys. **14**, L125 (1984).

[35] A. I. Liechtenstein, M. I. Katsnelson, and V. A. Gubanov, Solid State Commun. **54**, 327 (1985).

[36] B. L. Gyorffy, A. J. Pindor, J. Staunton, G. M. Stocks, and H. Winter, J. Phys. F: Met. Phys. **15**, 1337 (1985).

[37] J. Staunton, B. L. Gyorffy, G. M. Stocks, and J. Wadsworth, J. Phys. F: Met. Phys. **16**, 1761 (1986).

[38] A. I. Liechtenstein, M. I. Katsnelson, V. P. Antropov, and V. A. Gubanov, J. Magn. Mag. Mater. **67**, 65 (1987).

[39] H. Akai, Hyperfine Interact. **68**, 3 (1992).

[40] J. Kudrnovský, V. Drchal, and J. Mašek, Phys. Rev. B **35**, 2487 (1987).

[41] R. Richter, H. Eschrig, and B. Velicky J. Phys. F: Met. Phys. **17**, 351 (1987).

[42] R. Richter and H. Eschrig, J. Phys. F: Met. Phys. **18**, 1813 (1988).

[43] K. Hyodo, A. Sakuma, and Y. Kota, Phys. Rev. B bf 94, 104404 (2016).

[44] D. Wagenknecht, L. Šmejkal, Z. Kašpar, J. Sinova, T. Jungwirth, J. Kudrnovský, K. Carva, and I. Turek, Phys. Rev. B **99**, 174433 (2019).

[45] I. Turek, J. Kudrnovsky, and V. Drchal, Phys. Rev. B **100**, 134435 (2019).

[46] N. Marzari, A. A. Mostofi, J. R. Yates, I. Souza, and D. Vanderbilt, Rev. Mod. Phys. **84**, 1419 (2012).

[47] X. Wang, J. R. Yates, I. Souza, and D. Vanderbilt Phys. Rev. B **74**, 195118 (2006).

[48] T. Nomoto, T. Koretsune, and R. Arita, Phys. Rev. B **102**, 014444 (2020).

[49] G. Pizzi, D. Volja, B. Kozinsky, M. Fornari, and N. Marzari, Comput. Phys. Commun, **185**, 422 (2014).

[50] S. Poncé, E. R. Margine, C.Verdi, F.Giustino, Comput. Phys. Commun, **209**, 116 (2016).

[51] M. G. Lopez, David Vanderbilt, T. Thonhauser, and Ivo Souza, Phys. Rev. B **85**, 014435 (2012)

[52] Q. S. Wu, S. N. Zhang, H.-F. Song, M. Troyer, and A. A. Soluyanov, Comput. Phys. Commun. **224**, 405 (2018).

[53] S. S. Tsirkin, NPJ Comput. Mater. **7**, 33 (2021). See also https://wannier-berri.org/.

[54] D. Mourada and G. Czycholl, Eur. Phys. J. B **85**, 153 (2012).

[55] M. Köhl, C. Wolff, and K. Busch, Opt. Lett. **37**, 560 (2012).

[56] M. Born and J. R. Oppenheimer, Ann. Physik. **84**, 457 (1927).

[57] P. Hohenberg and W. Kohn, Phys. Rev. **136**, B864 (1964).

[58] W. Kohn and L. J. Sham, Phys. Rev. **140** A1133 (1965).

[59] A. K. Rajagopal and J. Callaway, Phys. Rev. B **7**, 1912 (1973).

[60] M. V. Ramana and A. K. Rajagopal, J. Phys. C: Solid State Phys. **12**, L845 (1979).

[61] J. Korringa, Physica, **13**, 392 (1947).

[62] W. Kohn and N. Rostoker, Phys. Rev. **140**, 1111 (1954).

[63] F. S. Ham and B. Segall, Phys. Rev. **124**, 1786 (1961).

[64] B. L. Gyorffy and M. J. Stott, Band Structure Spectroscopy off Metals and Alloys, (Academic Press, New York, 1973).

[65] F. Yonezawa and K. Morigaki, Suppl. Prog. Theor. Phys. **53** 1 (1973).

[66] B. Veliký, S. Kirkpatrick, and H. Ehrenreich, Phys. Rev. **175**, 747 (1968).

[67] R. Mills, L. J. Gray, and T. Kaplan, Phys. Rev. B **27**, 3252 (1983).

[68] B. Ginatempo and J. B. Staunton, J. Phys. F: Met. Phys. **18**, 1827 (1988).

[69] P. Giannozzi, S. Baroni, N. Bonini, M. Calandra, R. Car, C. Cavazzoni, D. Ceresoli, G. L. Chiarotti, M. Cococcioni, I. Dabo, A. D. Corso, S. de Gironcoli, S. Fabris, G. Fratesi, R. Gebauer, U. Gerstmann, C. Gougoussis, A. Kokalj, M. Lazzeri, L. Martin-Samos, N. Marzari, F. Mauri, R. Mazzarello, S. Paolini, A. Pasquarello, L. Paulatto, C. Sbraccia, S. Scandolo, G. Sclauzero, A. P. Seitsonen, A. Smogunov, P. Umari, and R. M. Wentzcovitch, J. Phys.: Condens. Matter **21**, 395502 (2009).

[70] P. Giannozzi, O. Andreussi, T. Brumme, O. Bunau, M. B. Nardelli, M. Calandra, R. Car, C. Cavazzoni, D. Ceresoli, M. Cococcioni, N. Colonna, I. Carnimeo, A. D. Corso, S. de Gironcoli, P. Delugas, R. A. DiStasio, Jr., A. Ferretti, A. Floris, G. Fratesi, G. Fugallo, R. Gebauer, U. Gerstmann, F. Giustino, T. Gorni, J. Jia, M. Kawamura, H.-Y. Ko, A. Kokalj, E. Kkbenli, M. Lazzeri, M. Marsili, N. Marzari, F. Mauri, N. L. Nguyen, H.-V. Nguyen, A. O. de-la Roza, L. Paulatto, S. Ponc, D. Rocca, R. Sabatini, B. Santra, M. Schlipf, A. P. Seitsonen, A. Smogunov, I. Timrov, T. Thonhauser, P. Umari, N. Vast, X. Wu, and S. Baroni, J. Phys.: Condens. Matter **29**, 465901 (2017).

[71] A. D. Corso and A. M. Conte, Phys. Rev. B **71**, 115106 (2005).

[72] A. D. Corso, Comput. Mater. Sci. **95**, 337 (2014).

[73] J. P. Perdew, K. Burke, and M. Ernzerhof, Phys. Rev. Lett. **77**, 3865 (1996).

[74] N. Marzari and D. Vanderbilt, Phys. Rev. B **56**, 12847 (1997).

[75] I. Souza, N. Marzari, and D. Vanderbilt, Phys. Rev. B **65**, 035109 (2001).

[76] A. A. Mostofi, J. R. Yates, Y.-S. Lee, I. Souza, D. Vanderbilt, and N. Marzari, Comput. Phys. Commun. **178**, 685 (2008).

[77] A. A. Mostofi, J. R. Yates, G. Pizzi, Y.-S. Lee, I. Souza, D. Vanderbilt, and N. Marzari, Comput. Phys. Commun. **185**, 2309 (2014).

[78] G. Pizzi, V. Vitale, R. Arita, S. Blügel, F. Freimuth, G. Gŕanton, M. Gibertini, D. Gresch, C. Johnson, T. Koretsune, J. Ibañez- Azpiroz, H. Lee, J.-M. Lihm, D. Marchand, A. Marrazzo, Y. Mokrousov, J. I. Mustafa, Y. Nohara, Y. Nomura, L. Paulatto, S. Poncé, T. Ponweiser, J. Qiao, F. Thle, S. S. Tsirkin, M. Wierzbowska, N. Marzari, D. Vanderbilt, I. Souza, A. A. Mostofi, and J. R. Yates, J. Phys.: Condens. Matter **32**, 165902 (2020).

[79] H. Ebert, D. Ködderitzsch, and J. Minár, Rep. Prog. Phys. **74**, 096501 (2011).

[80] H. Ebert et al., The Munich spin-polarized relativistic Korringa-Kohn-Rostoker (SPR-KKR) package, version. 8.5.0 (2020).

[81] S. H. Vosko, L. Wilk, and M. Nusair, Can. J. Phys. **58**, 1200 (1980).

[82] K. Hirai, J. Phys. Soc. Jpn. **67**, 1776 (1998).

[83] A. Sakuma, J. Phys. Soc. Jpn. **67**, 2815 (1998).

[84] R. M. Bozorth, Ferromagnetism (Van Nostrand, New York, 1951).

[85] P. H. Dederichs, R. Zeller, H. Akai, and H. Ebert, J. Magn. Magn. Mater. **100**, 241 (1991).

[86] A. Zunger, S.-H. Wei, L. G. Ferreira, and J. E. Bernard, Phys. Rev. Lett. **65**, 353 (1990).

[87] Y. Ishikawa, R. Tournier, and J. Filippi, J. Phys. Chem. Solids **26**, 1727 (1965).

[88] J. O. Strom-Olsen, D. F. Wilford, S. K. Burke, and B. D. Rainford, J. Phys. F **9**, L95 (1979).

[89] B. Babic, F. Kajzar, and G. Parette, J. Phys. Chem. Solids **41**, 1303 (1980).

[90] S. K. Burke and B. D. Rainford, J. Phys. F **13**, 441 (1983).

[91] S. K. Burke, R. Cywinski, J. R. Davis, and B. D. Rainford, J. Phys. F **13**, 451 (1983).

[92] S. K. Burke and B. D. Rainford, J. Phys. F **13**, 471 (1983).

Acknowledgements

This thesis conclude two and a half years of my Ph.D. research in Prof. Koretsune's group, Graduate School of Science, Tohoku University, Japan, and half a year of my overseas training in Prof. Ebert's group, Lüdwig-Maximilian-Universitäte, München, Germany. We started the research on the development of the calculation method of alloy systems with Prof. Kentaro Nomura, Institute for Material Research, Tohoku University since I was an undergraduate student. Concerning the calculation of alloy systems, we learned the supercell calculation using the open-core method from Prof. Hiroki Tsuchiura, Graduate School of Engineering, Tohoku University and the CPA calculations from Prof. Hisazumi Akai, Institute for Solid State Physics, the University of Tokyo. Needless to say, these experiences have led me to this doctoral research. I would like to express my gratitude to all the people I met through my research.

I would like to express my gratitude to Prof. Takashi Koretsune for giving me the opportunity of working in his group. As a supervisor of my doctoral research, his help on my research was immeasurable. He also accepted me to study in Germany for half a year. Through my doctoral research, we are now in the starting point for the application of the Wannier-CPA method to material research of alloy systems. I am glad if I can contribute to a part of the research.

I especially indebted to Prof. Dr. Hubert Ebert. He gave me an invaluable experience on studying the KKR Green's function method. He taught me the methods attentively to the details of the methodology and computation ways. The calculation method of the CPA on the basis of the Wannier representation seems to be a little different from the KKR-CPA calculations. However, the computational method of the KKR-CPA calculations is quite similar to that of the Wannier-CPA method and we adapted many of the techniques used by the KKR methods in this study. There is no

doubt that this experience was of the most importance in carrying out this research. It was a tough time because of Corona when I stayed in Germany. Prof. Ebert and his wife Frau Ursula Ebert gave me a lot of support even for my private life. Although it was a difficult time, I was able to stay safe and healthy and even have a good memory thanks to them. The space of this acknowledgements is too small to mention all of the things they gave me during my stay in Germany. I will never forgot the four and a half months I spent with Familie Ebert. Prof. Ebert gave me a lot of discussion even after my return to Japan and helped me writing a paper.

I would like to express my thanks Dr. Sergiy Mankovsky, Lüdwig-Maximilian-Universitäte, München. He came to the university and taught me the code usage of the SPR-KKR package despite the situation of Corona. He and his wife Ms. Svitlana Polesya also supported my stay in Germany. They kindly took me to the München airport so that I could safely return to Japan on the last flight. I was very glad that they baked me a cake and celebrated my birthday.

I would like to extend my gratitude to Prof. Kentaro Nomura for the support of my doctoral studies. He is my undergraduate supervisor and gave me the first theme that led to this research. Unfortunately, I had to leave his group because of the retirement of Prof. Bauer, but he generously cooperated with the research even after I moved from his group. He gave me a lot of advice in carrying out my research.

I would like to thank Prof. Koji Kobayashi, Institute for Material Research, Tohoku University. He supported me coding calculation programs from my undergraduate days. I learned the basics of coding from him. Concerning this research, he gave me a lot of discussion of how to code the CPA calculation in the Wannier representation and its effective algorithm.

I would like to express my thanks to Prof. Ryotaro Arita, RIKEN Center for Emergent Matter Science for accepting me to work in his group in RIKEN as a trainee. I was able to carry out a fulfilling research. I would also like to thank Prof. Takuya Nomoto, RIKEN Center for Emergent Matter Science. He gave me the first step on the Wannier-CPA calculations.

I would like to thank students and staffs who worked together as members of Koretsune group: Mr. Kenta Nakanishi, Mr. Kensuke Kurita, Mr. Daiki Sato, Mr. Alwan Abdillah Darussalam, Mr. Tatsuki Oikawa, Mr. Katsuhiro Arimoto, Mr. Syota

Namerikawa, Mr. Hiroto Saitoh, Ms. Naomi Yamamoto, and Ms. Yoko Wako. It was a nice memory to work together with them.

I would like to thank my thesis committee members: Prof. Riichiro Saito, Prof. Takafumi Sato, Prof. Kentaro Nomura, Prof. Yusuke Nambu, Prof. Takashi Koretsune, Prof. Naokazu Shibata, Prof. Joji Nasu, Prof. Masakazu Matsubara, Prof. Hisatoshi Yokoyama, and Prof. Atsushi Ono for accepting to review this thesis out of their busy schedule.

My Ph.D. work was supported by Japan Society for the Promotion of Science (JSPS) through a research fellowship for young scientists (21J10577) and Graduate Program in Spintronics (GP-Spin), Tohoku University.

I am deeply indepted to Prof. Yoshiro Hirayama and GP-Spin staff members for the financial support of my half a year overseas training in Lüdwig-Maximilian-Universitäte, München. They offered me a valuable research experience that I cannot get without belonging to the program. Because of the state of emergency over COVID-19 I had a lot of trouble such as a shutdown of the airport and not being able to use public transportation. They resolved these problems for me. I deeply appreciate their supports during my stay in Germany. Finally, I would like to thank Ms. Siobhan Nishimura. As a staff of GP-Spin, she supported me in writing English in my research.

Naohiro Ito
Sendai, Japan
December 6, 2021

List of Publication

1. N. Ito and K. Nomura, Anomalous Hall effect and spontaneous orbital magnetization in antiferromagnetic Weyl metal, J. Phys. Soc. Jpn. **86**, 063703 (2017).

2. N. Ito, T. Kikkawa, J. Barker, D. Hirobe, Y. Shiomi, and E. Saitoh, Spin Seebeck effect in the layered ferromagnetic insulators $CrSiTe_3$ and $CrGeTe_3$, Phys. Rev. B **100**, 060402(R) (2019).

3. T. Kato, K. Sugawara, N. Ito, K. Yamauchi, T. Sato, T. Oguchi, T. Takahashi, Y. Shiomi, E. Saitoh, and T. Sato, Modulation of Dirac electrons in epitaxial Bi_2Se_3 ultrathin films on van der Waals ferromagnet $Cr_2Si_2Te_6$, Phys. Rev. Materials **4**, 084202 (2020).

4. N. Ito, T. Nomoto, K. Kobayashi, S. Mankovsky, K. Nomura, R. Arita, H. Ebert, and T. Koretsune, Wannier-based implementation of the coherent potential approximation with application to Fe-based transition-metal alloys, arXiv:2111.15109 (submitted to Phys. Rev. B).